Master of Science Thesis

Microphysical models for dry and wet phyllosilicate friction

Joost Anton Roholl

August 2014
Faculty of Geosciences
Department of Earth Sciences
Utrecht University

Supervisors:
E. Bakker, Msc., Dr. J. Samuelson, Dr. S.A.M. den Hartog and Prof. Dr. C.J. Spiers

Universiteit Utrecht

Abstract

Despite extensive research and experimental studies on the frictional behaviour of phyllosilicates little is known about the physical mechanisms controlling (pure) phyllosilicate friction. The aim of this thesis is to formulate a microphysical model for the steady state frictional behaviour of phyllosilicate gouges at relatively low temperatures (room temperature to ~400 ^{0}C), where dislocation and diffusional processes are of limited importance as grain scale deformation mechanisms.

Based on a literature review it is proposed that phyllosilicate friction can potentially be controlled at one of the following scales of interaction; i) atomic scale, ii) asperity (nm) scale, iii) grain (1-10 µm) scale and iv) clast scale (10-30 µm). In order to determine the interaction scales occurring during phyllosilicates friction axial loading experiments were conducted on muscovite gouge using an applied normal load of 1.9, 2.8, 6.5 or 12.1 MPa for 24 hours. In addition, shear experiments at 6.5 MPa normal stress, strain rate velocities of 1-2 mm/s and reaching shear strains between 10-50 were performed. The deformed samples were impregnated with epoxy resin while still under load in order to eliminate unloading artefacts and preserve the actual deformed microstructure under load, thus providing the microstructural record of the active deformation mechanisms. Backscattered Scanning Electron Microscope micrographs show that this approach was indeed successful in eliminating unloading artefacts. From SEM-micrographs it is observed that during frictional sliding grains interact on level of the grain scale, i.e. the edges of interacting grains are in contact and fail by both ductile and brittle deformation during sliding.

Microphysical models were subsequently derived for friction controlled by atomic and grain scale interactions for both wet and dry phyllosilicate friction, incorporating characteristics of the microstructures observed in the literature and experiments. No models were derived for asperity controlled friction, since previous authors have already studied this process extensively Thermodynamic considerations concerning the frictional processes were employed to predict the corresponding frictional parameters, such as the coefficient of friction and its dependence on velocity.

By correlating the predicted frictional parameters with observations on phyllosilicate friction in the literature it is concluded that i) dry and wet phyllosilicate friction is not controlled by atomic scale interactions, ii) the leading hypothesis regarding wet phyllosilicate friction by Moore and Lockner (2004), namely viscous slip on an thin adsorbed film, is not in agreement with the observations on wet phyllosilicate friction and iii) based on the derived grain scale controlled microphysical models cleavage failure of edge-contacts do occur during frictional sliding, but do not control friction.

Table of Contents

1 Introduction

1.1 General context of this study

Interplate earthquakes are amongst the most devastating natural phenomena faced by humanity. The most destructive earthquakes generally originate at subduction zone megathrusts, as demonstrated most recently by the magnitude 9.0 Tohoku-Oki earthquake and related tsunami that struck the coast of Japan (Simons et al., 2011). The economic and human losses following such events emphasize the need to understand the mechanics of earthquakes. Despite this need, the exact mechanisms of earthquake nucleation are still poorly understood.

The current understanding is that earthquakes are the result of a frictional stick-slip instability (Scholz, 1998, 2002; Paterson and Wong, 2005). In this view, no motion occurs along a fault in the aseismic period in between earthquakes, building up (elastic) stresses as a result of continued tectonic loading. Once these stresses overcome the frictional resistance on the fault, sudden movement or slip on the fault will result in an earthquake. A prerequisite for frictional stick-slip behaviour is so-called velocity weakening frictional behaviour, whereby the frictional resistance to slip reduces with increasing slip velocity, leading to unstable slip (Scholz, 1998, 2002; Paterson and Wong, 2005). This is in contrast to velocity strengthening behaviour, which is characterized by an increase in the frictional resistance to slip with increasing slip velocity, meaning that this form of frictional behaviour is inherently stable and incapable of producing seismic events (Scholz, 1998, 2002; Paterson and Wong, 2005).

Unstable slip, and hence earthquake nucleation, only occurs in a region known as the seismogenic zone, which is bound by aseismic regions. Focal depth data shows that the seismogenic zone of subduction zone megathrusts is located between 5-15 km depth and ~40 km depth (Fig. 1.1; Hyndman, 1997). The general consensus is that both the up-dip and down-dip boundaries are related to temperature controlled processes, with the up-dip boundary situated at 100-150 ^{0}C and the down-dip boundary placed at ~ 400 ^{0}C (Hyndman, 1997).

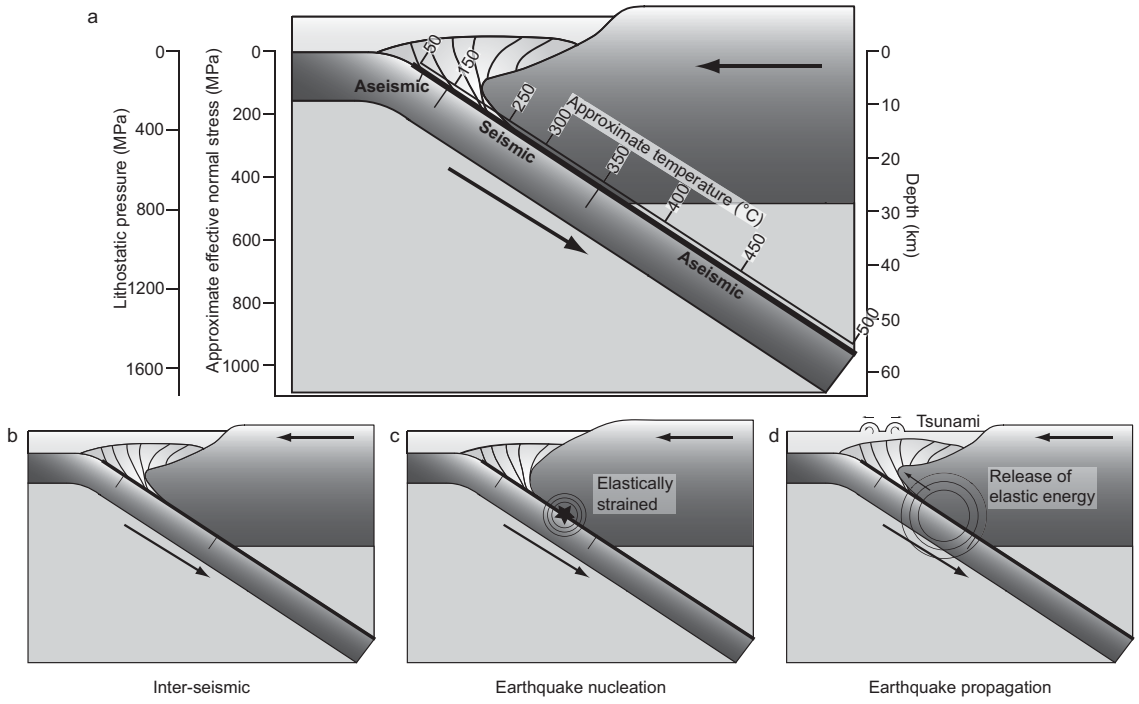

Figure 1.1 Schematic representation showing a) a cross section of a subduction zone with the seismic and aseismic zone(s) depicted. (b-d) Schematic representation characterizing the seismic cycle, with (b-c) the building up of elastic stress and no motion, leading to (d) the nucleation of an earthquake when the frictional resistance is overcome and subsequent propagation of the earthquake. After den Hartog et al. (2013)

The down-dip seismogenic limit on subduction megathrusts is usually explained by the change from brittle to ductile deformation with increasing temperature (e.g Hyndman et al., 1997; Scholz, 1998, 2002;) or by the intersection of the thrust fault with the fore-arc Moho (e.g. Hyndman, 1997; Peacock and Hyndman, 1999). In contrast, no such consensus exists regarding the up-dip limit of the seismic zone. It has been suggested that the transition of the frictionally weak, hydrous phyllosilicate mineral smectite to the stronger non-hydrous mineral illite causes the onset of seismic behaviour, based on the coincidence of the temperature of the smectite to illite transition with the temperature of the up-dip seismogenic limit (Vrolijk, 1990). This smectite-to-illite hypothesis for the up-dip seismogenic limit along subduction megathrusts, however, implicitly assumes velocity weakening properties of illite, as opposed to velocity strengthening of smectite. Alternative hypotheses for the up-dip limit exist, for example a change in the degree of lithification of fault gouge (Marone and Scholz, 1988). This hypothesis is based on the observation that deformation in unconsolidated gouge material is not localized and in experimental studies produces stable sliding (Beeler et al., 1996). Progressive consolidation of fault gouge with depth, yielding localized deformation and potential for unstable behaviour, may then explain the onset of seismogenesis**.**

Clearly, to better understand earthquake nucleation along plate boundary faults, notably subduction megathrusts, the mechanisms underlying velocity strengthening versus velocity weakening behaviour need to be identified.

1.2 Rate and state friction

The velocity dependence of friction is in general described and interpreted using an empirically based model called the rate and state friction model (RSF) originally proposed by Dieterich (1979) and Ruina (1983). There are various variations of the RSF-equation, but the one currently best fitted to experimental observations is the 'slowness' or Dieterich-Ruina equation. In this equation the friction coefficient is dependent on the instantaneous sliding velocity and a time-dependent state variable:

$$\mu = \mu_0 + a\ln\left(\frac{V}{V_o}\right) + b\ln\left(\frac{V_o\theta}{D_c}\right) \qquad (1.1)$$

where μ is the coefficient of friction, which is the ratio of the shear stress τ to the (effective) normal stress σ, μ_0 is the coefficient of friction at reference slip velocity V_0, V is the slip velocity and a and b are material properties called the direct and evolution effect, respectively, as explained below. Furthermore D_c is the so-called critical slip distance and θ is state variable that evolves according to:

$$\dot{\theta} = 1 - \left(\frac{V\theta}{D_c}\right) \qquad (1.2)$$

The significance of the different terms is illustrated in Figure 1.2, which shows schematically the possible frictional responses to an increase in sliding velocity as represented in the RSF framework.
For an e-fold increase in sliding velocity, an immediate increase in friction is observed with a magnitude a, which is therefore aptly named the 'direct velocity effect'. The frictional coefficient then decreases over time to form a new steady state value over a characteristic slip distance D_c. The difference between the peak friction value caused by the velocity increase and the new steady state value is defined by b.

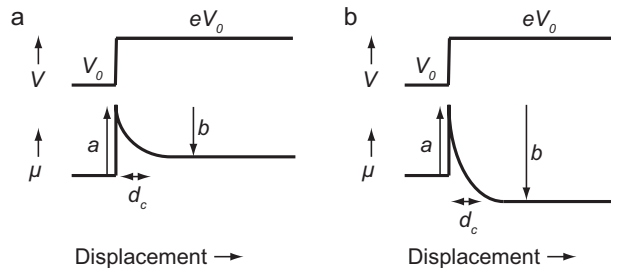

Figure 1.2 The schematic response of friction to a velocity increase of magnitude e for a) a velocity strengthening material and b) a velocity weakening material. After den Hartog et al. (2013)

From Figure 1.2 it is clear that, together, the parameters a and b define the velocity effect of friction. The change in steady state friction due to velocity (e.g. Scholz, 1998 and Paterson and Wang, 2005) is described by:

$$\frac{d\mu_{ss}}{d\ln(V)} = (a-b) \tag{1.3}$$

The parameters a and b are generally positive and have a magnitude in the order of 10^{-2} (Scholz, 2002). As is clear from Figure 1.2 and formula 1.3 a positive value of $(a-b)$ corresponds to an increase in friction coefficient with increasing sliding velocity, thus velocity strengthening behaviour, whereas negative $(a-b)$ values result in velocity weakening.

1.3 Previous microphysical modelling efforts

Considerable research effort has focused on determining experimentally the frictional strength and the velocity dependence of friction for a wide variety of rock forming materials. Interpretation of the obtained frictional properties has mainly been done in the framework of the RSF theory. The RSF model is empirically based and lacks a proper physical basis, although some attempts have been made to obtain a physical basis for the RSF parameters (e.g. Baumberger, 1999; Rice et al., 2001). The essential notion involves the competition between growth and destruction of asperity contact areas. However, is has never been convincingly verified that asperity contacts control friction in rock materials and furthermore this hypothesis does not fit well with observed gouge microstructures of friction experiments (e.g. Niemeijer and Spiers, 2005; den Hartog, 2013). In order to extrapolate lab data to natural fault conditions and to be able to develop accurate earthquake models, a better understanding of the actual physical mechanisms by which frictional sliding is accommodated in fault zones is essential, notably in gouge filled faults.

Recognizing this importance of a (micro)physical based approach, Bos and Spiers, (2000, 2002) and later Niemeijer and Spiers, (2005, 2007) developed microphysical models in which frictional behaviour of fault rocks was not explained in terms of the RSF parameters, but as a function of actual physical mechanisms. These models were based on experiments done on phyllosilicate + halite mixtures, acting as a fault gouge analogue. The basic premise of the model involves a competition between the compaction caused by the deformation by pressure solution of halite clasts and intergranalur dilatation and shows favourable agreement with the experiments. Some of the assumptions in this model, however, are not realistic for natural fault conditions. Accordingly, den Hartog and Spiers (2014) improved and extended the models by Bos, Niemeijer and Spiers and formulated a microphysical model for the frictional behaviour of quartz-illite mixture, deformed at (P,T) conditions equivalent to natural subduction zones. In the model of den Hartog and Spiers (2014), a matrix-supported microstructure is adopted, in which friction is assumed to occur by rate-independent slip on aligned phyllosilicates and thermally activated deformation of the intervening quartz clasts. This model was found to predict many of the trends observed in the friction experiments on quartz-illite mixtures conducted by den Hartog and Spiers (2013).

Despite the overall good agreement between model predictions and experimental results found by den Hartog and Spiers (2014), some disagreement existed, which was explained by the oversimplification of pure phyllosilicate friction in the model. Den Hartog and Spiers (2014) incorporated phyllosilicate friction as a rate-independent process, while phyllosilicates are widely observed to be velocity strengthening (e.g. Faulkner et al., 2007; Ikari et al., 2011a). This shortcoming highlights the need for a microphysical model for the frictional behaviour of pure phyllosilicates. Formulation of a microphysical model for phyllosilicate friction and subsequent incorporation into the original model for phylloslicate-quartz friction by den Hartog and Spiers (2014), would be of wide interest, given the widespread occurrence of phyllosilicate-rich fault zones, such as subduction zones, continental strike slip faults and low angle detachment faults (Schleicher et al., 2010; Holdsworth, 2011; Ikari and Saffer, 2011; Collettini, 2011**)**

1.4 Microphysics of phyllosilicate friction

As of yet, no microphysical model exists that can quantitatively predict the frictional behaviour of pure phyllosilicates. In fact, little is known about the microphysical processes active during phyllosilicate friction. Based on a correlation between the interlayer (001) bond strength of phyllosilicates and the frictional strength, Moore and Lockner (2004) proposed that the strength of dry phyllosilicates is controlled by breaking of the interlayer bonds. Similarly, the same authors explained the strength of wet phyllosilicates as being governed by viscous slip on thin water layers weakly bonded to the surface of phyllosilicates. Haines et al. (2013), dispute this general view and suggest that frictional weakness of phyllosilicates can be explained by strain accommodation along very narrow surfaces with only little dilation. Neither group of authors however proposes a microphysical model for phyllosilicate friction, nor a proper quantitative account of the physical mechanisms that control friction in phyllosilicates.

To formulate a quantitative model for phyllosilicate friction, the nature of the interactions between phyllosilicate grains needs to be understood, notably the scale of interaction. There are four different scales of interaction proposed that occur within a deforming aggregate of phyllosilicate grains that can control the frictional sliding and hence the macroscopic frictional behaviour:

i) Atomic scale interactions between the sliding grains
ii) Asperity scale (1-10nm) interactions between the sliding grains
iii) Grain scale interactions (0.1μm-10μm) between the sliding grains
iv) Clast scale (10μm-~40μm), interaction of the scale of the deforming aggregate

Identifying which of the above interactions dominates the frictional behaviour of phyllosilicates requires microstructural analysis of deformed phyllosilicate gouges. However, samples obtained from shear experiments are usually impregnated after unloading and sample extraction from the deformation apparatus. This is a result of the technical difficulties of impregnating samples while under load. The draw-back of impregnating after unloading is the presence of unloading features in the microstructures, such as extensional cracks or opened-up pre-existing shear (bands), which are not related to deformation processes occurring during the experiments but rather are experimental artefacts. The precise interaction between individual grains, especially in shear bands, is therefore mostly obscured. In order to obtain a better constraint of the scale of interaction between the individual phyllosilicate grains, sheared samples should thus be impregnated while still being under load.

1.5 Aims and approach

The aim of this thesis is to formulate a microphysical model for the steady state frictional behaviour of phyllosilicate gouges. The approach adopted involves a combination of reviewing literature, conducting loading and shear experiments, microstructural analysis and microphysical modelling. The focus of this study is on the steady state frictional behaviour of phyllosilicates at relatively low temperatures (room temperature to ~400^{0}C). At these temperatures, the

microstructures are less complicated to interpret than microstructures observed at higher temperatures and the frictional behaviour is better constrained and studied by previous experimental studies.

First, the existing literature on phyllosilicate frictional behaviour is reviewed, distinguishing the main trends in frictional behaviour observed. Particular attention is paid to experimental microstructures and the main microstructural characteristics as a function of temperature are identified. Next, the results of both loading and shear experiments are described. The microstructures resulting from these experiments were recovered by impregnating the deformed sample with epoxy resin while still under load, attempting to 'freeze' the microstructural record of the active deformation mechanisms. Interpretation of Scanning Electron Microscopic (SEM) images of the resulting sections and comparison thereof with literature observations was done to identify the scale of interaction that occur during the frictional behaviour (e.g. atomic, nm or 1-10 µm scale) between phyllosilicate grains during slip. This information was subsequently used as the basis to formulate a microphysical model for pure phyllosilicate friction. Thermodynamic considerations concerning the frictional processes were employed to predict the corresponding frictional parameters. Conclusions concerning which of the different microphysical models formulated is a viable hypothesis of the mechanism of pure phyllosilicate friction are then made based on the experiments and comparison with observations on phyllosilicate friction.

2 Previous studies on the frictional behaviour of phyllosilicates

In this section, a review of the available literature concerning (steady-state) phyllosilicate friction is given. Focus is on the key observations needed for the development including the effect of pore fluids on the frictional strength, the velocity and temperature dependence of the frictional strength. Furthermore the microphysical features of microstructures observed in the literature are summarized here and will be used as a basis for the development of the microphysical models described in sections 4 and 5 of this thesis.

2.1 Mechanical data

2.1.1 Effects of water, interlayer cations and temperature on friction coefficient

The friction coefficients of dry and wet phyllosilicates obtained in a range of studies at low temperatures (RT>T<~200 ^{0}C) are given in Table 2.1. The coefficients of friction reported by the different authors are not always obtained in exactly the same manner. Some authors report the friction coefficients taken at the yield point (e.g. den Hartog et al., 2013; Behnsen and Faulkner, 2013) while other authors present coefficients obtained for steady state sliding and/or much higher shear strains (e.g. Moore and Lockner, 2004; van Diggelen et al., 2010; den Hartog et al. 2013). For some minerals, the frictional strength increases with increasing strain (e.g. van Diggelen et al., 2010; den Hartog et al. 2013).

Two main observations follow from the data presented in Table 2.1. Firstly, the frictional strength of almost all dry and wet phyllosilicate minerals studied are significantly lower than the frictional strength of other rock forming minerals, which are uniformly characterized by frictional coefficients of ~0.6-0.85 (i.e. Byerlee, 1978; Ikari et al., 2011a). Secondly, frictional strength of phyllosilicate minerals under wet conditions is consistently lower than the frictional strength of the same mineral under dry conditions.

Behnsen and Faulkner (2013) conducted triaxial shear experiments on montmorillonite samples containing either Na^+, K^+, Ca^{2+}, or Mg^{2+} as interlayer cation. They found that K-montmorillonite is stronger (μ = 0.26) than Na, Ca or Mg-montmorillonite (μ = 0.15, 0.11 and 0.11, respectively). They proposes that the increased frictional strength of K-montmorillonite is related to the decrease in interlayer water content of K- montmorillonite compared to Na, Ca or Mg-montmorillonite, caused by to the presence of the K^+-cation. Ikari et al. (2007) also reported a slight increase in the friction coefficient (0.05) for Na-montmorillonite compared to Ca-montmorillonite. The exchange of interlayer cations in some of the phyllosilicates can therefore possibly influence the frictional strength of phyllosilicate minerals.

Due to experimental difficulties, few experiments have been conducted at in situ fault conditions. Therefore, data on the frictional behaviour of phyllosilicates at high temperatures is limited. In studies conducted on biotite and muscovite (e.g. van Diggelen et al., 2010; den Hartog et al., 2013), however, it is observed that the wet frictional strength increases with increasing temperatures (Fig. 2.1). Wet talc, on the other hand, shows a slight decrease of the friction coefficient with increasing temperature Moore and Lockner, 2007), indicating that the increase in frictional strength with temperature found in biotite and muscovite may not be a general property of all phyllosilicate minerals. As mentioned before, strain hardening is observed for some phyllosilicate minerals;(e.g. van Diggelen et al., 2010; den Hartog et al., 2013). The effect of increasing shear strain on the frictional strength of muscovite is also shown in Figure 2.1**.** This strain hardening effect is in all likelihood not a material property, but the result of the experimental setup (Den Hartog, pers. com.).

Mineral	μ_{dry}		μ_{wet}	
Lizardite $Ni_3(Si_2O_5)(OH)_4$	0.35 0.82	(23) (18)	0.18-0.24 0.29 0.41	(20) (23) (11)
Kaolinite $Al_2Si_2O_5(OH)_4$	0.40 0.40 0.66 0.82 0.84	(23) (16) (2) (8) (11)	0.20-0.23 0.25 0.29 0.30 0.51	(7) (16) (23) (17) (11)
Talc $Mg_3Si_4O_{10}(OH)_2$	0.22 0.24 0.35 0.36 0.36 0.37	(23) (8) (14) (1) (18) (11)	0.16 0.17 0.18 0.20 0.20 0.22	(1) (8) (23) (11) (14) (6)
Pyrophyllite $Al_2Si_4O_{10}(OH)_2$	0.33 0.38	(23) (11)	0.27 0.28	(23) (11)
Montmorillonite $(Na,Ca)_{0.33}(Al,Mg)_2(Si_4O_{10})(OH)_2 \bullet n(H_20)$	0.22 0.39 0.49-0.62 0.8	(2) (23) (12) (13)	0.06-0.12 0.08-0.32 0.09-0.48 0.10 0.12 0.12 0.15-0.32 0.17 0.27-0.34	(14) (10) (12) (15) (22) (23) (9) (5) (3)
Phlogopite $KMg_3(AlSi_3O_{10})(F,OH)_2$	0.31 0.45-0.51	(23) (11)	0.27 0.31-0.33	(23) (11)
Biotite $K(Mg,Fe)_3AlSi_3O_{10}(F,OH)_2$	0.31 0.46	(23) (11)	0.24-0.35 0.27 0.29 0.33	(6) (23) (25)* (11)
Muscovite $(KAl_2(AlSi_3O_{10})(F,OH)_2)$	0.42 0.58 0.59	(23) (11) (8)	0.29-0.46 0.35-0.38 0.38 0.38-0.43 0.42-0.46 0.47	(24)* (6) (23) (21)* (11) (8)
Illite $(K,H_3O)(Al,Mg,Fe)_2(Si,Al)_4O_{10}[(OH)_2,(H_2O)$	0.40 0.48	(23) (2)	0.27-0.32 0.30 0.38 0.42-0.61	(19) (22) (5) (10)
Chlorite $(Mg,Fe)_3(Si,Al)_4O_{10}(OH)_2 \cdot (Mg,Fe)_3(OH)_6$	0.42 0.44 0.68 0.68	(2) (23) (11) (8)	0.27-0.32 0.32 0.38 0.41	(19) (23) (11) (8)

Table 2.1 All values for the frictional strength are taken at room temperature except when indicated with * in which case the values were obtained at 200 ^{0}C

1) Horn and Deere (1962) 2) Shimamoto and Logan (1962) 3) Bird (1984) 4) Logan and Rauenzahn 5) Morrow et al. (1992) 6) Scruggs and Tullis (1998) 7) Bos et al (2000) 8) Morrow et al. 2000 9) Saffer et al (2001) 10) Saffer and Marone (2003) 11) Moore and Lockner (2004) 12) Ikari et al (2007) 13) Moore and Lockner (2007) 14) Moore and Rymer (2007) 15) Takahasi et al. (2007) 16) Crawford et al (2008) 17) Brantut et al (2008) 18) Moore and Lockner (2008) 19) Ikari et al. (2009) 20) Carpenter et al (2009) 21) Van Diggelen et al. (2010) 22) Tembe et al. (2010) 23) Behnsen and Faulkner (2013) 24) Den Hartog et al. (2013) 25) Lu and He (2014)

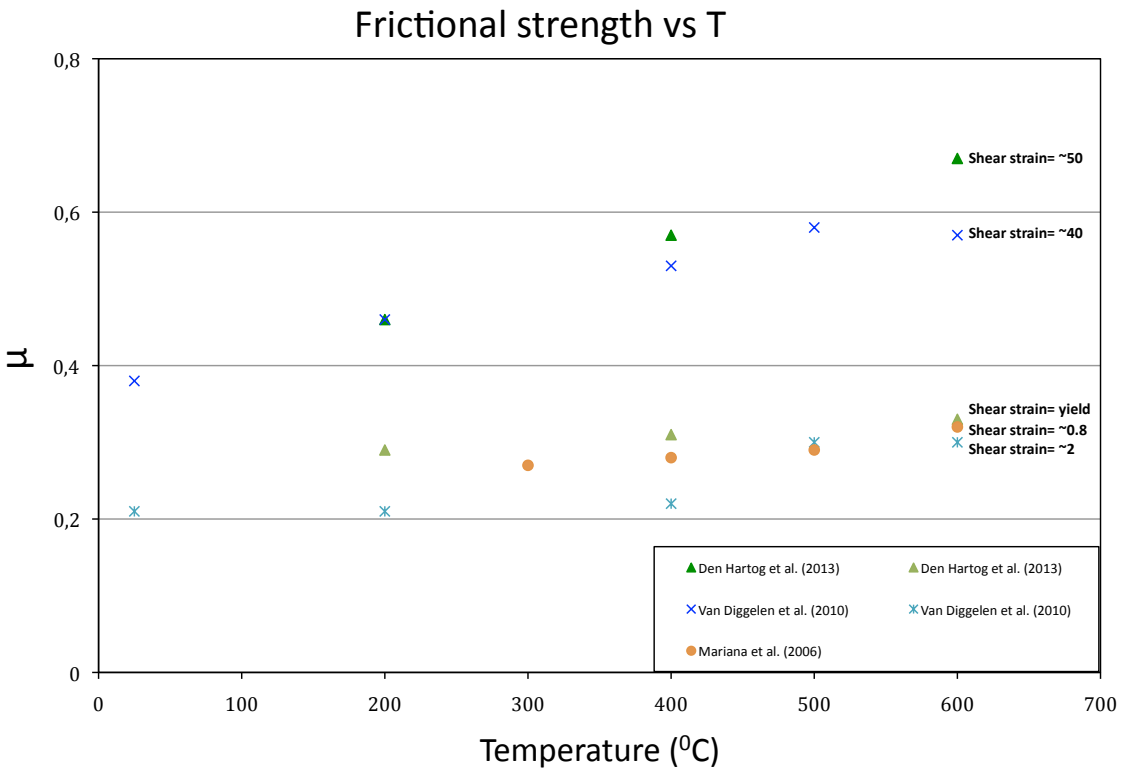

Figure 2.1 Frictional strength of wet muscovite from various authors at different amounts of shear strain versus temperature.

2.1.2 Effect of σ_n and 001 interlayer bond strength on friction coefficient

Behnsen and Faulkner (2012) investigated the effect of increasing normal stress on the frictional strength of phyllosilicates at room temperature. These authors concluded that there is negligible effect of the normal stress on the frictional strength of dry phyllosilicates, and very small effect on the frictional strength of wet phyllosilicates.

The correlation between interlayer bond strength (IBS), measured as the electrostatic separation energy, and the data on the frictional strength of dry phyllosilicate powders reported by Moore and Lockner (2004) and Behnsen and Faulkner (2012) are shown in Figure 2.2. The data of Behnsen and Faulkner (2012) are not in complete accordance with the findings of Moore and Lockner (2004). As is seen in Figure 2.2 no clear relation exists between IBS and the frictional strength reported by Behnsen and Faulkner (2012), while the strength data of Moore and Lockner show a clear linear relation with the IBS. Behnsen and Faulkner (2012) proposed that this discrepancy could be caused by varying amounts of strain hardening in the data of Moore and Lockner (2004).

No relation is found between the IBS and frictional strength of wet phyllosilicates (Moore and Lockner, 2004; Behnsen and Faulkner, 2012), but a qualitative relation on the 001 plate surface energies is found. Both authors reported that the frictional strength of water saturated phyllosilicate minerals with hydrophobic plate surfaces is found to be less weakened by the presence of water than the phyllosilicate minerals with hydrophilic surfaces (e.g Morrow et al, 2000; Moore and Lockner, 2004; Behnsen and Faulkner, 2012).

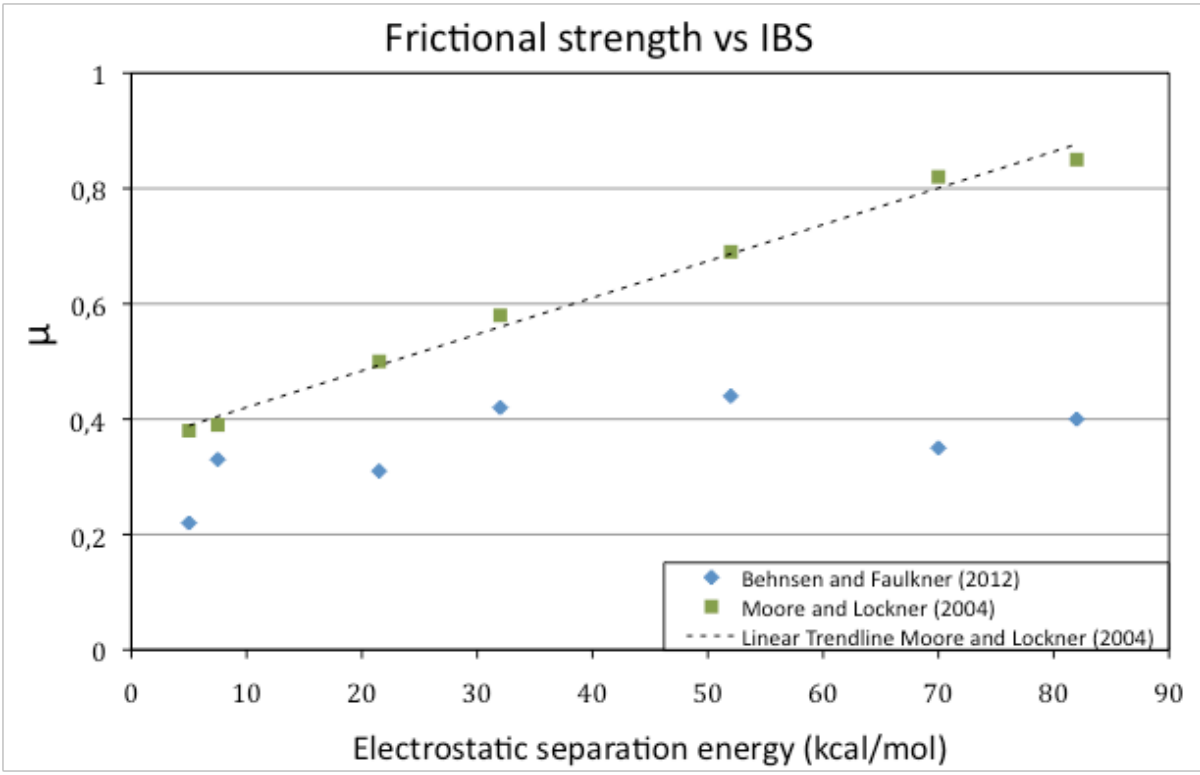

Figure 2.2 Frictional strength of dry phyllosilicate minerals from studies of Moore and Lockner (2004) and Behnsen and Faulkner (2012) versus the electrostatic separation energy of the 001 plane (taken from Giese (1978, 1980 and Bish (1981)). The dashed line represents the linear relation between μ and electrostatic separation energy reported by Moore and Lockner (2004). This figure is modified from Behnsen and Faulkner (2012)

2.1.3 Velocity dependence of friction coefficient

It is well established that phyllosilicates show velocity-strengthening behaviour at room temperatures. Reported values of $(a-b)$ are almost always positive and typically in the range of 0.005- 0.02 (e.g. Ikari et al, 2010; van Diggelen et al., 2010; den Hartog et al., 2013).

Data on the velocity dependence of pure phyllosilicate friction at higher temperatures is scarce. Studies on the velocity dependence of pure muscovite friction at high temperatures were conducted by Mariana et al. (2006), van Diggelen et al. (2010) and den Hartog et al (2013). Recently, the velocity dependence of biotite friction was studied by Lu and He (2014). The $(a-b)$ values obtained from experiments on muscovite by den Hartog et al. (2013) and on biotite by Lu and He (2014) for temperatures ranging from room temperature to ~ 700 ^{0}C are shown in Figure 2.3. For both biotite and muscovite the $(a-b)$ values decrease from positive (velocity-strengthening) to near zero (velocity-neutral) or even slightly negative (velocity-weakening) with increasing temperature up to ~ 400 ^{0}C. At higher temperatures, the data of den Hartog et al (2013) show an increase in $(a-b)$ values, whereas the data on biotite from Lu and He (2014) remain constant and slightly negative.

In most studies, stable sliding was observed, but at high temperatures (500^{0}C -700^{0}C), Mariana et al. (2006), van Diggelen et al. (2010) and den Hartog et al (2013) occasionally observed stick-slip behaviour of muscovite, indicative unstable behaviour. In comparison, Lu and He (2014) observed stick-slip behaviour of biotite at temperatures above 400 ^{0}C.

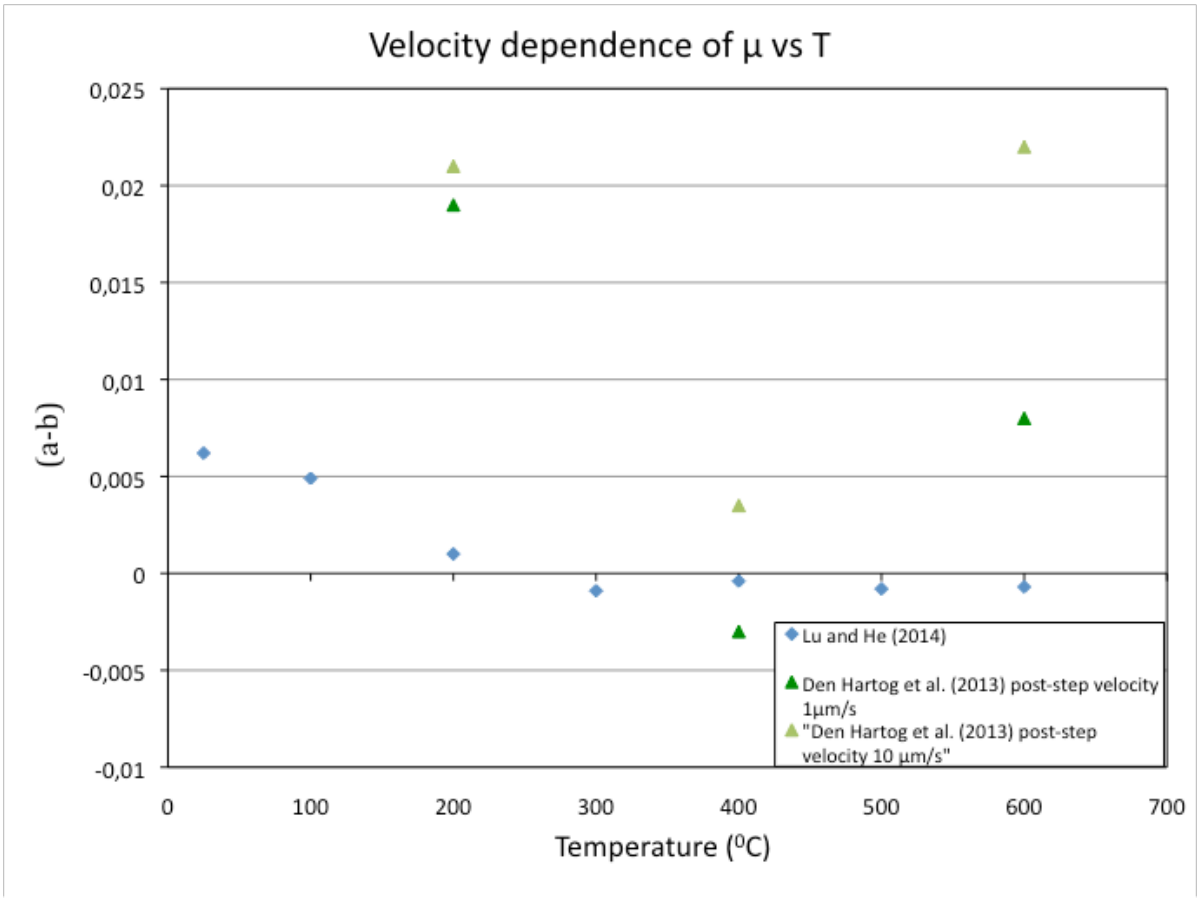

Figure 2.3 $(a-b)$ versus temperature. Data from Lu and He (2014) for biotite and Den Hartog et al. (2013) for muscovite

2.2 Microstructural observations

2.2.1 Compaction microstructures before shearing

Microstructures of phyllosilicate samples that have only been compacted show several common features (Figure 2.4; Misra and Burg, 2012; Lu and He, 2014). i) The phyllosilicate grains remain typically plate like**,** aligning their basal plan (sub)-perpendicular to the applied loading direction ii) the phyllosilicates define a wavy foliation, iii) the phyllosilicate grains are aligned with their basal plane (sub)-perpendicular to the applied load and iv) Grains bend at their edges in pore spaces to come into contact with neighbouring grains (Misra and Burg, 2012).

Figure 2.4a) Microstructure of compacted biotite. σ_n is ~50 MPa at room temperature (Lu and He, 2014)

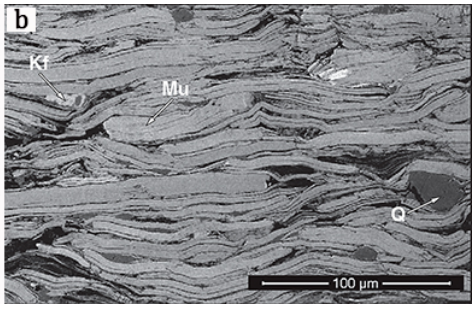

Figure 2.4b) Microstructure of compacted muscovite. σ_n is 170 MPa, loaded for 30 hours at 590 °C (Misra and Burg, 2012)

2.2.2 Microstructures of phyllosilicates sheared at low T (RT<T< ~200^{0}C)

The microstructures of phyllosilicates sheared at low temperatures share abundant common features (Moore and Lockner, 2004; van Diggelen et al., 2013; Behnsen and Faulkner, 2013; den Hartog et al., 2013; Haines et al., 2013; Lu and He, 2014). SEM-micrographs of typical sheared phyllosilicate samples are shown in Figure 2.5. There is no noticeable difference in the microstructure between wet and dry phyllosilicates (Moore and Lockner, 2004). The main microstructural features of phyllosilicate gouges sheared at temperatures up to 200^{0}C are as follows:

i) All microstructures show a wavy, anastomosing foliation, composed of intersecting P-, R1-, Y- and boundary shears (Fig. 2.5a,c,d; terminology after Logan, 1992).

ii) In these shear bands, the phyllosilicate grains have a fine grain size and are orientated with their basal plane parallel to the shear direction (Fig, 2.5 a-d). The grains commonly appear parallel to each other. Often, the grains show evidence of brittle deformation, including fracturing and cleavage of grains (Fig. 2.5b). Evidence for kinking is also commonly observed (Fig. 2.5b).

iii) Lenses with a roughly sigmoidal shape containing coarser grains are situated between the shear bands (Fig. 2.5a,c,d). The grains in these bands commonly do not have the same orientation as the shear bands and are (much) less deformed than the grains in the shear bands. Evidence for kinking is commonly seen in the lenses (Fig. 2.5b).

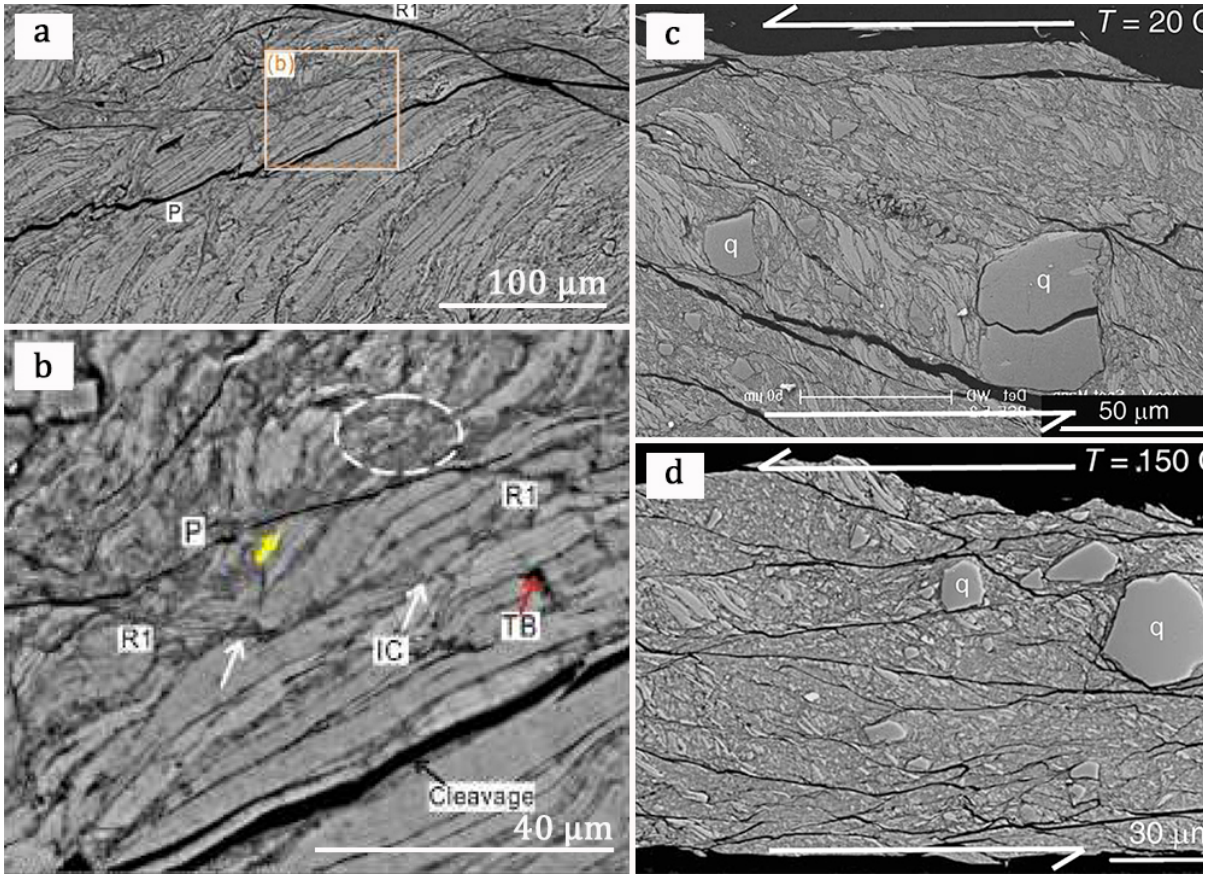

Figure 2.5 a) Microstructure of sheared biotite at 100 ^{0}C with σ_n of 200 MPa (Lu and He (2014). P and R1 denote P- and Riedel-shears respectively. b) Detail of a). c ,d) Microstructures of muscovite sheared at 20 and 150 ^{0}C (van Diggelen et al., 2010)

2.2.3 Microstructures of phyllosilicates sheared at intermediate T(~200^{0}C <T<~400^{0}C)

The main features of microstructures of muscovite (van Diggelen et al., 2010 and den Hartog et al., 2013) and biotite (Lu and He, 2014) observed at intermediate temperatures, i.e. between ~200 and ~400^{0}C do not differ greatly from the observed features at low temperatures *T* (RT<T< ~200^{0}C). The microstructures are still characterized by a wavy, anastomosing foliation of intersecting P-, R1-,

Y- and boundary shears with sigmoidal shaped lenses containing coarser grains. At these temperatures, ductile deformation features become more pronounced, for example kinking and multiple types of folding. Van Diggelen (2010) also observed that the shear bands decreased in width with an increase in the temperature, accompanied by a more widespread occurrence of the lenses.

2.2.4 Microstructures of phyllosilicates sheared at high T (~400^{0}C <T<~700^{0}C)

At high temperatures (~500-700 ^{0}C), the microstructural observations of van Diggelen et al. (2010), den Hartog et al. (2013) and Lu and He (2014) become more divergent. In Figure 2.6 the microstructures observed by these authors are shown. Den Hartog et al (2013) observed no significant difference between the microstructures of samples sheared at high temperatures (600^0 C) with respect to low temperature (200^0 C). Lu and He (2014), on the other hand, observed intensively deformed and less deformed domains in their sheared biotite samples (T=500-700^0 C). In the intensively deformed domains, evidence for both brittle and ductile deformation was found, resulting in a very chaotic structure. The less deformed regions showed mostly evidence for ductile deformation, including kinking and folding, similar to their samples sheared at intermediate temperatures (Lu and He, 2014). In the samples of van Diggelen et al (2010) the elongated lenses become more pronounced with increasing temperatures and by definition the shear bands become smaller. In the microstructures observed at 600^0 C, no shear bands are visible and the structure is characterized by an oblique foliation with grains orientated at an angle of ~ 20^0 to the shear direction. Mariana et al., 2006 deformed muscovite gouges at temperatures of 400-600^{0}C, at very low strain rates for very low strains. These authors observed the following features: i) a main foliation sub-parallel to the shear direction, ii) some R1 shears, iii) heterogeneous deformation with areas of intensive kinking and iv) evidence for fracturing of individual mica grains. From the above studies, it follows that the common microstructural features of phyllosilicates sheared at temperatures above 600^{0}C are: i) a decrease or even absence of localized deformation (in shear bands) and ii) an increase in ductile deformation processes.

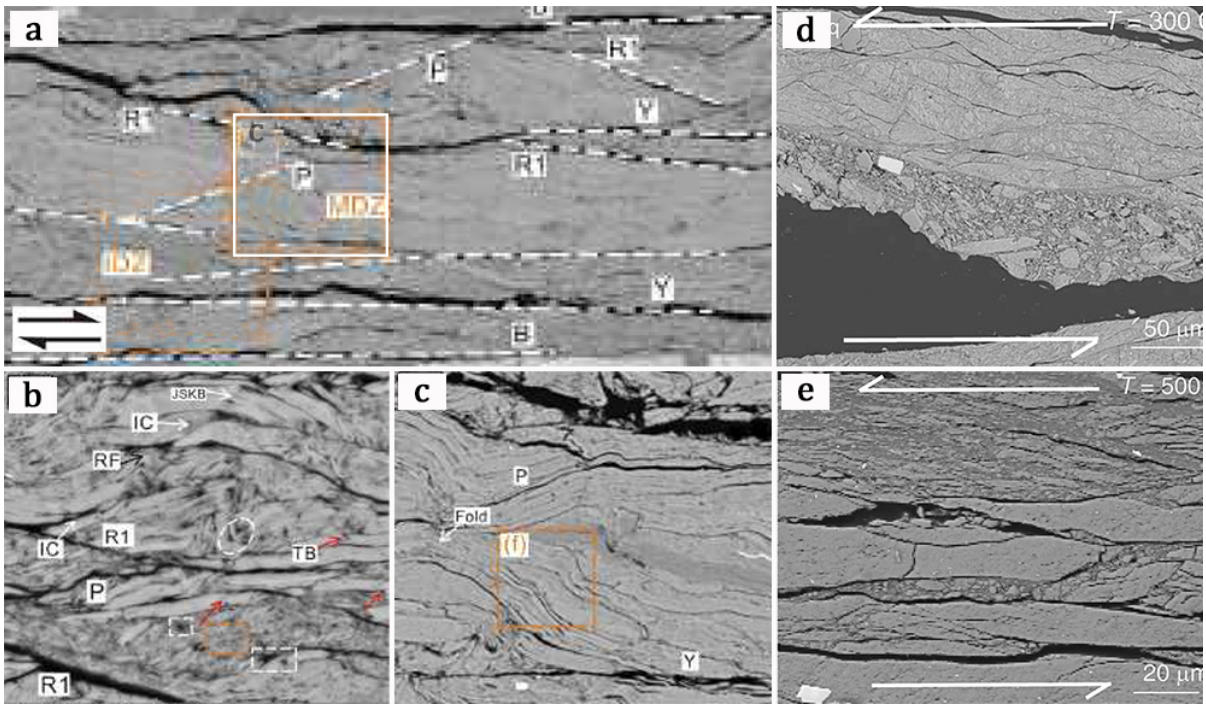

Figure 2.6 a) Overview microstructure of sheared biotite at 500 ^{0}C. b) and c), details of a). d) Microstructure of sheared muscovite at 300 ^{0}C (van Diggelen et al., 2010). Microstructure of sheared muscovite at 500 ^{0}C (van Diggelen et al., 2010).

3 Experiments

Two types of experiments were conducted in this study: loading experiments and shear experiments. The aim of both types of experiments was to obtain the microstructures of both compacted and sheared phyllosilicates gouges while still under load for different applied normal stresses.

3.1 Methods

3.1.1 Sample material

Commercially obtained muscovite powder, with a grain size of less than 44 µm was used in both types of experiments. X-Ray Diffraction (XRD) analysis showed the powder to be 97.3% pure with a quartz contamination of 2.7%. This powder was mixed with and equal weight of demineralised water to form a paste that was used as sample material.

Figure 3.1 An overview of the experimental setup. 1) Weights used to apply the different loads. 2) Delrin POM piston. 3) Delrin POM container in which the sample is placed and loaded 4) Plastic tube connecting Delrin POM piston to either a vacuum pump or a syringe as shown here. 5) Handles used to turn upper piston in shear experiments

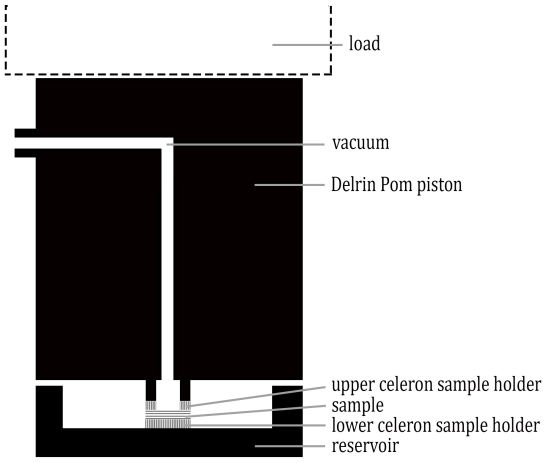

Figure 3.2 Schematic profile of experimental setup

3.1.2 Experimental setup and procedure: loading experiments

All loading experiments were conducted in the 'dead-weight' set-up shown in Figure 3.1. A schematic profile is presented in Figure 3.2. In this setup, the sample material is located between two 1 mm Celeron (a reinforced laminated plastic) sample holders and is placed in a disk-shaped container (Fig. 3.3). The container was used to act as a reservoir for the epoxy resin and made of an acetal homopolymer (Delrin POM), a plastic to which epoxy resin does not adhere, hence facilitating easy sample removal. The load on the sample is applied by weights, which can be varied in mass and number. The load is transferred to the sample via a Delrin POM piston with a central hole (Fig. 3.2), allowing for the application of a vacuum and hence flow of the epoxy resin.

A ~1 mm thick layer of muscovite–water paste was distributed between the Celeron sample holders and placed in the Delrin POM container. The sample was subsequently loaded for 24 hours at an applied normal stress of 1.9, 2.8, 6.5 or 12.1 MPa. While still under load, pre-heated Araldite 2020 epoxy resin (15 minutes at 50 ^{0}C) was introduced into the reservoir using a syringe. The sample material was then impregnated by applying a vacuum at the top of the Delrin POM piston, yielding

upward flow of the epoxy resin, into the sample. The vacuum was maintained for 5-30 minutes until the epoxy resin was observed in the plastic tube connecting the vacuum pomp with the Delrin POM piston, presumably having impregnated the sample. The epoxy resin was then cured for approximately 30 hours, while remaining the load constant. Finally, the assembly of sample and sample holders was carefully removed from the reservoir.

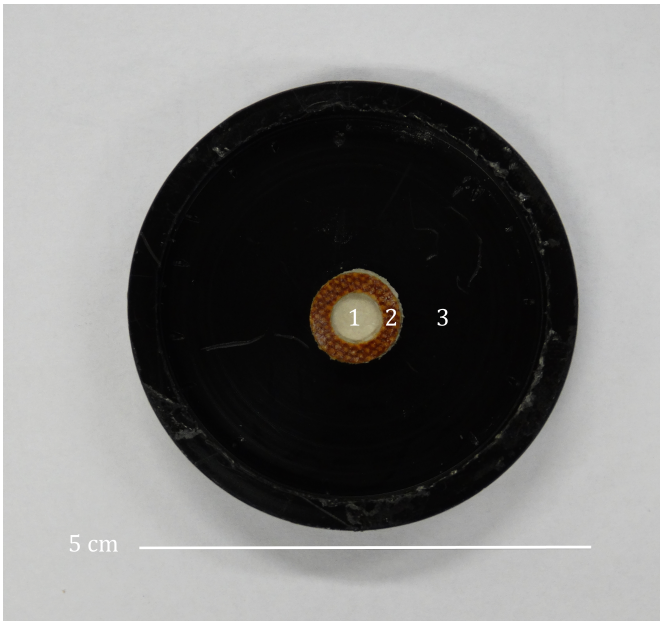

Figure 3.3 Detail of the sample setup with 1) the muscovite water paste, 2) the upper Celeron sample holder and 3) the Delrin POM reservoir disk

3.1.3 Experimental setup and procedure: shear experiments

The shear experiments were conducted in the same 'dead-weight' setup as the loading experiments (Fig. 3.1-3.2). Similar to the loading experiments the sample material is deposited between two 1 mm thick ring shaped Celeron sample holders and is thereafter placed in a disk-shaped container. The surface of the sample holders was roughened using sand paper. Additionally a ~ 3 mm thick Celeron ring is placed around the sample holders and sample material (Fig. 3.4). Using superglue the upper Celeron sample holder is glued to the Delrin POM piston, which in turn is glued to the weights. The lower sample holder is glued to the reservoir disk, which in turn is glued to the 'dead-weight' set-up. This is done so that the two ring shaped Celeron holders could rotate independently from each other.

A ~2 mm thick layer of muscovite-demi-water paste was distributed between the Celeron samples and placed in the Delrin POM container before gluing. Similar to the loading experiments the samples were loaded for 24 hours at an applied normal stress of 6.5 MPa before the sample was sheared. Then the sample was sheared by manually rotating the weight clockwise for either a half, a whole or three complete turn(s). A complete turn was conducted between ~30-38 seconds, resulting in an average sliding/rotating velocity of roughly 1.5 mm/s. After shearing the samples were impregnated and sectioned using the same approach as outlined for the loading experiments.

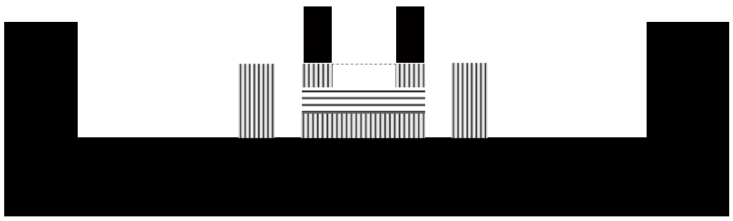

Figure 3.4 Schematic profile of set-up shear experiments

3.1.4 Microstructural analysis

Microstructures of the loading experiments were prepared by sawing the impregnated samples perpendicular to the loading direction and polishing the resulting thick sections. Microstructures of the shear experiments were prepared by sawing the impregnated perpendicular to the shear plane. All thick sections were carbon coated for Scanning Electron Microscope (SEM) analysis. Overview and detailed micrographs of the microstructure were acquired using a using JEOL-SEM. Some of the obtained images are a mosaic of more images. High resolution micrographs were analysed using JMicrovision, an image analysis program, to obtain 2D grain parameters and to determine the area fraction of SEM-visible porosity defined by setting a appropriate greyscale threshold.

3.2 Results: Microstructures Loading Experiments

3.2.1 Sample (mm) scale characteristics

SEM micrographs of the samples produced in the loading experiments are presented in Figure 3.5 and show both the sample and Celeron sample holders. The microstructures seen in these cross–sections can be separated into two domains: (i) a central domain, which is not in contact with the upper sample holder and thus was not loaded, (ii) and the outer regions, which are located between the upper and lower sample holder and thus were loaded. Extruded sample material is also observed adjacent to the loaded parts of the sample. It is clear from these micrographs that the loaded parts of the muscovite samples are thinned significantly compared to the non-loaded parts in all experiments, having a considerably lower porosity. The thickness of the loaded layer between the sample holders varies between 100µm and 150µm for the different experiments and is not constant over the width of the loaded area. No noticeable correlation between the applied normal stress and layer thickness is observed. Note that at the highest normal stress the central domain of the sample is broken up in multiple pieces. This is not observed in the other experiments.

3.2.2 Textural (100-500µm) characteristics

The microstructures of the loaded parts of the different samples are shown in Figure 3.6. In this figure, one of the two loaded parts visible in Figure 3.5 is shown and the edges of the microstructures are adjacent left to the extruded sample material and the non-loaded material in the centre of the sample is to the right. Detailed SEM images of the central region of Figure 3.6 are shown in Figure 3.7, i.e. Figure 3.7 shows the central region of the loaded sample parts. All samples are dense with a lower porosity at the centre of the sample than at their sides (i.e. adjacent to unconfined material). A broad correlation between the applied load and sample porosity is observed, being characterized by a decrease in the porosity with an increase in the load. The SEM-visible porosity was estimated to be ~15% for the samples loaded at 1.9, 2.8 and 6.5 MPa, as opposed to ~5% for the sample loaded at 12.1 MPa.

The long axes of the phyllosilicate grains are in general orientated (sub)-perpendicular to the loading direction, forming a foliation roughly perpendicular to the loading direction**.** The alignment of grains is strongest in the centre of the sample and becomes progressively less near the extrusion points (Fig. 3.6). Although the main foliation is sub-perpendicular to the applied loading axis, some rhomboidal shaped domains are present, giving the foliation a wavy appearance. These domains have a thickness varying between 10-40µm and occasionally contain grains with a different orientation than the main foliation (Figure 3.7). (Sub)-vertical bands of small grains and with a higher porosity are also present in the samples. Finally, small cracks at the sample boundaries are found in all samples, most notably in the sample that has undergone the highest load.

3.2.3 Grain (0.1 µm-10µm) scale characteristics

Individual phyllosilicate grains are thin and platy (Figures 3.7 and 3.8), with a mean width varying between 10 and 30 µm and a mean thickness of 1-5 µm. Aspect ratios of the grains are mostly in the range between 8:1 and 15:1, but may be as high as 20:1. Very fine, sub-micron grains are occasionally observed, usually associated with regions of higher porosity and/or near horizontal contact areas between bigger grains.

The long axes of the phyllosilicate grains are roughly perpendicular to the loading direction, defining a horizontal foliation. As a result, grains are both in dominated by horizontal contacts between grains. The nature of this contact varies and typical examples are shown in Figure 3.8.

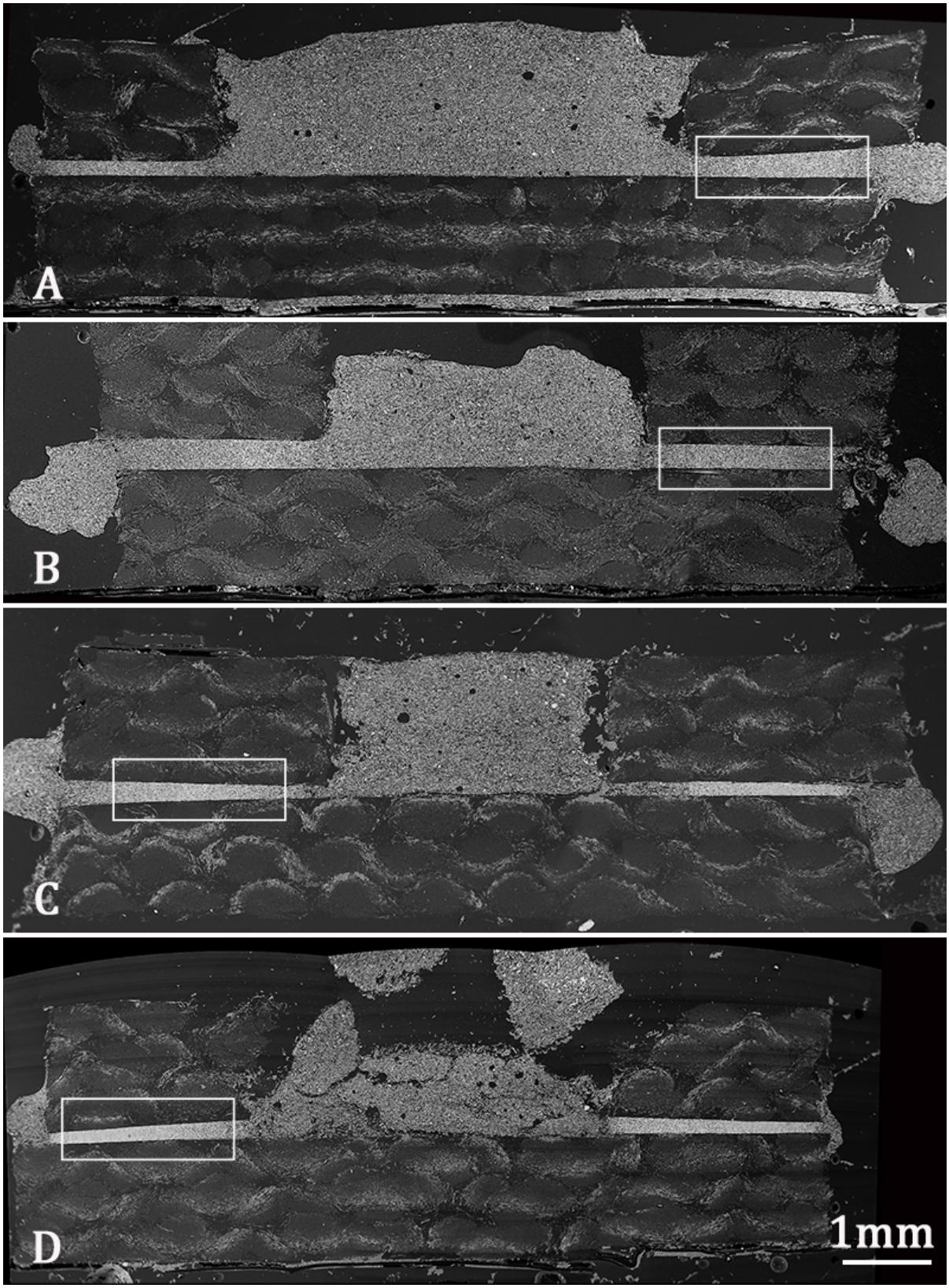

Figure 3.5 : SEM backscattered images presenting an overview of the cross-sections through sample and sample holders. Experiments were done at a) 1,87 MPa, b) 2,75 MPa, c) 6,5 MPa d) 12,1 MPa applied stress. White rectangles highlighted areas which are shown in detail in Figure 3.6

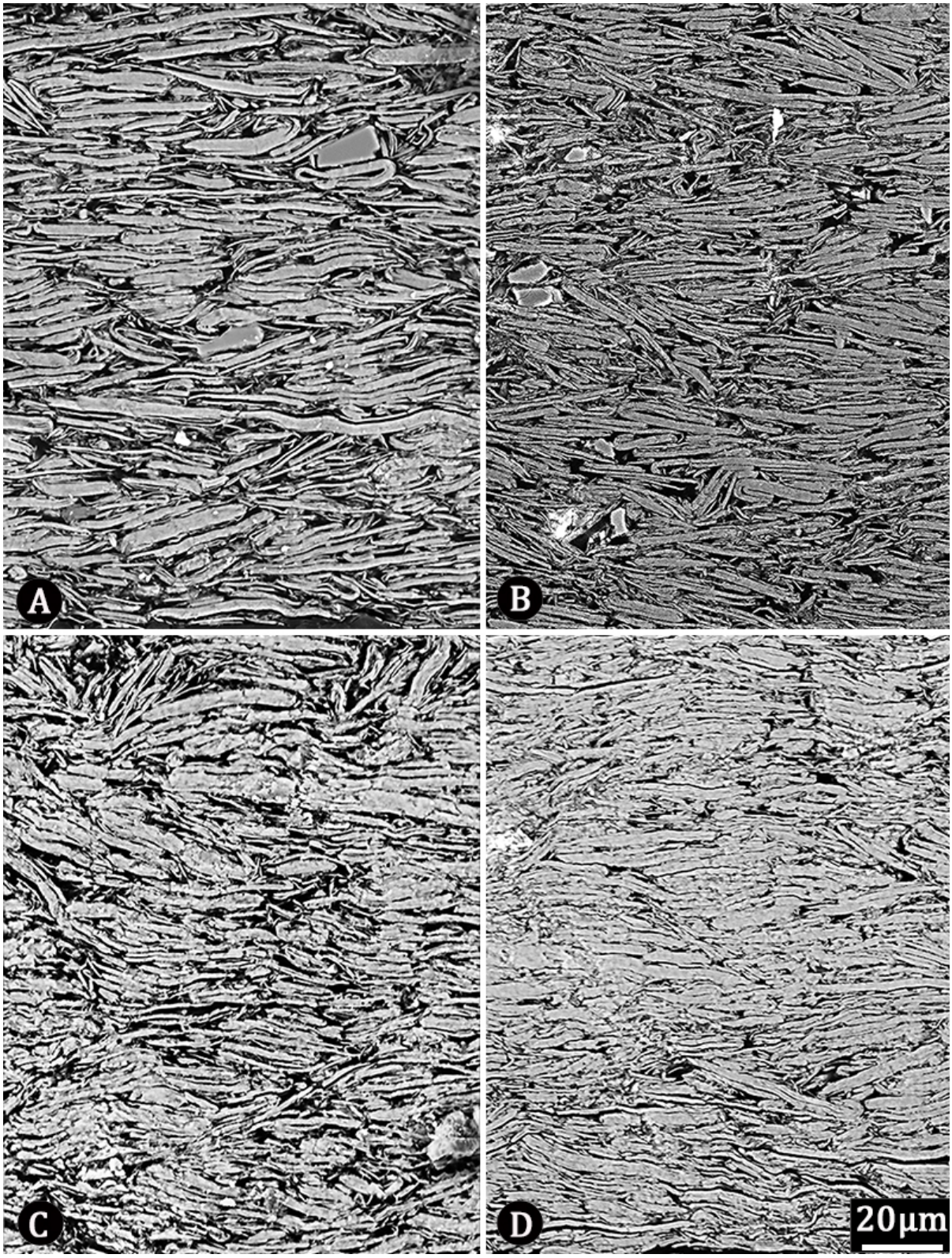

Figure 3.7 SEM backscattered images showing details of the microstructure of the middle part of the samples for the different loads. a) 1,87 MPa, b) 2,75 MPa, c) 6,5 MPa d) 12,1 MPa applied stress

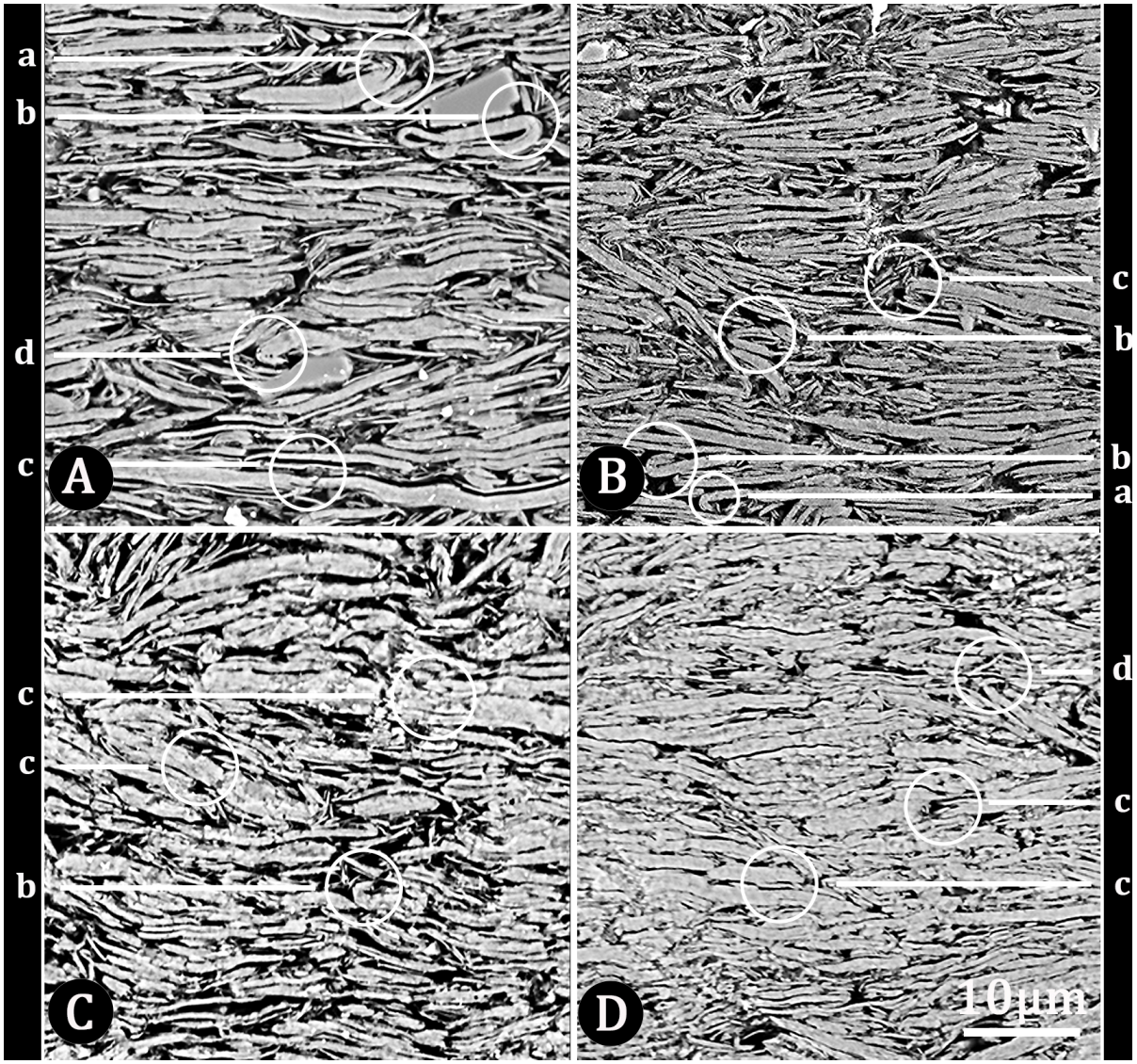

Figure 3.8 SEM backscattered images showing details of the microstructure of the middle part of the samples for the different loads. A) 1,87 MPa, B) 2,75 MPa, C) 6,5 MPa D) 12,1 MPa applied stress. a) frayed and bent grain in contact b) Completely folded up grains c) Opening (along 001 plane) of grains in contact d) Ductile bent grain in contact

Often, one or both of the grains are bent (Figures 3.8a-d) or even completely folded up (Figures 3.8a,b). Many of the contact points of the folded grains look frayed or are split multiple times (Figures 3.8a-c). When no folding occurs at the horizontal contact between grains, evidence of the splitting of the grains is often observed (Figures 3.8a-b.) Grains are also in contact with each when one of the grains is misaligned compared to the main foliation (3.8b-d).

With increasing normal stress, the grains change from roughly rectangular in shape (1.9 and 2.8 MPa) to a more 'wavy' shape (6.5 and 12.1 MPa). In addition, grains in the sample loaded to 12.1 MPa are in general thinner. There seem to be more grains that are folded in the sample compacted at 1.9-6.5 MPa normal load than at 12.1 MPa. The size of the grains is not affected substantially by the normal stress.

3.3 Results: Shear Experiments

Multiple shear experiments were conducted, but in most experiments to0 little or no sample material was left after shearing to obtain useful microstructures. Only from the experiment conducted at applied normal stress of 6.5 MPa and one complete turn sufficient sample material was left to obtain useful micrographs.

3.3.1 Sample (mm) scale characteristics

A SEM micrograph of the sample produced by the shear experiment conducted at 6.5 MPa applied normal stress with a strain rate estimated in the order of ~1-2 mm/s and a total estimated strain between ~25-50 is presented in Figure 3.9 and shows both the sample and Celeron sample holders. The sheared muscovite sample is thinned significantly compared to the initial thickness of ~2mm and has a thickness varying between 20-40 µm. This is also a considerable thickness reduction compared to the sample that was only loaded with a 6.5 MPa applied normal stress. Similarly as in the load experiments extruded sample material is observed adjacent to both sides of the sheared sample layer. The thickness as well as the porosity of the sheared sample layer is higher at both edges than in the middle of the sample. The micrograph presented in Figure 3.9 is a cross section taken along the ring shaped sample holder and not through the unloaded centre. Therefore no unloaded central region is present in the micrograph, in contrast to the micrographs of the load experiments where this central unloaded region is present.

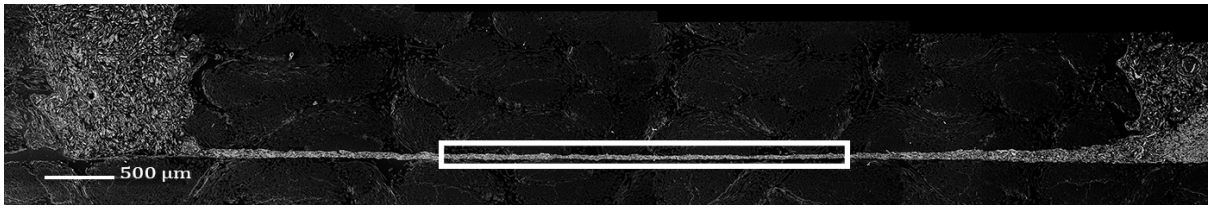

Figure 3.9 SEM backscattered image presenting an overview of a cross-section through sample and sample holders of shear experiment. The white rectangle highlighted areas which are shown in detail in Figure 3.6

3.3.2 Textural (100-500µm) characteristics

The microstructure of the central part of the sample, indicated with a white rectangle in Figure 3.9, is shown in Figure 3.10. The microstructure observed is a compact aggregate and has SEM-visible porosity of ~ 13 %. This SEM-visible porosity is similar to that observed in the sample from the loading experiment at 6.5 MPa applied normal stress, which had a porosity of ~15%.

The sheared microstructure is characterized by a foliation of aligned phyllosilicate grains, mostly orientated with their long axes ~20 to ~ 45 degrees to the shear plane. In some areas the grains are orientated sub-horizontal or have an orientation ~10-20 degrees against the shear plane. This gives the foliation an anastomasing character. Grains near the sample boundary are generally orientated with their long axes parallel to the shear plane and some of the grains near the boundaries are bent in the direction of the shear plane. Some small areas of around 10-20 µm thick with (folded) grains with a different orientation from the overall orientation are observed (but are not as common as in the loading experiments. Apart from the main foliation also much smaller phyllosilicate grains are present (mostly in pore areas) with no apparent structure. In the surface grooves very compact structures with a low porosity and little apparent structure are seen. Lastly, a couple of cracks are present in the samples, usually near the sample boundaries.

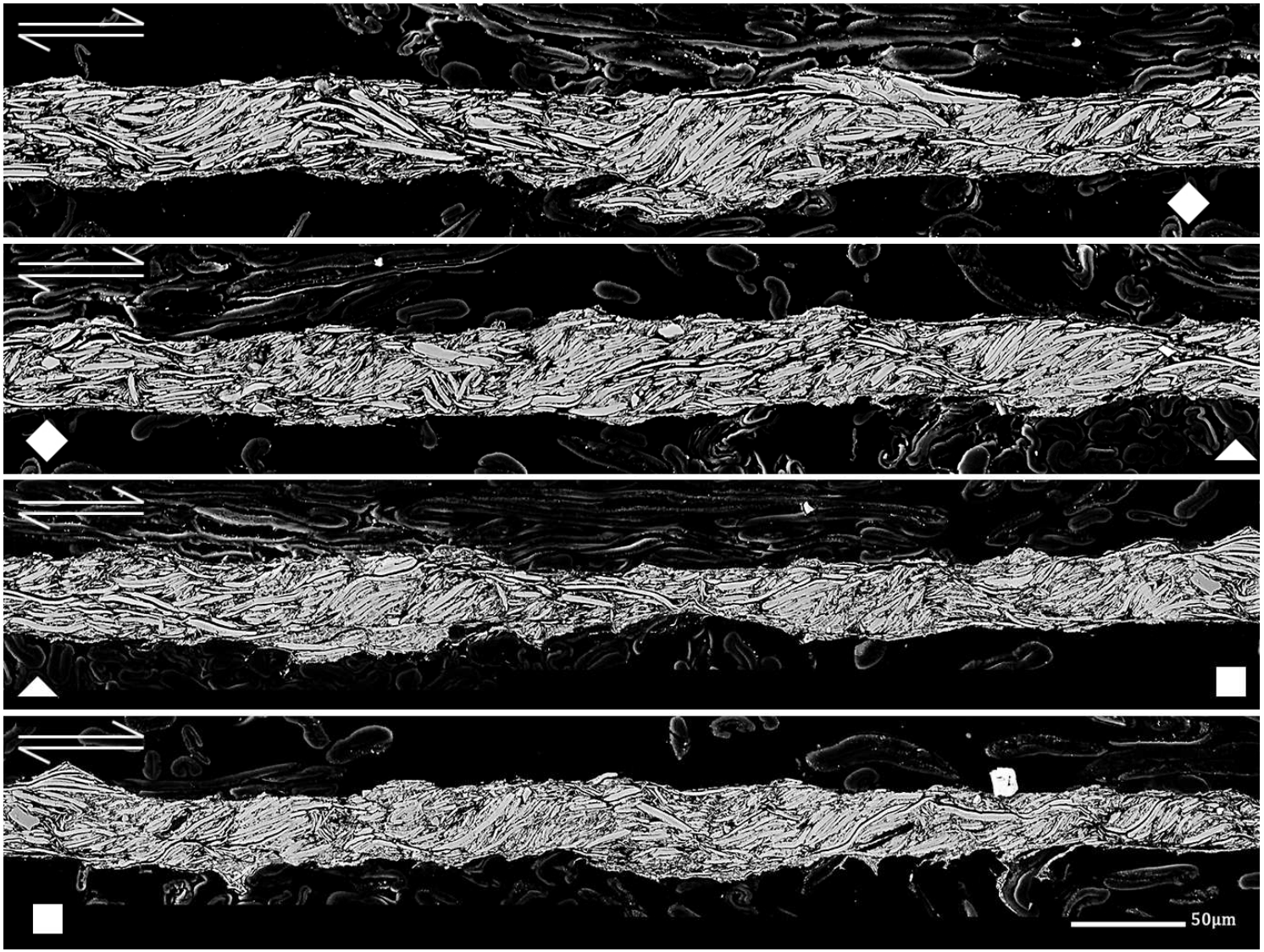

Figure 3.10 SEM backscattered images presenting a close up view of the highlighted area in Figure 3.9. The different geometrical objects Indicate overlapping points between the subsequent images.

3.3.3 Grain (0.1-10μm) scale characteristics

Detailed microstructures of Figure 3.10 are shown in Figure 3.11. The individual grains that make up the main foliation are plate-like. The length of the long axes of these grains varies between ~20-~35μm and the length of their short axes between ~2-~4μm, with aspect ratios ranging from 1/6 to 1/13 and a main aspect ratio of roughly 1/10. Most of these grains are thicker in their middle than at their edges. Apart from the bigger grains supporting the aggregate structure a significant amount of very small grains, with long axes of ~1 -~3 μm and short axes ranging from 150nm or to ~ 500 nm, are found in the samples.

. The grains making up the main foliation are commonly aligned with the grains adjacent to them and are both in vertical as well as in horizontal contact with their neighbours. The nature of this contact varies between contacting edges and typical examples are shown in Figure 3.11. i) Many of the edges are in contact with one of the grains is bent over/into the neighbouring grains. ii) It is often observed that one or both grains in contact are split (in the 001 plane orientation). Grains are sometimes split multiple times and occasionally almost the whole grain is split. iii) Lastly, some of the contacting grains show more heavily deformation, being (completely) folded up at the contact points. Compared with load experiments the contact between the grains is much less dominated by ductile deformation and folding of contacting grains.

The edges of the contacting grains commonly have a frayed character due to the splitting of the grains and the presence of small cracks. The SEM visible cracks are usually around 0.25-1 μm, but in some grains they can be as big as 2μm.

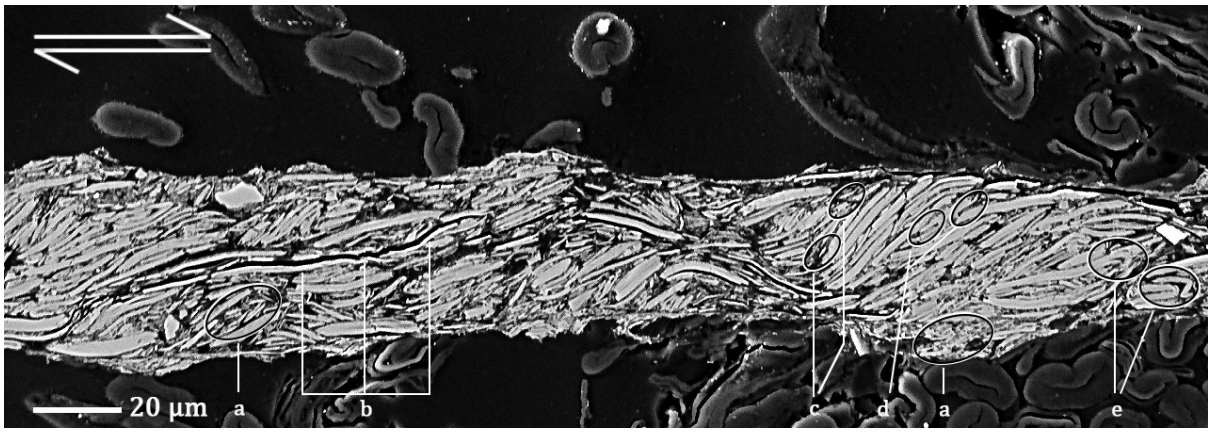

Figure 3.11 SEM backscattered image showing a detailed image from Figure 3.11. a) shows(very) small grains, b) shows a crack, c) shows contact between adjacent grains d) contact between neighbouring grains where one grain is bent over the other grain. e) contact between neighbouring grains were grains in contact are completely folded

3.4 Discussion

The microstructures of the compacted phyllosilicate aggregates show the following main characteristics. Firstly, the horizontal foliation and aligned of adjacent grains shows clearly that grains are both in vertical and in horizontal contact with neighbouring grains. Secondly, a decrease in porosity and hence increase in grain contact area with increasing normal stress is interpreted as the result of compaction of the samples. Thirdly, abundant evidence for ductile deformation as well as cleavage of grains is found in the experiments. Lastly, the edges of the grains show imperfections of the order of 0.5-1μm, which could act as stress concentrators facilitating failure of the grains.

The microstructure of the sheared phyllosilicate aggregates shows the following main characteristics. Firstly, the orientation change from the sub-horizontal foliation in the compacted microstructures to a foliation with grains with a main orientation of ~20-40 degrees in the shear experiment is consistent with dextral shear. Secondly, the alignment of the grains shows that not only in compaction but also during shearing grains are both in vertical and horizontal contact with each other. Thirdly, the abundance of very small grains and the fact that

bigger grains are often less thick at their edges is interpreted as brittle failure of (most likely) the edges of grains during shearing. Compared with the compacted microstructures, sheared microstructures show less evidence of ductile deformation and it is therefore likely that during shearing ductile deformed grains were broken. From these observations, it is clear that during frictional sliding of grains interactions at the grain scale level (i.e. failure of edges of grains) occur and could potentially be controlling friction in phyllosilicates. Lastly, similar to the compacted microstructure the edges of the grains in the shear microstructure show imperfections of the order of 0.5-1μm, which could have acted as stress concentrators facilitating the failure of the grains as seen in microstructures. Ideally, all of these characteristics should be incorporated in a microphysical model.

In both types of experiments the aim was to eliminate experimental artefacts from the microstructure, such as features introduced by unloading the sample. Wavy foliation of aligned grains is similar to compacted microstructures seen by Lu and He, 2014 without the unloading features. Lorenze shaped domains could be precursors to sigmoidal shaped domains seen in literature. The approach used in impregnating the sample therefore looks to have been successful.

It is not likely that artefacts were introduced by impregnating the sample while under load since i) the central domain of the samples which were not loaded have a chaotic structure which is to be expected if the epoxy resin had no effect on the microstructure. If the epoxy resin had an effect then certainly in the non-loaded part some kind of structuring should occur. ii) In the loaded part of the samples, near the extrusion points, the microstructure is more chaotic than in the middle. If the aligned structure was caused by the introduction of the epoxy resin then this aligned structure would be distributed throughout the sample.

The large cracks near the sample holders present in all samples are the result of sample preparations. In order to get the epoxy disk out of the reservoir the disk had to be bent, which in all likelihood caused these cracks to form. It should be noted that since the sample material was not confined at its sides in the shear experiments a considerable amount of volume loss occurred, evidenced by a two to three time thickness reduction compared to the compacted microstructure at a similar applied normal stress. Lastly, the non-uniform thickness of the compacted samples is the result of asymmetrical loading of the samples.

4 Microphysical models for friction of dry phyllosilicates

In this section, a microphysical model for the steady state frictional sliding of dry phyllosilicates at temperatures ranging from low (room temperature) to intermediate temperatures (~400 ^{0}C) is developed. This temperature range is selected because at these temperatures, the microstructures are easier to interpret than microstructures observed at higher temperatures and the frictional behaviour is better constrained by previous experimental studies. The model is based on the frictional behaviour and microstructures of sheared pure phyllosilicate friction reported in previous studies and described in the literature described in section 2, as well and as on the results of the friction compaction and shear experiments described in section 3. The main features a microphysical model on dry phyllosilicate friction needs to explain are the following observations:

1) The low frictional strength of dry phyllosilicates compared to other dry rock forming minerals.
2) The (linear) relation found by Moore and Lockner (2004) between the interlayer bond strength of phyllosilicate minerals and their frictional strength.
3) The velocity strengthening behaviour of phyllosilicates observed at room temperature.

In the following, the assumed main microstructural characteristics on which the models are based and the modelling approach are described first. Next, microphysical models are developed assuming frictional control of different scale of interaction between the grains. An explanatory list of symbols is given in Appendix 1.

4.1 Sample scale model microstructure and modelling approach

Starting point for the development of a microphysical model for dry phyllosilicate friction is the definition of an idealised microstructure. In section 2 of this study, the steady state microstructures of dry and wet phyllosilicates sheared at temperatures up to ~400 ^{0}C are described in detail. In summary, these microstructures were characterized by an anastomosing foliation of aligned, fine-grained phyllosilicates that folds around sigmoidal shaped regions. The anastomosing foliation commonly consists of intersecting P-, Y-, R- and boundary shears, of which the Y-shears are in general most common, whereas the sigmoidal regions often contain coarser, less deformed phyllosilicate grains with orientations different from the bulk foliation (e.g. Moore and Lockner, 2004; Van Diggelen et al., 2010; Den Hartog et al., 2013; Haines et al., 2013 and Lu and He, 2014).

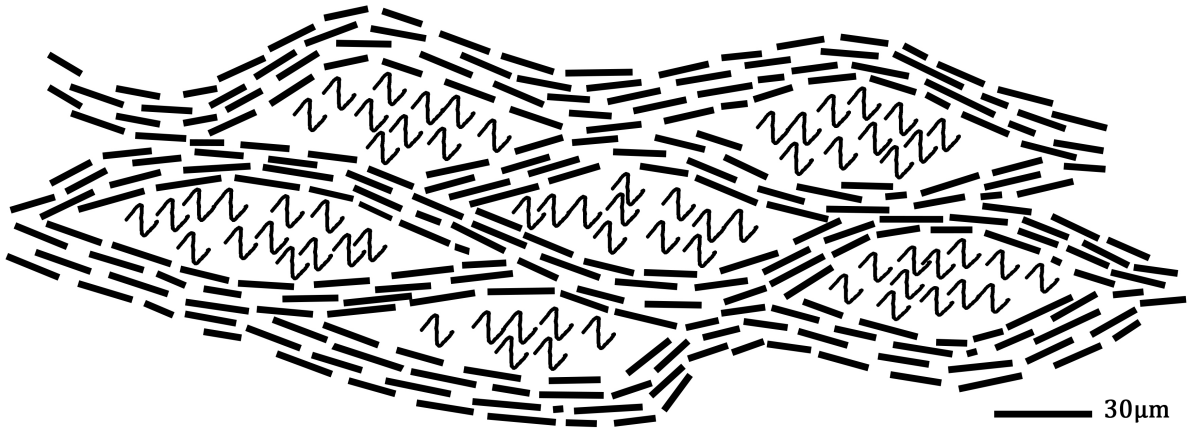

Figure 4.1 Idealized schematic microstructure of sheared phyllosilicates

Based on these microstructural observations in the literature and this study, the shear deformation in the idealised microstructure (Fig. 4.1) can be accommodated by localised deformation in the anastomosing shear bands and/or by deformation of the sigmoidal clasts. In this study the sigmoidal clast were not observed prominently. Furthermore it is assumed that the microstructure is supported by the anostomasing shear bands and not by the clasts. Therefore, it is assumed here that the deformation of shear bands controls the frictional behaviour of phyllosilicates. Within these shear bands, the grains are aligned and in contact with each other along horizontal planes. In addition, the edges of most of the adjacent grains are assumed to contact each other along vertical planes. The individual platy phyllosilicate grains are taken to be rectangles with dimensions $a:a:b$, where a is the dimension parallel to the sheet (i.e. the long axis) and b the dimension perpendicular to the sheets (i.e. length of the short axis. The smallest possible repeating structure of the microstructure, the unit cell, is indicated in Figure 4.1. It is assumed that the interaction between the grains along the horizontal planes is at the grain scale, whereas it is at the atomic and the asperity scale along the vertical planes of contact (Fig. 4.2).

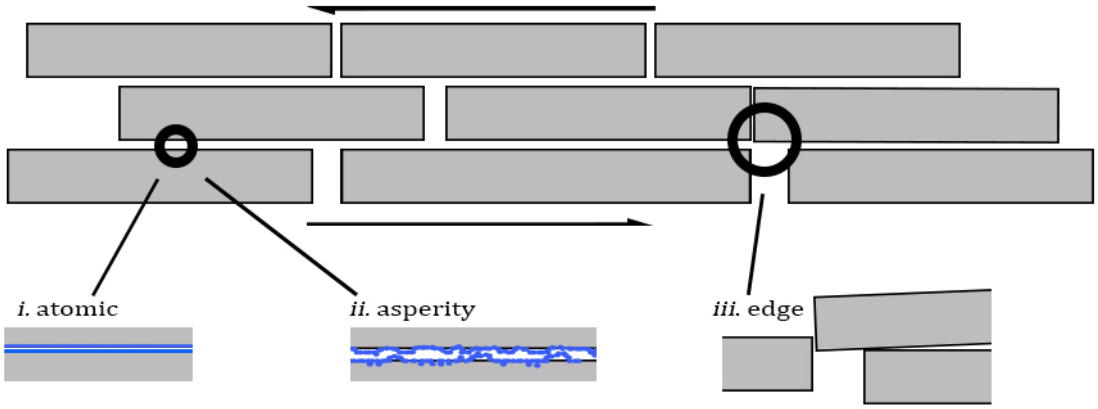

Figure 4.2 Schematic overview of scale of interaction between grains during frictional sliding

Frictional slip in the shear bands is assumed to be accommodated by sliding of the individual grains over each other. The interactions at the different scales (i.e. atomic, asperity or grain scale) between the grains will cause resistance to sliding and thus determines the frictional behaviour at the grain scale. Since the frictional sliding of the grains accommodates the deformation in the shear bands, which in turn accommodates the deformation at sample scale, the macroscopic frictional behaviour is ultimately determined by the interactions between the individual grains.

To evaluate which scale of interaction between the grains, i.e. atomic, asperity or grain scale, controls the observed macroscopic frictional behaviour, microphysical models are developed, each assuming friction control at a different scale of interaction. In each model, the active processes are evaluated and the accompanying microscopic forces are quantified for the unit cell, using dissipation theory. The microscopic forces are subsequently translated into the macroscopic forces acting on the phyllosilicate aggregated, using a force balance. From the resulting macroscopic forces, predicted frictional parameters are calculated, using muscovite as an example. In this study, only the atomic scale and the interaction between the edges of the phyllosilicate grains are evaluated. The asperity scale is not evaluated in this study since friction sliding controlled by asperities is already studied extensively in the literature **(**e.g. Baumberger, 1999; Rice et al., 2001)

4.2 Atomic scale barrier model

In the first microphysical model it is assumed that the frictional behaviour of phyllosilicates is controlled by atomic scale interactions between the grains, such as van der Waals forces. Atomic scale processes are expected to control the macroscopic behaviour if interactions between the sliding grains at scales larger than the atomic scale do not exist or offer a lower frictional resistance to sliding than the atomic scale interactions. Here, the latter is assumed. For example, interactions between contacting grain edges are assumed to cause negligible resistance.

4.2.1 Model microstructure and deformation mechanisms

If atomic scale processes control the macroscopic friction there is either i) no interaction between the sliding grains at scales larger than the atomic scale or ii) these interactions offer a lower frictional resistance to sliding than the atomic scale interactions. A schematic microstructure for a phyllosilicate aggregate in which only atomic scale interactions offer the resistance to shear is shown in Figure 4.3. In this model microstructure, the grains are separated by a distance *S* along vertical planes. The porosity ϕ is defined as the ratio of the pore volume to the total volume of the unit cell and given as:

$$\phi = \frac{Volume\ pores}{Volume\ unit\ cell} = \frac{2Sba}{2ba(S+a)} = \frac{S}{(S+a)} \qquad (4.1)$$

In this model microstructure, movement of the phyllosilicate grains with respect to each other is assumed to occur via atomically controlled friction.

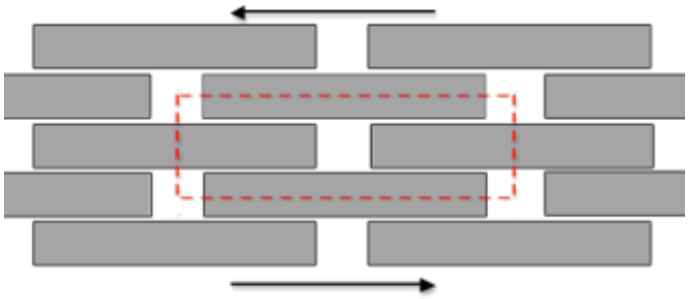

Figure 4.3a Schematic 2-dimensional representation of the microstructure of the atomic friction controlled microphysical model. The dotted red lines highlight the area of the unit cell.

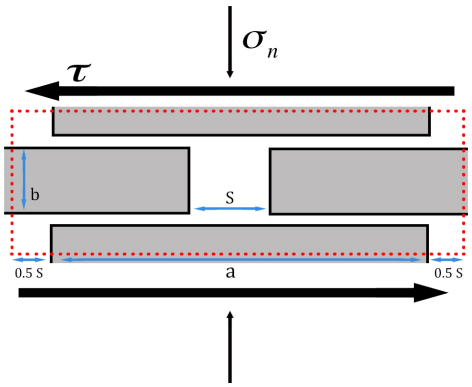

Figure 4.3b Unit cell of microphysical model for atomic controlled friction. In this figure *S* is the average horizontal distance between the phyllosilicate grains, *b is* the height of an individual grain and *a* is the width of a grain.

4.2.2 *Force balance*

To evaluate the frictional resistance caused by the atomic scale processes, the microscopic normal and shear forces acting in the unit cell are evaluated. The forces acting within the unit cell have to be balanced by the normal and shear forces acting macroscopically on the unit cell.

The microscopic normal force is equal to the product of the microscopic normal stress $\tilde{\sigma}_n$ and the load supporting area, which is $2(a-S)a$ per unit cell. This force is balanced by the macroscopic normal force, determined by the macroscopic normal stress σ_n acting on the total area of the unit cell $(a+S)a$. Similarly, the microscopic shear stress $\tilde{\tau}$, acting over grain contact area per unit cell is balanced by the macroscopic shear strength τ acting on the total area of the unit cell.

These balances are given by, respectively

$$2\tilde{\sigma}_n(a-S)a = \sigma_n(a+S)a \quad (4.2)$$

$$2\tilde{\tau}(a-S)a = \tau(a+S)a \quad (4.3)$$

Using these relations, and assuming that the microscopic shear and normal stresses are related via an atomic coefficient of friction for dry friction $\tilde{\mu}$, the following relation between the macroscopic stresses is obtained:

$$\tilde{\tau} = \tilde{\mu}\tilde{\sigma}_n \rightarrow \tilde{\mu} = \frac{\tilde{\tau}}{\tilde{\sigma}_n} \quad (4.4)$$

$$\frac{2\tilde{\sigma}_n(a-S)a}{2\tilde{\tau}(a-S)a} = \frac{2\sigma_n(a+S)a}{2\tau(a+S)a} \rightarrow \frac{\tilde{\sigma}_n}{\tilde{\tau}} = \frac{\sigma_n}{\tau} \rightarrow \frac{\tilde{\sigma}_n}{\tilde{\tau}} = \mu$$

$$\tilde{\mu} = \mu \quad (4.5)$$

4.2.3 *Predicted macroscopic frictional parameters*

The above microphysical model for friction controlled by atomic scale interactions predicts that the macroscopic frictional behaviour of dry phyllosilicates is controlled by the atomic friction coefficient $\tilde{\mu}$. Studies on atomic controlled friction and the atomic friction coefficient $\tilde{\mu}$ are scarce. Liu et al. (1998) found an atomic coefficient of friction of 0.045 for muscovite using nanoscale Atomic Force Microscopy (AFM). Bucholz et al. (2012) studied atomic scale friction of pyrophyllite using AFM and obtained an atomic scale friction coefficient of ~ 0.03. Data on the velocity and temperature dependence of the atomic friction coefficient are non-existent, but such a dependence seems unlikely, given that processes like the van der Waals forces are time and temperature independent.

Observations on atomic scale frictional behaviour demonstrate that the assumption made that atomic scale interactions are frictional, is valid, certainly when the applied load is relatively low (Israelachvili et al., 1995; Bushan et al., 1995; Krim et al., 2011). However, for higher loads, the coefficient of friction has been found to increase with applied normal stress (Israelachvili et al., 1995; Bushan et al., 1995). When this is the case, wear of the material is generally also observed. This means that processes that act on a bigger scale than the atomic scale begin to have an influence on friction (Homola et al., 1989; Bushan et al., 1995).

4.3 Grain scale barrier models

In the second microphysical model is it is assumed that the frictional behaviour of phyllosilicates is controlled by grain scale interactions. This is the largest scale of interaction considered here and takes place at the edges of adjacent grains. Such interactions have been ignored by previous authors (e.g. Moore and Lockner, 2004; Haines et al., 2013). They, however, inevitably occur, which is evident from our microstructural observations in Chapters 2 and 3. Therefore, it is important to quantify the resistance as a result of the interactions between the edges of the sliding grains and evaluate whether such interactions can explain the observed frictional behaviour of phyllosilicates.

4.3.1 *Model microstructure and deformation mechanisms*

In this microphysical model, it is assumed that the shear band porosity, ϕ, is a key factor determining the deformation mechanisms. The porosity results from the horizontal distance between adjacent grains and is given by

$$\phi = \frac{Volume\ pores}{Volume\ unit\ cell} = \frac{2Sba}{2ba(S+a)} = \frac{S}{(S+a)} \tag{4.6}$$

When grains slide past each other, the top grain is assumed to bend into the underlying pore, bringing the edges of adjacent grains into contact (Figure 4.4). The strain in this case is thus accommodated by the serial processes of frictional slip along the horizontal contact and internal deformation of the (top) grain to overcome the edge contact.

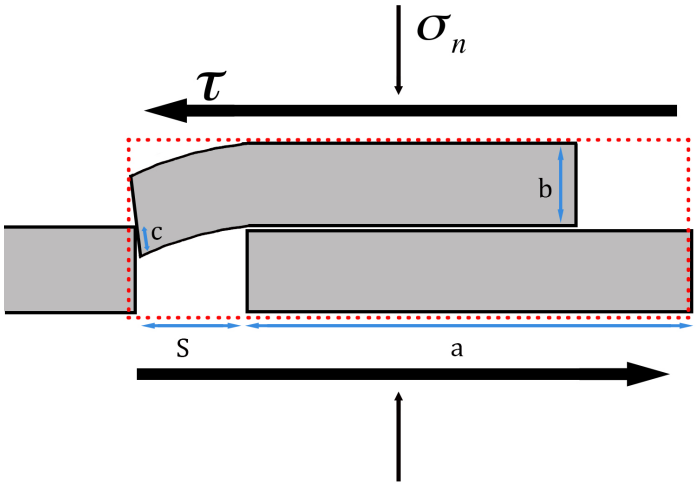

Figure 4.4 Schematic representation of the unit cell used for the edge contact model. S here represents the average distance between the grains, a and b represent the length and height of the phyllosilicate grain respectively. c is the vertical length of contact between the grains. Lastly, τ and σ_n are the macroscopic shear and normal stress respectively.

The bending of the top grain can occur by various deformation mechanisms, yielding different amounts of grain overlap or *c*. Similarly, subsequent deformation of the top grain to move past the edge of the bottom grain can occur by several failure mechanisms. Since different mechanisms can potentially result in different macroscopic frictional behaviour, all possible deformation and failure mechanisms will be analysed. In the following, the frictional resistance caused by contacting grain edges will first be derived in general terms, which is valid regardless of the specific deformation or failure mechanism. Next, the shear strength will be quantified for different possible deformation mechanisms of grain bending, yielding different grain overlaps. This is followed by an evaluation of the force required to overcome the edge contact by various failure mechanisms**.** Lastly, all different combinations of deformation and failure mechanisms are cast into separate microphysical models.

4.3.2 Force balance

In this model microstructure, the macroscopic normal force, $\sigma_n a^2$, is supported by the microscopic normal stress $\tilde{\sigma}_n$ acting on the unit cell contact area of $(a - S)a$, yielding:

$$\sigma_n a^2 = \tilde{\sigma}_n (a - S)a$$
$$\tilde{\sigma}_n = \frac{\sigma_n a}{(a - S)} \quad (4.7)$$

The macroscopic shear force acting on the unit cell, τa^2, in turn, is supported by the microscopic shear stress $\tilde{\tau}$ acting on the area $a(a - S)$ plus the force required for the grain to overcome the edge contact F_{edge}, i.e.

$$\tau a^2 = \tilde{\tau} a(a - S) + F_{edge}$$
$$\tau = \frac{\tilde{\tau} a(a - S)}{a^2} + \frac{F_{edge}}{a^2} \quad (4.8)$$

When it is assumed that sliding along the horizontal contact area is controlled by atomic scale frictional behaviour (cf. section 4.2), $\tilde{\tau}$ can be written as:

$$\tilde{\tau} = \tilde{\mu}\tilde{\sigma}_n$$

Using equation (4.7), this becomes:

$$\tilde{\tau} = \tilde{\mu}\left(\frac{\sigma_n a}{a - S}\right) \quad (4.9)$$

Substituting equation (4.9) into (4.8) now yields:

$$\tilde{\tau} = \tilde{\mu}\left(\frac{\sigma_n a}{a - S} \times \frac{a(a - S)}{a^2}\right) + \frac{F_{edge}}{a^2} = \tilde{\mu}\sigma_n + \frac{F_{edge}}{a^2} \quad (4.10)$$

The force needed to overcome the resistance at the edge contact of area ca depends on the shear strength of the edge contact τ_{edge}, i.e.

$$F_{edge} = \tau_{edge} ca \quad (4.11)$$

The macroscopic shear stress needed for frictional sliding is then obtained by combining equations (4.9) and (4.10):

$$\tau = \tilde{\mu}\sigma_n + \frac{\tau_{edge} c}{a} \quad (4.12)$$

The vertical contact length *c* can be expressed in terms of the normal stress. Bending of the top grain into the pore can occur via various deformation mechanisms, yielding different relations between the vertical overlap distance *c* and the normal stress. These relations are determined for bending of the upper grain by elastic deformation, time-independent ductile deformation and time-dependent ductile deformation.

4.3.2.1 *Elastic deformation*

First, the scenario is considered in which the edges of the adjacent grains come into contact as a result of elastic bending of the upper grain. If it is assumed that compaction of the phyllosilicate aggregate under the applied normal stress is primarily caused by the bending of grains into the pores and it is assumed that the effect of the vertical compaction of the individual grains is assumed to be negligible, the vertical strain ε_n is approximately equal to:

$$\varepsilon_n \approx \frac{c}{b} \tag{4.13}$$

From elasticity theory, the vertical strain is defined as:

$$\varepsilon_n = \frac{\sigma_n}{E_a} \tag{4.14}$$

where E_a is Young's modulus of the phyllosilicate aggregate. Combining equation 4.13 and 4.14 leads to an expression for c as a function of the applied normal stress.

$$c = \frac{b}{E_a}\sigma_n \tag{4.15}$$

Combining (4.11) and (4.15) gives the relation between the macroscopic shear stress and the macroscopic normal stress for a contact area between grains due to elastic bending of the grains

$$F_{edge} = \tau_{edge}\frac{ab\sigma_n}{E_a} \tag{4.16}$$

$$\tau_{elastic} = \left(\tilde{\mu} + \tau_{edge}\frac{b}{E_a a}\right)\sigma_n \tag{4.17}$$

4.3.2.2 *Time independent ductile deformation*

The second scenario considered is the scenario in which the bending of the top grain is the result of ductile, time independent deformation. Time independent ductile deformation is the result of a competition between work hardening, due to dislocation multiplication and increased interaction of dislocations with increasing deformation on the one hand, and recovery processes on the other hand. These recovery processes work against hardening by reducing dislocation density by annihilation and by enabling dislocations to untangle. It is assumed that work hardening processes control the deformation of the bent top grain. This allows expression of the grain overlap *c* in terms of the normal stress.

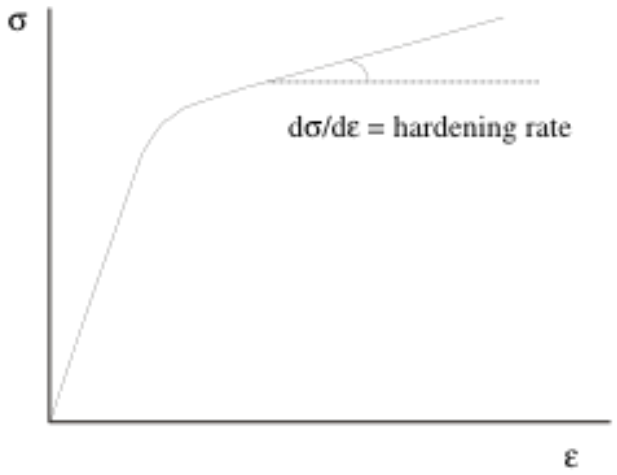

Figure 4.5 General relation between the stress and strain for work hardening controlled deformation

Figure 4.5 shows a schematic representation of the relationship between the normal stress and the strain for work hardening ductile deformation. From this figure, it follows that the relation between the normal stress and strain for a work hardening process is:

$$\sigma_n = \sigma_{yield} + \frac{d\sigma_n}{d\varepsilon_n}\varepsilon_n \qquad (4.18)$$

where σ_{yield} is the yield stress, i.e. the normal stress needed before ductile deformation initiates and $\frac{d\sigma_n}{d\varepsilon_n}$ or $\dot{h}$ is the hardening rate. For normal stress below the yield stress only elastic deformation occurs.

The vertical strain ε_n of the phyllosilicate aggregate is assumed to be primarily the result of bending of the phyllosilicate grains into the pores and the effect of vertical compaction of the individual grains is assumed to be negligible, as was done in the elastic bending scenario. **T**he total vertical strain is the result of the strain caused by elastic bending of the grains $\varepsilon_{elastic}$ plus the strain caused by bending of the grains due to work hardening plastic deformation $\varepsilon_{plastic}$.

$$\varepsilon_n = \varepsilon_{elastic} + \varepsilon_{plastic} \qquad (4.19)$$

Combining equation 4.12 and equation 4.17 leads to the following expression of the vertical overlap distance c:

$$c = b\varepsilon_n = b(\varepsilon_{elastic} + \varepsilon_{plastic}) \qquad (4.20)$$

The contribution of the elastic deformation to the total vertical strain after yielding is the total strain due to elastic bending at yield point ε_{yield}.

$$\varepsilon_{elastic} = \varepsilon_{yield} = \frac{\sigma_{yield}}{E_a} \qquad (4.21)$$

The vertical strain due to plastic deformation, after a certain yield stress is overcome, is then:

$$\varepsilon_{plastic} = \frac{d\varepsilon_{plastic}}{d\sigma_n}\sigma_n \qquad \varepsilon_{plastic} = \frac{\sigma_n}{\dot{h}} \qquad (4.22)$$

Combining (4.12), (4.21) and (4.22) leads to an expression for c as function of the normal stress σ_n

$$c = b(\varepsilon_{elastic} + \varepsilon_{plastic}) \quad c = b\varepsilon_{yield} + b\frac{\sigma_n}{\dot{h}} \quad c = b\frac{\sigma_{yield}}{E_a} + b\frac{\sigma_n}{\dot{h}} \tag{4.23}$$

Combining (4.11) and (4.23) yields the relation between the macroscopic shear stress and the macroscopic normal stress for a contact area between grains as a result of time independent ductile bending of the grains, given by

$$\tau_{ductile} = \tau_{edge}\frac{b}{a}\frac{\sigma_{yield}}{E_a} + \left(\tilde{\mu} + \tau_{edge}\frac{b}{\dot{h}a}\right)\sigma_n \tag{4.24}$$

4.3.2.3 Time dependent ductile deformation

The third and last scenario considered here is that in which bending of the overlapping grain is the result of time dependent ductile deformation. Similar as was considered in section 4.3.2.1 above vertical overlap distance c is in this case the result of elastic bending and now a time dependent ductile deformation processes.

From the geometry of the unit cell (Fig. 4.4) it is clear that the bent grain is experiencing a shear strain γ of

$$\gamma = \frac{c}{S} \tag{4.25}$$

The shear strain rate is then given by the rate of change of c over time.

$$\dot{\gamma} = \frac{\dot{c}}{S} \tag{4.26}$$

Integrating with respect to time gives an expression for $c_{elastic}$ versus the time t and the shear strain rate $\dot{\gamma}$, i.e.

$$\frac{dc_{elastic}}{dt} = S\dot{\gamma}$$
$$\int dc_{elastic} = S\dot{\gamma}\int dt \rightarrow c_{elastic} = S\dot{\gamma}t \tag{4.27}$$

Mares and Kronenberg (2006) found that dislocation glide was the dominant time dependent deformation mechanism in their experiments on muscovite. Accordingly, it is assumed here that time dependent ductile deformation is accommodated by a dislocation glide process. The shear strain rate given in (4.26) is hence given as (Mares and Kronenberg, 2006):

$$\dot{\gamma} = A\exp(\alpha\tau)\exp(-Q/RT) \tag{4.28}$$

where *A* and α are experimental constants and Q is the activation energy.
The shear stress acting on the bent grain is assumed to be proportional to the normal stress on the phyllosilicate aggregate.

$$\tau \propto C\sigma_n \tag{4.29}$$

where C is a constant. This then leads to the following expression for the shear strain and the applied normal stress.

$$\dot{\gamma} = A\exp(\beta\sigma_n)\exp(-Q/RT) \tag{4.30}$$

where β is a new constant equal to $C\alpha$. Combining equations (4.15), **(**4.27**)** and (4.29) now gives an expression for the vertical overlap c as a function of the applied normal stress.

$$c = b\frac{\sigma_{yield}}{E_a} + SA\exp(\beta\sigma_n)\exp(-Q/RT)t \tag{4.31}$$

The time over which the top grain is allowed to bend into the pore, depends on the time t_{slide} it takes to slide over the pore at velocity v_{slide} and the time t_f for an edge contact to fail. The latter varies depending on the process by which the edge obstacle is overcome.

$$t = t_{slide} + t_f \qquad t_{slide} = \frac{S}{v_{slide}} \qquad t = \frac{S}{v_{slide}} + t_f \tag{4.32}$$

Incorporating (4.32) into (4.31) now gives:

$$c = b\frac{\sigma_{yield}}{E_a} + SA\exp(\beta\sigma_n)\exp(-Q/RT)\left(\frac{S}{v_{slide}} + t_f\right) \tag{4.33}$$

Finally, combining (4.12) and (4.33) yields a relation between the macroscopic shear strength and macroscopic normal stress for a time independent ductile bending process.

$$\tau_{ductile(t)} = \tilde{\mu}\sigma_n + \tau_{edge}\frac{b}{a}\frac{\sigma_{yield}}{E_a} + \left(\tau_{edge}\frac{SA\exp(-Q/RT)\exp(\beta\sigma_n)}{a}\left(\frac{S}{v_{slide}} + t_f\right)\right) \tag{4.34}$$

4.3.3 Edge contact failure mechanisms

As described by equation (4.12), the force needed to move the top grain past the edge of the bottom grain and to continue sliding depends on the contact area of the edges multiplied by the shear strength of this area. The shear strength of the edge contact depends on the failure mechanism by which the edge contact between the grains is overcome. Two failure mechanisms are analysed here, cleavage failure and Griffith type crack failure.

4.3.3.1 *Cleavage failure*

Brittle failure of minerals can occur by cleavage, the splitting of minerals along specific weaker crystallographic planes. The preferred cleavage plane of phyllosilicates is the 001 plane, as a result of weak 001 interlayer bonds (Putnis, 1992). Thus, cleavage occurs parallel to the *a* dimension of the current model phyllosilicate grains. The work done in cleaving a phyllosilicate mineral is proportional to the surface energy γ_s of the newly created area A (Israelachvili, 2011), though:

$$W_{cleavage} = \gamma_s A \tag{4.35}$$

Cleavage can result in either (i) one large piece of the top grain breaking off or (ii) multiple smaller pieces that are cleaved off. Both scenarios are considered here. The first possibility is schematically represented in Figure 4.6, showing that the overriding grain can overcome the edge obstacle by breaking of a large piece, which subsequently falls into the pore. This process creates the minimum amount of new surface area in overcoming the edge obstacle, resulting in the minimum force.

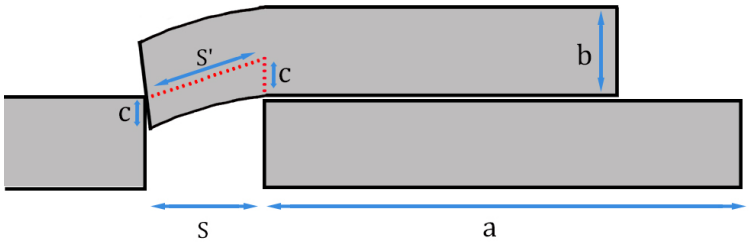

Figure 4.6 Schematic representation of interacting grains. The dotted red line denotes where the piece will break of.

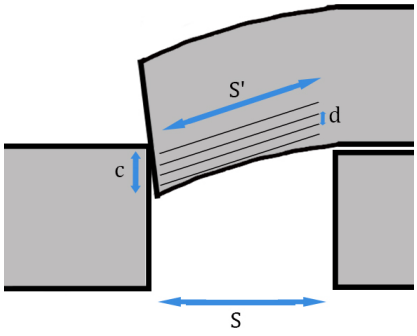

Figure 4.7 Schematic representation of interacting grains. The grey lines denotes where the pieces will break of.

Cleavage of the grain along only one plane creates two new surfaces with surface energy γ_s and a combined area of $(S^{'} + c)a \approx (S + c)a$. The work done in cleaving the grain is the force F_{edge} needed for cleavage over the horizontal distance S in which the cleaved grain is moved. This leads to a formula for the minimum force needed to overcome an edge contact by cleavage given by:

$$F_{edge C_{\min}} S = 2\gamma_s (S + c)a$$
$$F_{edge C_{\min}} = \frac{2\gamma_s (S + c)a}{S} \tag{4.36}$$

Figure 4.7 shows the alternative possible type of cleavage, i.e. the creation of a multitude of new surfaces by breaking the grain in to multiple smaller cleaved planes. The maximum area that can be created is proportional to the cleavage of every 001 plane that is in contact with the edge. This will lead to the maximum theoretical force that is required to overcome an edge due to cleavage. The

amount of cleavage planes in contact with the edge is given by the vertical contact distance c divided by the 001 lattice spacing $d_{lattice}$. The maximum force is then given by:

$$F_{edgeC_{\max}} S = 2\gamma_s Sa \frac{c}{d_{lattice}}$$
$$F_{edgeC_{\max}} = 2\gamma_s \frac{ca}{d_{lattice}} \quad (4.37)$$

Cleavage occurring on every 001 plane in contact with the edge of the bottom grain is a very unlikely scenario. It is more reasonable to assume that cleavage occurs only at some 001 planes in contact with the edges with an average distance d between them. The force required to overcome the edge contact by cleavage is then given by:

$$F_{edgeC} = 2\gamma_s \frac{ca}{d} \quad (4.38)$$

4.3.3.2 *Griffith type failure*

The second mechanism considered here for failure of the edge of the top grain is Griffith type failure (Griffith 1920, 1924). The observed discrepancy between the theoretical stress needed for breaking atomic bonds and the much lower actual stress needed for brittle failure led Griffith to the hypothesis that failure is caused by the presence of microscopic flaws. These flaws act as concentrators of stress. At the tip of such a flaw or crack the remote applied stress is intensified, meaning that a lower applied stress is needed to initiate rupture. Griffith obtained a criterion for the stress needed to propagate an elliptical crack in uniaxial compression using an energy balance. He considered the elastic energy released when a crack propagates and the work done in creating new crack surfaces. This resulted in to the following criterion for failure:

$$\sigma_c = \sqrt{\frac{2\gamma_s E_c}{\pi d_{crack}}} \quad (4.39)$$

where σ_c is the stress at failure, γ_s the surface energy, E_c the Young's modulus for a single crystal and d_{crack} the half width of an elliptical crack.

The microstructures of the loading experiments presented in Chapter 3 show that the edges of phyllosilicate grains have imperfections that can act as stress concentrators and facilitate failure similar to Griffith type cracks. A schematic representation of how a Griffith type failure in the edge contact model is envisioned is shown in Figure 4.8. It assumed that the crack fails in a tensile manner, i.e. the crack is a mode I type crack. To evaluate the force needed to overcome the edge-contact by Griffith type failure, it is assumed that this force is linear proportional to force at failure.

$$\frac{F_{edge}}{ca} \propto \sigma_c \quad \frac{F_{edge}}{ca} \approx C_1 \sigma_c \quad (4.40)$$

Combining equation (4.39) and (4.40) leads to the following expression for the force needed to overcome the edge contact due to a Griffith like failure

$$F_{edgeG} = C_1 ca \sqrt{\frac{2\gamma_a E_c}{\pi d_{crack}}} \quad (4.41)$$

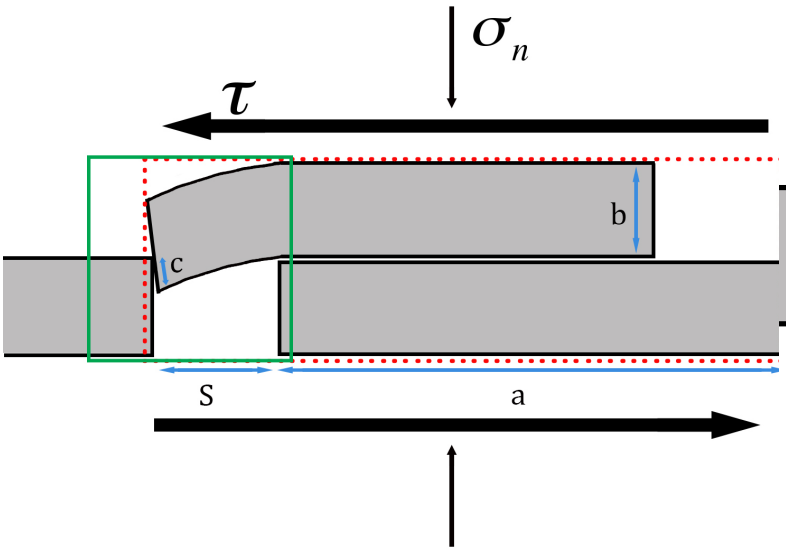

Figure 4.8a) Schematic overview of the unit cell of edge contact model

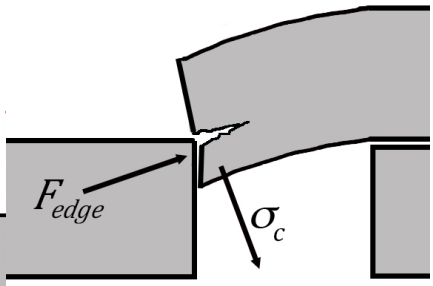

Figure 4.8.b) Detailed picture showing schematically the intial flaw and accompanied forces

4.3.4 Final microphysical model assembly and predicted frictional parameters

In sections 4.3.2 the vertical contact dimension c was expressed as function of the applied normal stress σ_n for the various proposed bending mechanisms, yielding three different expressions for the macroscopic shear strength as a function of σ_n (4.17; 4.24; 4.35). In addition, in section 4.3.3 three expressions for the failure strength of the contact were obtained, each derived assuming a different failure mechanism or scale thereof. These equations can be combined in different ways, leading to nine different relations between the macroscopic shear strength τ and normal stress σ_n, shown for cleavage failure and Griffith type failure in Table 4.1 and 4.2, respectively.

The relations between τ and σ_n presented in table 4.1 and 4.2 can be used to predict the (apparent) macroscopic friction coefficient μ. The microphysical models in which either elastic bending or time independent ductile bending is assumed (4.42- 4.45; 4.48; 4.49), give a linear relation between the normal stress and the shear stress in the form of $\tau = A\sigma_n$, i.e. they predict that the friction coefficient μ is then equal to A. For example, the microphysical model combining the maximum strength for cleavage failure with an elastic bending mechanism (4.43) predicts that $\mu = \frac{b}{a}\frac{2\gamma_s S}{E_a d_{lattice}(S+a)}$. The relation between τ and σ_n predicted for microphysical models in which the contact is the result of time dependent ductile bending is not linear with normal stress but exponential, rendering isolation of μ more difficult. However, an apparent coefficient of friction can be obtained by assuming that the relation between τ and σ_n at a certain range of normal stresses can be approximated as linear.

Apparent friction coefficients for the different models are calculated using the phyllosilicate mineral muscovite as an example. In calculating the friction coefficients, it is assumed that frictional slip along the horizontal phyllosilicate contact leads to negligible resistance compared to that due to failure of the edge contact. The values used for the different parameters are presented in appendix 2 and the predicted friction coefficients are presented in table 4.3 and 4.4 for cleavage failure and Griffith type failure, respectively. The friction coefficients for the different microphysical models assuming cleavage failure range from 1.25 x 10^{-7} to 1.25 x 10^{-3} (Table 4.3). The different microphysical models assuming Griffith type failure, in turn, predict friction coefficients ranging from 1.2 x 10^{-3} to 0.9 (Table 4.4).

The effect of (changes in) sliding velocity and/or temperature on μ for each microphysical model can be qualitatively estimated based on the relations between τ and σ_n shown in table 4.1 and 4.2. For example, if in the equation describing the shear strength the latter is not dependent on the temperature or on the sliding velocity, it follows logically that there is no effect of temperature or sliding velocity on μ. Only when either of the failure mechanisms is combined with ductile, time depended bending as contact mechanism it results in a dependence of μ on the velocity, i.e. velocity weakening (Tables 4.3 and 4.4).

Cleavage failure		
Contact mechanisms	Elastic	$\tau_{(C+e)\min} = A_1 + \left(\tilde{\mu} + A_2 \frac{b}{aE_a}\right)\sigma_n$ (4.42)
		$\tau_{(C+e)\max} = \left(\tilde{\mu} + A_2 \frac{b}{ad_{lattice}E_a}\right)\sigma_n$ (4.43)
	Ductile time independent	$\tau_{(C+d)\min} = A_1\left(1 + \frac{b\sigma_{yield}}{E_a}\right) + \left(\tilde{\mu} + A_2 \frac{b}{a\dot{h}}\right)\sigma_n$ (4.44)
		$\tau_{(C+d)\max} = A_1 \frac{b\sigma_{yield}}{d_{lattice}E_a} + \left(\tilde{\mu} + A_2 \frac{b}{d_{lattice}a\dot{h}}\right)\sigma_n$ (4.45)
	Ductile time dependent	$\tau_{(C+dt)\min} = A_1 + \tilde{\mu}\sigma_n + A_2\left(\frac{b}{a}\frac{\sigma_{yield}}{E_a} + \frac{1}{aE_a}SA\exp(\beta\sigma_n)\exp(-Q/RT)\left(\frac{S}{v_{slide}} + t_f\right)\right)$ (4.46)
		$\tau_{(C+dt)\max} = \tilde{\mu}\sigma_n + \frac{A_2}{d_{lattice}}\left(\frac{b}{a}\frac{\sigma_{yield}}{E_a} + \frac{1}{aE_a}SA\exp(\beta\sigma_n)\exp(-Q/RT)\left(\frac{S}{v_{slide}} + t_f\right)\right)$ (4.47)

Table 4.1 Relation between τ and σ_n for models combining cleavage failure and the different contact mechanisms. A_1 is $\frac{2\gamma_s S}{(S+a)a}$ and A_2 is $\frac{2\gamma_s S}{(S+a)}$

Griffith-type failure		
Contact mechanisms	Elastic	$\tau_{(G+e)} = \left(\tilde{\mu} + \frac{C_1}{E_a}\frac{b}{a}\sqrt{\frac{2E_c\gamma_s}{\pi c_{griffith}}}\right)\sigma_n$ (4.48)
	Ductile time independent	$\tau_{(G+d)} = \frac{b}{a}\frac{\sigma_{yield}}{E_a}C_1\sqrt{\frac{2E_c\gamma_s}{\pi d}} + \left(\tilde{\mu} + \frac{C_1}{\dot{h}}\frac{b}{a}\sqrt{\frac{E_{c\gamma_s}}{\pi c_{griffith}}}\right)\sigma_n$ (4.49)
	Ductile time dependent	$\tau_{(G+dt)} = \tilde{\mu}\sigma_n + C_1\sqrt{\frac{2E_c\gamma_s}{\pi c_{griffith}}}\left(\frac{b}{a}\frac{\sigma_{yield}}{E_a} + \frac{1}{a}SA\exp(\beta\sigma_n)\exp(-Q/RT)\left(\frac{S}{v_{slide}} + t_f\right)\right)$ (4.50)

Table 4.2 Relation between τ and σ_n for models combining Griffith type failure and the different contact mechanisms

Cleavage failure				
		(Apparent) Friction coefficient	Velocity dependence	Temperature dependence
Contact mechanisms	Elastic	$\mu_{(C+e)\min} = 2.5 \times 10^{-13}$ $\mu_{(C+e)\max} = 2.49 \times 10^{-4}$	No	No
	Ductile time dependent	$\mu_{(C+d)\min} = 1.88 \times 10^{-11}$ $\mu_{(C+d)\max} = 1.87 \times 10^{-2}$	No	With increasing temperature, μ increases
	Ductile time dependent	$\mu_{(C+dt)\min} = 1.88 \times 10^{-11}$ $\mu_{(C+dt)\max} = 1.87 \times 10^{-2}$	With increasing sliding velocity, μ decreases	With increasing temperature, μ increases

Table 4.3 The apparent friction coefficient, predicted response of μ on velocity and temperature for microphysical models combining cleavage failure and the different proposed contact mechanisms

Griffith-type failure						
		(Apparent) Friction coefficient			Velocity dependence	Temperature dependence
Contact mechanisms	Elastic	$c_{griffit}$ (in μm)	$C_1 = 1$	$C_1 = 10$	No	No
		0.1	$\mu_{(G+e)} = 3.8 \times 10^{-3}$	$\mu_{(G+e)} = 3.8 \times 10^{-3}$		
		0.5	$\mu_{(G+e)} = 1.7 \times 10^{-3}$	$\mu_{(G+e)} = 1.7 \times 10^{-2}$		
		1	$\mu_{(G+e)} = 1.2 \times 10^{-3}$	$\mu_{(G+e)} = 1.2 \times 10^{-2}$		
		1.5	$\mu_{(G+e)} = 9.9 \times 10^{-4}$	$\mu_{(G+e)} = 9.9 \times 10^{-2}$		
	Ductile time dependent	0.1	$\mu_{(G+d)} = 0.29$	$\mu_{(G+d)} = 2.9$	No	With increasing temperature, μ increases
		0.5	$\mu_{(G+d)} = 0.13$	$\mu_{(G+d)} = 1.3$		
		1	$\mu_{(G+d)} = 0.096$	$\mu_{(G+d)} = 0.96$		
		1.5	$\mu_{(G+d)} = 0.074$	$\mu_{(G+d)} = 0.74$		
	Ductile time dependent	0.1	$\mu_{(G+d)} = 0.29$	$\mu_{(G+d)} = 2.9$	With increasing sliding velocity, μ decreases	With increasing temperature, μ increases
		0.5	$\mu_{(G+d)} = 0.13$	$\mu_{(G+d)} = 1.3$		
		1	$\mu_{(G+d)} = 0.096$	$\mu_{(G+d)} = 0.96$		
		1.5	$\mu_{(G+d)} = 0.074$	$\mu_{(G+d)} = 0.74$		

Table 4.4 The apparent friction coefficient, predicted response of μ on velocity and temperature for microphysical models combining Griffith-type failure and the different proposed contact mechanisms

5 Microphysical models for wet phyllosilicate friction

Negligible differences are reported in the literature between the microstructures of wet and dry phyllosilicates sheared at low temperature (RT<T<400 ^{0}C) (cf. Chapter 2; e.g. Moore and Lockner, 2004). Frictional sliding of wet phyllosilicates is accordingly assumed to be potentially controlled by the same scales of interaction between the sliding grains as dry phyllosilicates (Chapter 4), i.e. interactions at the i) atomic-, ii) asperity- and/or iii) grain- scale. Microphysical models for the steady state frictional sliding of wet phyllosilicates are therefore developed by evaluating if, and if so, how, the models developed for dry phyllosilicate friction are affected by the presence of pore fluids.

Recall from Chapter 2 that from previous experimental studies a microphysical model for wet phyllosilicate friction needs to explain the following main observations:

i) A significant drop in frictional strength (μ_{wet} is~0.1-0.2 lower than μ_{dry}) of phyllosilicates in the presence of pore fluids compared to dry friction.
ii) Velocity strengthening behaviour of phyllosilicates at room temperature.
iii) An observed decrease in velocity strengthening with increasing temperature to (near) velocity-neutral or even slightly velocity weakening behaviour at the temperature range considered. (RT<T<400 ^{0}C).
iv) The qualitative relation found by Moore and Lockner, 2004 and Behnsen and Faulkner, 2012 that phyllosilicate minerals with hydrophobic plate surfaces have a lower drop in frictional strength between μ_{wet} and μ_{dry} than phyllosilicates with hydrophilic plate surfaces.

First, models in which wet phyllosilicate friction is controlled at the atomic scale are presented, followed by models for grain scale controlled friction. As explained in Chapter 4 models for asperity controlled friction are not derived in this study. An explanatory list of symbols introduced in these models is presented in Appendix 1.

5.1 Atomic barrier model in the presence of water

In this model, it is assumed that the presence of pore fluids only has a mechanical effect on friction and the possible chemical effects introduced by the presence of pore fluids are ignored. These latter effects are considered separately in section 5.2**.** This is done in order to separate the effects of these two types of processes on friction.

5.1.1 Model microstructure

A similar schematic microstructure and corresponding unit cell as used in section 4.2 is used for a wet phyllosilicate aggregate in which only atomic scale interactions offer shear resistance (Fig. 5.1a,b). In this model microstructure, movement of the phyllosilicate grains with respect to each other is assumed to occur atomic scale friction. The load supporting area, i.e. the horizontal area along which the grains are in contact with each other, is defined as a_r, while the area of the unit cell where the macroscopic normal stress is acting upon is called A.

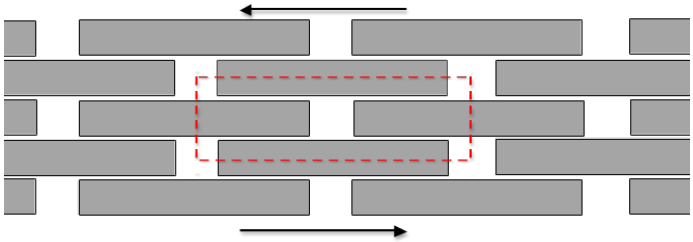

Figure 5.1a Schematic 2-dimensional representation of the microstructure of the wet atomic friction controlled microphysical model. The dotted red lines highlight the area of the unit cell.

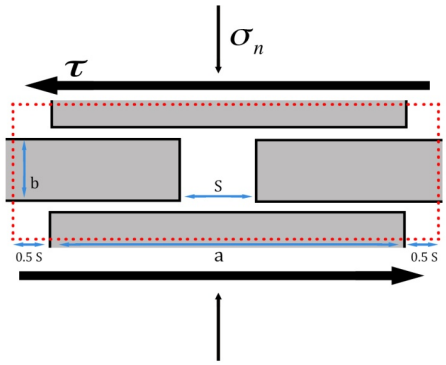

Figure 5.1b Unit cell of microphysical model for wet atomic controlled friction. In this figure *S* is the average horizontal distance between the phyllosilicate grains, *b* is the height of an individual grain and *a* is the width of a grain.

5.1.2 Force balance

It is assumed that fluids are only present in the pores and not along the grain contacts. When pore fluids are present, the macroscopic normal force $\sigma_n A$ acting on the unit cell is balanced by the microscopic normal force $\tilde{\sigma}_n A$ acting on the grain contacts plus the force supported by the pore fluid $P_f(A - a_r)$, i.e.

$$\sigma_n A = \tilde{\sigma}_n a_r + P_f(A - a_r) \qquad (5.1)$$

The force balance between the macroscopic and microscopic shear forces is the same as in the dry case, since fluids can not support shear forces, so:

$$\tau A = \tilde{\tau} a_r \qquad (5.2)$$

Rewriting equation 5.1 and using the same assumption as in the dry model, namely that for atomic scale interactions the relation between $\tilde{\tau}$ and $\tilde{\sigma}_n$ is frictional (4.10) yield the following relation between τ and $\tilde{\sigma}_n$:

$$\tilde{\tau} = \frac{A}{a_r}\tau$$

$$\tilde{\tau} = \tilde{\mu}\tilde{\sigma}_n (4.10) \rightarrow \tilde{\sigma}_n = \frac{A}{a_r}\tau \qquad (5.3)$$

Rewriting equation 5.1 and subsequently combining the resulting equation 5.3 yields the following expression for macroscopic shear stress τ:

$$\tilde{\sigma}_n = \frac{\sigma_n A - P_f(A - a_r)}{a_r}$$

$$\frac{A}{\tilde{\mu} a_r}\tau = \frac{(\sigma_n - P_f)A + P_f a_r}{a_r} \quad \rightarrow \quad \tau = \tilde{\mu}\left(\sigma_n - P_f + \frac{P_f a_r}{A}\right) \qquad (5.4)$$

When a pore fluid is present in the phyllosilicate aggregate, the contact area between the grains decreases as a result of fluid infiltration into the (grain) contacting areas (e.g. Paterson and Wang, 2002). If, as a result, the contact area of the grains a_r becomes much smaller than the total unit cell area A equation 5.4 simplifies to:

$$a_r << A \quad \frac{a_r}{A} \approx 0 \rightarrow \frac{P_f a_r}{A} \approx 0$$

$$\tau_{a-wet} = \tilde{\mu}(\sigma_n - P_f) = \tilde{\mu}(\sigma_{n\,eff}) \qquad (5.5)$$

5.1.3 Predicted macroscopic frictional parameters

The microphysical model for friction controlled by wet atomic scale interactions with only a mechanical effect due to presence of pore fluids predicts that the macroscopic frictional behaviour of wet phyllosilicates is controlled by the microscopic friction coefficient $\tilde{\mu}$. This result is equivalent to that obtained for the dry atomic scale controlled friction, with the exception that in this case a relation between τ and $\sigma_{n\,eff}$ is obtained instead of τ and σ_n. As mentioned in section 4.2.3, the literature on atomic scale friction of phyllosilicates is scarce. Liu et al. (1998) found an atomic coefficient of friction of 0.045 for muscovite using nanoscale Atomic Force Microscopy (AFM). Bucholz et al. (2012) studied atomic scale friction of pyrophyllite using AFM and obtained an atomic scale friction coefficient of ~ 0.03. Israelachvili and Kott (1990) reported friction coefficients of 0.01-0.03 for the sliding of atomically flat mica sheets with a confined layer of water between them. Thus, this model predicts very low values of the coefficient of friction.

5.2 Thin adsorbed water film model

Moore and Lockner (2004) proposed that frictional sliding in wet phyllosilicates is accommodated by viscous slip on a thin water film bonded to the 001 mineral plane. According to Moore and Lockner (2004), the water molecules are bonded to the 001 mineral plane of phyllosilicates in proportion to their surface energy. The difference in frictional strength between different water-saturated phyllosilicates is accordingly explained as resulting from the difference in bonding strength of this thin film of water to the phyllosilicate surface.

To evaluate the hypothesis of Moore and Lockner (2004) in a physically robust way, a microphysical model is developed here, where the mechanism controlling frictional sliding is viscous slip on a thin water film confined between phyllosilicate grains.

5.2.1 Model microstructure and deformation mechanisms

The same microstructural model as used in the atomic interaction controlled friction model is used here, but now a thin adsorbed film of liquid separates the grains. A schematic representation of the proposed microstructural model is shown in Figure 5.2a and the corresponding unit cell in Figure 5.2b. The movement of the grains past each other in this model microstructure is accommodated by viscous slip in the thin adsorbed liquid film.

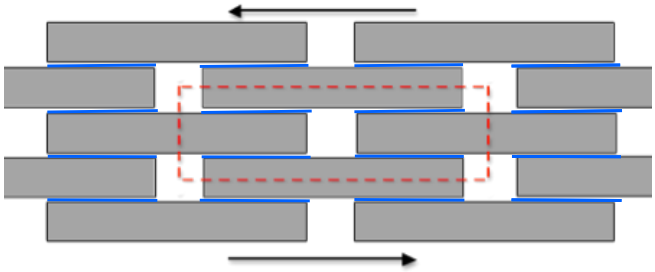

Figure 5.2a A schematic representation of the microstructure for thin adsorbed film model. The blue lines represents (very schematically) the confined adsorbed layer. The dotted red lines highlight the unit cell

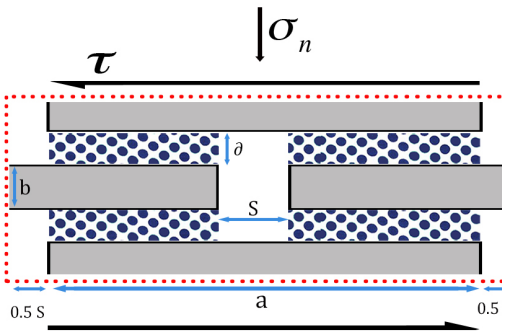

Figure 5.2b Schematic representation of the unit cell of thin adsorbed film model. The parameters *a*, *b* and represent the horizontal width of a grain, the thickness of the grain and the average distance between the grains respectively. The thickness of the confined layer of water is given by δ. The thickness of the confined water film compared to the grains is exaggerated in this figure.

5.2.2 Force balance

The microscopic normal stress $\tilde{\sigma}_n$, supported by a thin film of fluid confined between two solids, is equal to the pore fluid pressure of the bulk fluid phase P_f plus an additional term called disjoining pressure Π_d (Butt et al, 2003). The disjoining pressure is caused by an interplay of surface interactions, however for confined liquids it is more appropriate to think of the disjoining pressure as an increased pressure supported by the liquid film, instead of as resulting from surface forces.

$$\tilde{\sigma}_n = \Pi_d + P_f \tag{5.6}$$

The microscopic shear stress needed to slide two grain past each other by viscous slip in a confined Newtonian fluid, such as water, depends on the shear strain rate $\dot{\gamma}$ and the viscosity of the fluid η:

$$\tilde{\tau} = \eta\dot{\gamma} \tag{5.7}$$

The general force balance between the microscopic and macroscopic, shear and normal stresses is in this model equivalent to section 5.1 and shear stresses, i.e. equations 5.1 and 5.2. Rewriting those equations and using 5.5 and 5.6 results in the following expression for the shear strength:

$$\frac{\sigma_n A}{\tau A} = \frac{\tilde{\sigma}_n a_r + P_f (A - a_r)}{\tilde{\tau} a_r}$$

$$\tau = \frac{\tilde{\tau} a_r}{\tilde{\sigma}_n a_r + P_f (A - a_r)} \qquad (5.8)$$

The expression for the shear strength τ can be simplified if it assumed that the average distance between the grains S is negligible compare to the area that is covered by an adsorbed film, a_r, the macroscopic area of the unit cell, A, is roughly equal to the grain contacting area.

$$S << a \qquad A = (a + S)a \approx a^2 \rightarrow a_r = (a - S)a \approx a^2 \rightarrow A - a_r \approx 0$$

Since the area where upon the macroscopic shear stress is acting is the same area as where upon the microscopic shear stress is acting the macroscopic and microscopic shear stresses are equal:

$$\tau a^2 = \tilde{\tau} a^2 \rightarrow \tau = \tilde{\tau} \qquad (5.9)$$

Combining then equation 5.7 and 5.9 yields the following expression for the macroscopic shear strength:

$$\tau = \eta \dot{\gamma} \qquad (5.10)$$

The shear strain rate $\dot{\gamma}$ in this geometry is given by the sliding velocity of the grains past each other, v_{slide}, over the thickness of the film, δ. Using this expression for $\dot{\gamma}$ and equation 5.10 yields:

$$\dot{\gamma} = \frac{v_{slide}}{\delta}$$
$$\tau = \eta \frac{v_{slide}}{\delta} \qquad (5.11)$$

The thickness δ of a confined thin water film decreases with increasing (macroscopic) effective normal stress $\sigma_{n\,eff}$ acting on the water layer (Rutter, 1983; Isrealachvilli et al., 1988; Renard and Ortoleva, 1997). The macroscopic effective normal stress is in equilibrium with the microscopic normal stress by the thin film, meaning that the effective normal stress is equal to the disjoining pressure Π_d, i.e.:

$$\sigma_n - P_f = \sigma_{n\,eff} = \Pi_d \qquad (5.12)$$

The relation between the thickness of the water film δ and the disjoining pressure Π_d is found to be either an exponential function in the form $\delta = a\exp(b\Pi_d)$ or a power-law function of the form $\delta = a\Pi_d{}^n$ (e.g. Pashley and Israelachvili, 1984; Beaglehole and Christenson, 1992; Heidug, 1995; Renard et Ortoleva, 1997), where *a*, *b* and *n* are experimentally derived constants. Beaglehole and Christenson, 1992 measured the disjoining pressure of thin water films on mica sheets (Fig. 5.3).

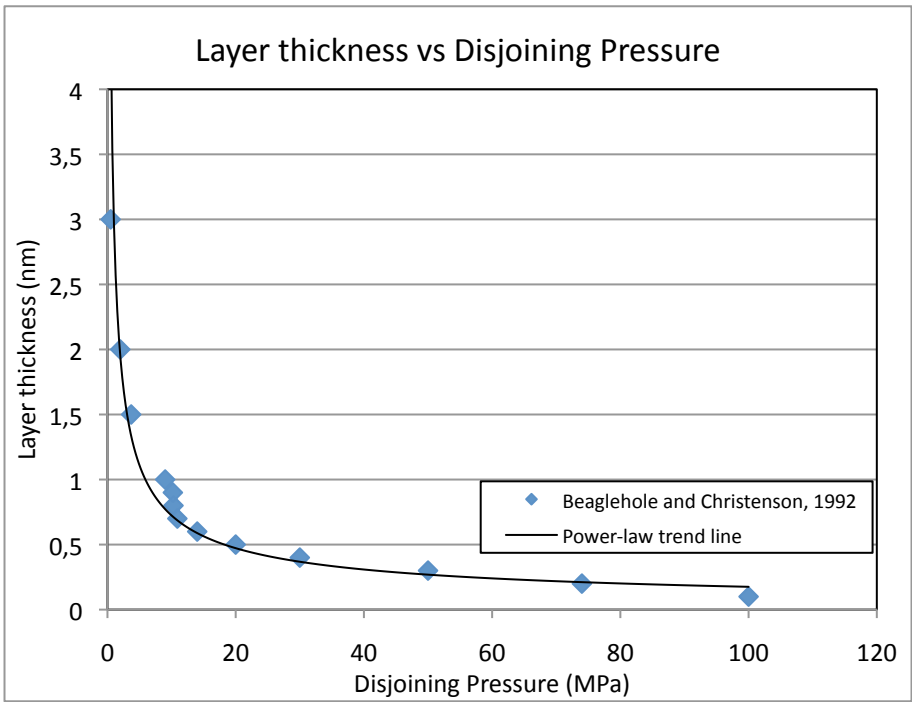

Figure 5.3 Thickness δ of thin water film on mica plotted versus the disjoining pressure Π_d, after data of Beaglehole and Christenson, 1992. The trend line is obtained assuming a power law relation between δ and Π_d.The trend line has a least square fit of R^2=0.93%

A power law function of the form $\delta = a\Pi_d^n$ was found to fit the data best with a being 1.472x10^{-5} mN^{-1} and a n-value of 6.145x10^{-1}. Inserting this power-law function for δ into equation 5.12 yields the following expression of the macroscopic shear strength τ:

$$\tau_v = \eta \frac{v_{slide}}{1.472 \times 10^{-5} \sigma_{neff}^{-0.614}} \qquad (5.13)$$

5.2.3 Material properties of confined liquid films

Equation (5.7) used to describe the viscous slip in the model, assumes macroscopic continuum behaviour of the fluid. The properties of a thin adsorbed liquid film, however, are not necessarily similar to its bulk continuum fluid properties. It is therefore necessary to review if, and if so how, the properties of thin films of liquids, and water in particular, are different from their bulk properties.

It is commonly assumed that adsorbed liquids consisting of only a few molecular layers are structured, which should lead to an increased viscosity of the adsorbed liquid film**.** However, conflicting results are obtained for the properties of confined liquids by different groups of authors using different kinds of experimental techniques. Israelachvili and colleagues (e.g. Israelachvili and Adams, 1978; Pashley and Israelachvili, 1984; Israelachvili, 1986; Israelachvili and Kott, 1988; Israelachvili et al., 1990) were the first to study the properties of liquids in confinement using the so-called surface force apparatus (SFA). In this apparatus a liquid is compressed between two cylindrical mica sheets. The distance between the sheets is measured by interferometry and the resistive force opposing the approach of the sheets towards each other and/or the sliding of one sheet relative to the other is measured by an arrangement of springs (e.g. Pashley and Israelachvili, 1984; Israelachvili, 1986)

In studies using the SFA on a variety of liquids, it is commonly seen that eventually the viscous friction behaviour of the liquids breaks down when 1-6 molecular layers of adsorbed liquid on the surface are present (e.g. Israelachvili and Kott, 1988; Klein et al., 2001). This is thought to arise from the transition from a fluid-like behaviour to solid or glass-like behaviour. For example, it is commonly seen that a finite shear stress is needed to initiate sliding for such thin liquids films (Israelachvili et al., 1990).

In SFA studies on pure water and/or aqueous solutions however this behaviour is not evident. For example, Israelachvili (1986) found that a thin film of water confined between two mica surfaces has bulk liquid properties even when only one molecular layer of water was present at the mica surface. Israelachvili also concluded that the position of the plane of slip is, within one molecular layer of the interface, consistent with the no slip boundary condition for viscous flow. His conclusions were not affected when instead of water a high concentration NaCl solution was used, introducing high repulsive hydrations surface forces. As a result, the water molecules should be more tightly bonded to the surface and this reaction should lead to an enhanced viscosity of the confined film (as is the case for other liquids studied), but evidently this was not the case for water. Other authors, using similar methods (e.g. Israelachvili and Kott, 1998; Klein et al., 2001), reproduced these results. All found the viscosity of confined thin water layers to be maximally 2-3 orders of magnitude higher than the bulk viscosity of water. Measurements of diffusion coefficients in confined films of water by Alcantar et al., 2003, were found to be around 2-3 orders of magnitude higher than bulk coefficients, further strengthening that the properties of confined films are broadly similar to those of their bulk properties.

It should be noted that the values obtained by Israelachvili and other authors using the SFA are however not in agreement with groups of authors using the Interfacial Force Microscope (IFM). In IFM, the frictional force of liquids between a probe tip and a flat sample is studied. IFM studies of water confined to 1-2 nm between the IFM-tip and a flat sample typically give results for the viscosity in the order of 10^6 to 10^7 times the bulk viscosity of water (e.g. Major et al., 2006; Goertz et al., 2007). At the moment there is no explanation for this discrepancy.

The viscosity measurements done by Israelachvili and colleagues are conducted in experimental settings considerably more similar to the settings in which friction experiments on phyllosilicates are conducted than that of the IFM, i.e. liquids confined between two phyllosilicate minerals instead of a probe tip and a sample. The viscosity measurements conducted by the SFA are therefore used as an estimate for the viscosity of a thin adsorbed water film on a phyllosilicate grain.

5.2.4 Predicted macroscopic frictional parameters

Using equation (5.13), the shear strength τ needed for viscous slip on a confined water film versus the effective normal stress is calculated (Fig. 5.4 and 5.5). A value for η hundred times the bulk viscosity of water at room temperature (100 Pa s) was used in these calculations, based on the results of Israelachvili and colleagues and sliding velocities of 10^{-5} µm/s (Fig. 5.4) and 1 µm/s (Fig. 5.5), respectively. As can be observed in Figures 5.4 and 5.5, the relation between τ and $\sigma_{n\,eff}$ is not linear, so only an apparent coefficient of friction can be calculated. In both figures, the relation between τ and $\sigma_{n\,eff}$ is linearly approximated for effective stress ranges of 1-20 MPa, 20-40 MPa and 40-100 MPa. The apparent coefficient of friction obtained by assuming a linear relation in these stress ranges is shown in table 5.1. Table 5.2 and equation 5.13 clearly show that increasing the sliding velocity with an order of magnitude results in an increase of frictional strength by the same order of magnitude, meaning that velocity strengthening behaviour is predicted by this model.

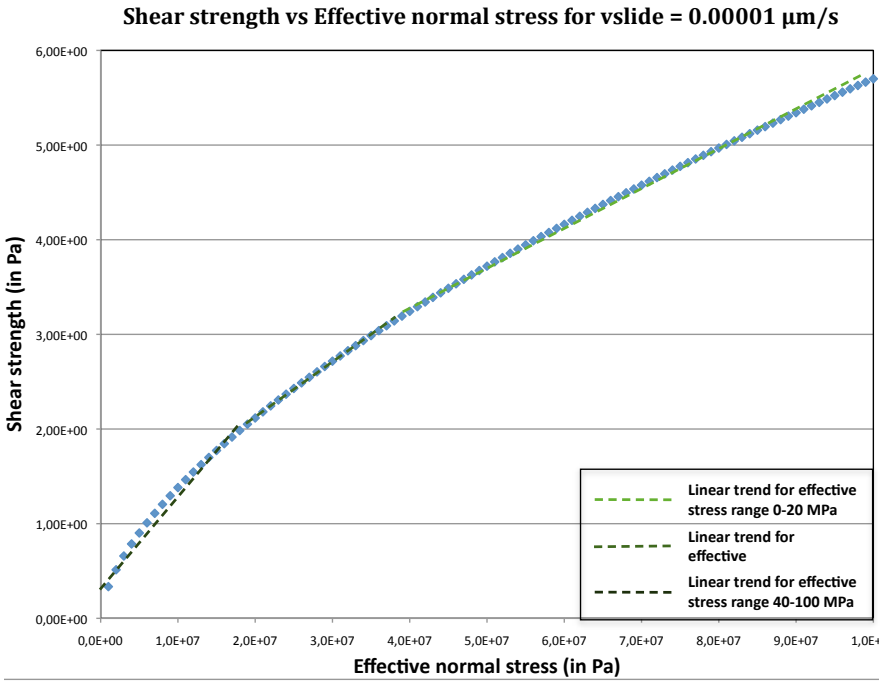

Figure 5.4 The relation between τ and σ_{neff} for viscous slip controlled friction with η is 100 Pas and v_{slide} is 10^{-5} µm/s. The dotted are trend lines assuming a linear relation between τ and σ_{neff}, for σ_{neff} range of 0 – 20 MPa, 20-40 MPa and 40 – 100 MPa respectively.

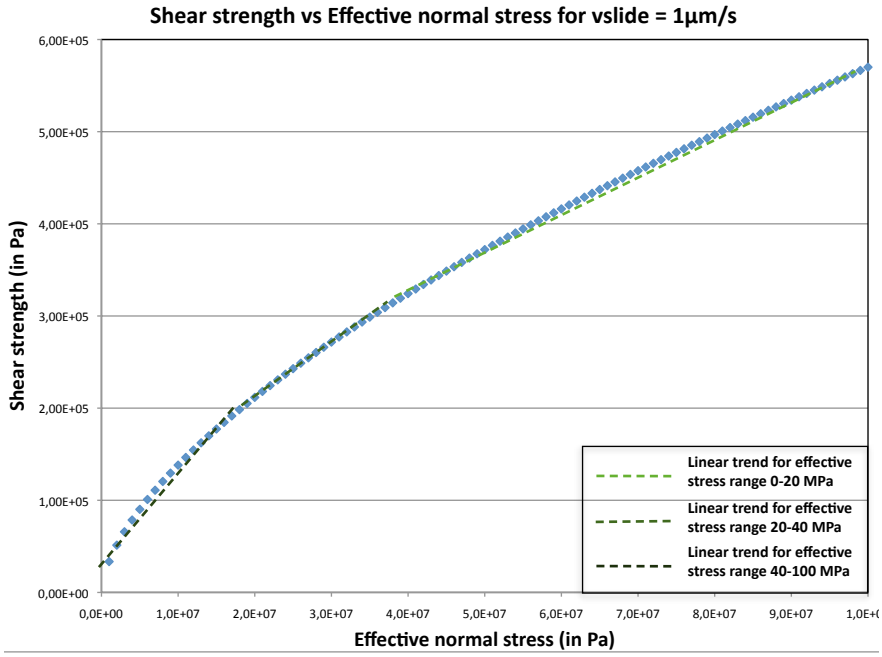

Figure 5.5 The relation between τ and σ_{neff} for viscous slip controlled friction with η is 100 Pas and v_{slide} is 1 µm/s. The dotted lines are trend lines assuming a linear relation between τ and σ_{neff}, for σ_{neff} range of 0 – 20 MPa, 20-40 MPa and 40–100 MPa respectively.

	$v_{slide} = 10^{-5}\mu/s$	$v_{slide} = 1\mu/s$
σ_{neff} range of 1 – 20 Mpa	$\mu = 9.38 \times 10^{-8}$	$\mu = 9.38 \times 10^{-3}$
σ_{neff} range of 20 – 40 Mpa	$\mu = 5.63 \times 10^{-8}$	$\mu = 5.63 \times 10^{-8}$
σ_{neff} range of 40 – 100 Mpa	$\mu = 4.09 \times 10^{-8}$	$\mu = 4.09 \times 10^{-3}$

Table 5.1 Apparent coefficient of friction for viscous slip controlled friction for different sliding velocities and different σ_{neff} ranges.

5.3 Grain scale barrier model in presence of water

In section 4.3, microphysical models were derived in which friction of dry phyllosilicates is controlled by the edge-contacts between the sliding grains. In the current section, it is evaluated if, and if so how, these models change when pore fluids are present. Furthermore an additional mechanism of overcoming edge-contacts is discussed in section 5.3, i.e. failure by subcritical crack growth.

5.3.1. Model microstructures and deformation mechanisms

A similar microstructural model and corresponding unit cell as used in section 4.3 is used here (Fig. 5.6), with the difference that now pore fluids are present. The strain in this model is accommodated by the serial processes of either atomic scale controlled friction or viscous slip on a thin adsorbed film along the horizontal contact and internal deformation of the (top) grain to overcome the edge contact.

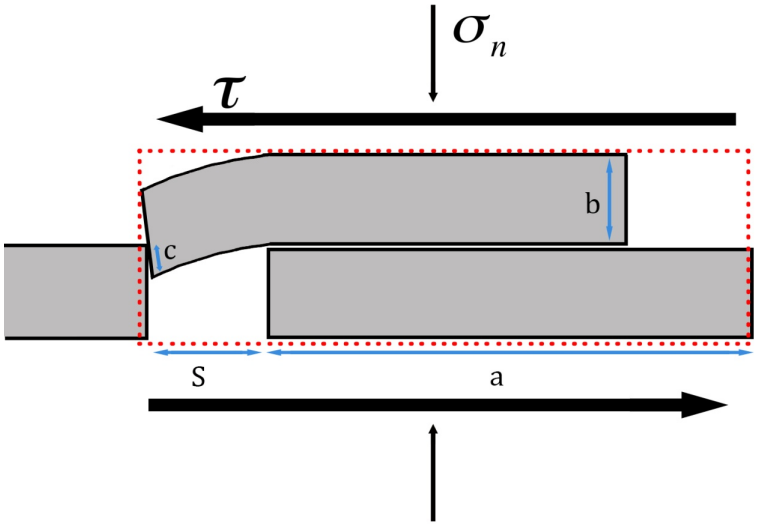

Figure 5.6 Schematic representation of the unit cell used for the wet edge contact model. S here represents the average distance between the grains, a and b represent the length and height of the phyllosilicate grain respectively. c is the vertical length of contact between the grains. Lastly, τ and σ_n are the macroscopic shear and normal stress respectively.

5.3.2. Force balance

The general expression (4.9) obtained for the macroscopic shear strength τ for the dry edge contact models is modified hereunder for the case when pore fluids are present. When it is assumed that sliding along the horizontal contact area is controlled by 'wet' atomic scale friction behaviour (cf. section 5.1) equation 4.9 is modified to include a pore fluid pressure term, yielding:

$$\tau = \tilde{\mu}\sigma_{n\,eff} + \frac{\tau_{edge} c}{a} \tag{5.14}$$

If it is assumed that sliding along the horizontal contact area is controlled by viscous slip on a thin confined film (cf. section 5.2) equation 4.9 is modified to include a pore fluid pressure term, yielding:

$$\tau = \eta \frac{v_{slide}}{1.472... \times 10^{-5} \sigma_{n\,eff}^{-0.6145...}} + \frac{\tau_{edge} c}{a} \tag{5.15}$$

The force to overcome the edge by different failure mechanisms and the different proposed mechanisms by which the vertical contact length c can be established are evaluated in section 4.3. In the following section it is evaluated if these bending and failure mechanisms are affected by the presence of pore fluids.

5.3.2.1 *Effect of pore fluids on bending mechanisms*

Recall from section 4.3 that contact between adjacent grains can be introduced by bending of the upper grain into the pore area by: i) elastic, ii) ductile time independent and iii) ductile time dependent bending deformation. The elastic behaviour of (rock) materials is not affected by the presence of pore fluids (Paterson and Wong, 1998). There is also no evidence that ductile time independent processes such as work hardening deformation are affected by pore fluids. The effect of pore fluids, especially water, on dislocation creep deformation has been studied by various authors on i.e. quartzite (Post et al., 1996), quartz (Ayensu and Ashbee, 1977) and olivine (Faul et al., 2011). It is found that the presence of water increases the rate of dislocation creep. Since time dependent ductile deformation of phyllosilicates is not well studied, it is not possible to incorporate this effect into the model calculations.

5.3.2.2 *Effect of pore fluids on failure mechanisms*

Recall from section 4.3 that two possible failure mechanisms of the edge contact are evaluated; i) failure of the edge contact by cleavage and ii) Griffith-like failure of the edge contact. The presence of pore fluids has no effect on the mechanism of cleavage failure. It can, however, drastically change the surface energy of materials (Butt et al., 2003; Israelachvili, 2011). The surface energy of muscovite is for example in complete vacuum ~ 5 Jm^{-2} (Obriemoff, 1930), but drops in humid environments to 0.3 Jm^{-2} (Bailey et al., 1969). Note that the value for surface energy in vacuum is not used in the dry models, since experiments on phyllosilicates friction are not conducted at that level of vacuum. It is therefore assumed that the presence of pore fluids has no effect on the cleavage failure mechanism.

The presence of water has in principle also no effect on Griffith-type failure mechanisms, but it is well established that when pore fluids are present, failure commonly occurs at stresses (much) lower than predicted for Griffith failure (e.g. Atkinson, 1979; Scholz, 2002). This phenomenon is called subcritical crack growth and is assumed to occur instead of Griffith failure when pore fluids are present. Griffith-type failure is therefore assumed to be the maximum failure strength in the case pore fluids present. The process of overcoming edge contacts by subcritical crack growth failure is evaluated in the next section.

5.3.3. Subcritical crack growth failure

Subcritical crack growth is the general term for the phenomenon where pre-existing cracks in a material propagate at stress intensity factors significantly lower than the critical value for dynamic failure, meaning that cracks propagate at substantially lower (remote) stresses than the critical stress predicted a Griffith-type failure. A number of mechanisms have been suggested to explain this phenomenon: e.g. stress corrosion and atomic diffusion. Stress corrosion is thought to be the dominant process at low homologous temperatures. Crack growth by stress corrosion occurs by the weakening of strained bonds at the crack tip by a stress dependent chemical reaction, which is influenced by the pore fluid (chemistry) in the crack environment (Atkinson, 1979; Freiman, 1984; Scholz, 2002).

The relation between the crack growth velocity v_c and the applied stress or stress intensity factor is usually described in a power law of the form:

$$v_c = A(T)K_1^n \tag{5.16}$$

where $A(T)$ is an experimentally derived temperature dependent term and n is called the stress-corrosion index (Atkinson, 1979; Scholz, 2002). For stress corrosion dominated subcritical crack growth, the following general expression between the crack propagation velocity and the stress intensity factor has been derived from theoretical considerations and experimental work (Bolz and Weiderhorn, 1970; Atkinson, 1979; Scholz, 2002):

$$v_c = v_0 \exp\left(\frac{-H + BK_1}{RT}\right) \tag{5.17}$$

where v_0' and B are experimentally fitted constants, H is the activation enthalpy related to the process by which subcritical crack growth occurs, R is the gas constant, T the absolute temperature and K_I is the stress intensity factor for the opening of a mode 1 crack. In this study, this crack growth law is used because of its theoretical basis.

The approach used to obtain an expression relating the failure strength of a grain contact by subcritical crack growth failure and the macroscopic sliding velocity is to integrate the time it takes for a subcritically growing crack with initial length c_0 to grow to a failure length c_f at which the crack fails dynamically. This is described in Appendix 3 and yields the following expression for the sliding velocity:

$$v_{slide} = \frac{d_{unitcell}}{\frac{(2\frac{-b\sigma_r\sqrt{\pi}}{RT}\sqrt{c_f}-1)\exp(\frac{H}{RT}-\frac{-b\sigma_r\sqrt{\pi}}{RT}\sqrt{c_f})}{v_0(\frac{-b\sigma_r\sqrt{\pi}}{RT})^2} - \frac{(2\frac{-b\sigma_r\sqrt{\pi}}{RT}\sqrt{c_0}-1)\exp(\frac{H}{RT}-\frac{-b\sigma_r\sqrt{\pi}}{RT}\sqrt{c_0})}{v_0(\frac{-b\sigma_r\sqrt{\pi}}{RT})^2}}$$

This expression is complex, and a second, simpler approach is used here to obtain a first order estimate of the relation between the failure strength of edge contacts by subcritical crack growth and the sliding velocity. It is assumed that the remote stress acting on the crack σ_r can be regarded as a constant during crack growth and that with fixed stress, cracks, with initial crack length c_0 will start to grow until they have a crack length of failure c_f and fail dynamically. Instead of relating the sliding velocity v_{slide} with the time it takes for an edge contact to fail, it is assumed for simplicity that the mean crack growth velocity is approximately equal to macroscopic sliding velocity, so $v_{crackmean} \approx v_{slide}$.

At the mean crack velocity, $v_{crackmean}$, the growing crack has a length of c_{mean}. Using the expression for the stress intensity factor K_1 and rearranging the terms of equation 5.17, an expression relating remote stress acting on the crack with the sliding velocity is obtained:

$$K_1 = B\sigma_r\sqrt{\pi c_{mean}}$$

$$\frac{v_{slide}}{v_0} = \exp\left(\frac{-H + B\sigma_r\sqrt{\pi c_{mean}}}{RT}\right)$$

$$\ln\left(\frac{v_{slide}}{v_0}\right) = \frac{-H + B\sigma_r\sqrt{\pi c_{mean}}}{RT}$$

$$\sigma_r = \frac{\ln\left(\frac{v_{slide}}{v_0}\right)RT + H}{B\sqrt{\pi c_{mean}}} \qquad (5.18)$$

Assuming then, as is done in section 4.3.3.2 for Griffith type failure, that the remote applied stress σ_r is linearly related to F_{edge} the following expression for F_{edge} is obtained:

$$C_1\sigma_r = \frac{F_{edge\ scc}}{ca}$$

$$F_{edge\ scc_r} = C_1 ca\frac{\ln(v_{slide}/v_0)RT + H}{B\sqrt{\pi c_{mean}}} \qquad (5.19)$$

5.3.4 Final model assembly and predicted frictional parameters

In sections 5.2 and 5.3 expressions were derived for either wet atomically controlled friction (5.14) or viscous slip on a thin adsorbed film (5.15) on the horizontal contact area. Combining these expressions with the expression obtained for cleavage failure (4.37-4.39) or subcritical crack growth failure (5.19) of the edge contact yields different expressions relating τ with σ_{neff} and are presented below.

Cleavage failure models assuming wet atomically controlled friction at the horizontal contact area between the grains, predict an equivalent expression for macroscopic shear stress τ as in the dry cleavage failure models, but now with τ as a function of the effective normal stress σ_{neff}(cf. Table 4.3). These wet cleavage failure models predict therefore the same frictional parameters as the models for the dry case (cf. Table 4.4). The relation between τ and σ_{neff} for wet cleavage failure models assuming viscous slip on a thin adsorbed film at the horizontal contact area is presented in table 5.3 and the respective predicted frictional parameters of these models in Table 5.4.

The microphysical models assuming cleavage failure and viscous slip on a thin adsorbed film predict apparent friction coefficients ranging from 6.72 x 10^{-8} to 2.54 x 10^{-2}. All models predict a dependence of μ on (changes in) the sliding velocity since viscous slip (on a thin adsorbed film) depends strongly on the sliding velocity. Therefore all models, except the model combining ductile time dependent bending and cleavage failure of the edge contact, predict that μ increases linearly with increasing sliding velocity. The model combining ductile time dependent bending predicts a competition between velocity weakening due to ductile time dependent bending and velocity strengthening due to viscous slip.

The relation between τ and σ_{neff} for microphysical models assuming sub critical crack growth failure of the edge contact and viscous slip on a thin adsorbed film at the horizontal contact area are presented in table 5.5.

No literature exists on subcritical crack growth processes in phyllosilicates and therefore the relevant parameters needed in calculating the frictional parameters that the subcritical crack growth failure models would predict are unknown. Thus, the predicted frictional parameters of subcritical failure models can only be described qualitatively. The predicted frictional strength of subcritical crack growth failure models is lower than that of Griffith-type failure, since cracks of a fixed length start to grow by subcritical processes at stress intensity factors and by consequence remote stresses lower than predicted from (dynamic) Griffith-type failure. Furthermore, subcritical crack failure models predict that μ increases with the natural logarithmic of the macroscopic sliding velocity as is clear from equation 5.19 and table 5.5. Therefore, all models, except the model combining ductile time dependent bending and failure of the edge contact, predict velocity-strengthening behaviour. The model combining ductile time dependent bending predicts a competition between velocity weakening by the ductile time dependent bending process and velocity strengthening due to viscous slip.

Cleavage failure + viscous slip		
Contact mechanisms	Elastic	$\tau_{c\min} = \eta \frac{v_{slide}}{1.472... \times 10^{-5} \sigma_{neff}^{-0.6145...}} + A_1 + \left(A_2 \frac{b}{aE_a} \right) \sigma_{neff}$ (5.20)
		$\tau_{c\max} = \eta \frac{v_{slide}}{1.472... \times 10^{-5} \sigma_{neff}^{-0.6145...}} + \left(A_2 \frac{b}{ad_{lattice}E_a} \right) \sigma_{neff}$ (5.21)
	Ductile time independent	$\tau_{c\min} = \eta \frac{v_{slide}}{1.472... \times 10^{-5} \sigma_{neff}^{-0.6145...}} + A_1 \left(1 + \frac{b}{a} \frac{\sigma_{yield}}{E_a} \right) + \left(A_2 \frac{b}{a\dot{h}} \right) \sigma_{neff}$ (5.22)
		$\tau_{c\max} = \eta \frac{v_{slide}}{1.472... \times 10^{-5} \sigma_{neff}^{-0.6145...}} + A_1 \frac{b}{a} \frac{\sigma_{yield}}{E_a} + \left(A_2 \frac{b}{ad_{lattice}\dot{h}} \right) \sigma_{neff}$ (5.23)
	Ductile time dependent	$\tau_{c\min} = \eta \frac{v_{slide}}{1.472... \times 10^{-5} \sigma_{neff}^{-0.6145...}} + A_1 \left(1 + \frac{b}{a} \frac{\sigma_{yield}}{E_a} + SA \exp(B\sigma_{neff}) \exp(-Q/RT) \left(\frac{S}{v_{slide}} + t_f \right) \right)$ (5.24)
		$\tau_{c\min} = \eta \frac{v_{slide}}{1.472... \times 10^{-5} \sigma_{neff}^{-0.6145...}} + A_1 + \frac{A_1}{d_{lattice}} \left(1 + \frac{b}{a} \frac{\sigma_{yield}}{E_a} + SA \exp(B\sigma_{neff}) \exp(-Q/RT) \left(\frac{S}{v_{slide}} + t_f \right) \right)$ (5.25)

Table 5.2 Relation between τ and σ_{neff} for cleavage failure and viscous slip microphysical models for different contact mechanisms. A_1 is $\frac{2\gamma_s S}{(S+a)a}$ and A_2 is $\frac{2\gamma_s S}{(S+a)}$

Cleavage failure + viscous slip					
		(Apparent) Friction coefficient		Velocity dependence	Temperature dependence
Contact mechanisms	Elastic	$v_{slide} = 10^{-6} \mu m/s$	$v_{slide} = 1 \mu m/s$	μ increases linearly with increasing sliding velocity	No
		$\mu_{(C+e)\min} = 6.74 \times 10^{-8}$	$\mu_{(C+e)\min} = 6.74 \times 10^{-3}$		
		$\mu_{(C+e)\max} = 2.49 \times 10^{-4}$	$\mu_{(C+e)\max} = 6.99 \times 10^{-3}$		
	Ductile time dependent	$\mu_{(C+d)\min} = 6.74 \times 10^{-8}$	$\mu_{(C+d)\min} = 6.74 \times 10^{-3}$	μ increases linearly with increasing sliding velocity	μ increases with increasing T
		$\mu_{(C+d)\max} = 1.86 \times 10^{-2}$	$\mu_{(C+d)\max} = 2.54 \times 10^{-2}$		
	Ductile time dependent	$\mu_{(C+d)\min} = 6.74 \times 10^{-8}$	$\mu_{(C+d)\min} = 6.74 \times 10^{-3}$	Combination of linear increase with sliding velocity of μ due viscous slip and decrease of μ with increasing sliding velocity at edge contact failure	μ increases with increasing T
		$\mu_{(C+d)\max} = 1.86 \times 10^{-2}$	$\mu_{(C+d)\max} = 2.54 \times 10^{-2}$		

Table 5.3 The apparent friction coefficient, predicted response of μ on velocity and temperature for microphysical models combining cleavage failure and the different proposed contact mechanisms

Subcritical crack growth failure + viscous slip		
Contact mechanisms	Elastic	$\tau_{(scc+e)} = \eta \frac{v_{slide}}{1.472... \times 10^{-5} \sigma_{neff}^{-0.6145...}} + \left(\frac{C_1}{E_a} \frac{b}{a} \left(\frac{\ln(v_{slide}/v_o)RT + H}{B\sqrt{\pi d_{mean}}} \right) \right) \sigma_{neff}$ (5.26)
	Ductile time independent	$\tau_{(scc+d)} = \eta \frac{v_{slide}}{1.472... \times 10^{-5} \sigma_{neff}^{-0.6145...}} + C_1 \frac{\sigma_{yield}}{E_a} \frac{b}{a} \left(\frac{\ln(v_{slide}/v_o)RT + H}{B\sqrt{\pi d_{mean}}} \right) + \left(\frac{C_1}{\dot{h}} \frac{b}{a} \left(\frac{\ln(v_{slide}/v_o)RT + H}{B\sqrt{\pi d_{mean}}} \right) \right) \sigma_{neff}$ (5.27)
	Ductile time dependent	$\tau_{(scc+dt)} = \eta \frac{v_{slide}}{1.472... \times 10^{-5} \sigma_{neff}^{-0.6145...}} + C_1 \left(\frac{\ln(v_{slide}/v_o)RT + H}{B\sqrt{\pi c_{mean}}} \right) \left(\frac{b}{a} \frac{\sigma_{yield}}{E_a} + SA \exp(\beta \sigma_{neff}) \exp(-Q/RT) \left(\frac{S}{v_{slide}} + t_f \right) \right)$ (5.28)

Table 5.4 Relation between τ and σ_{neff} for subcritical crack growth failure and viscous slip microphysical models for different contact mechanisms

6 Discussion

Based on the observations reported in the literature (cf. Chapter 2) and on experiments conducted in this study (cf. Chapter 3) it is concluded that frictional sliding of dry and wet phyllosilicates at low temperature (RT<T<400^{0}C) is controlled at one of the following interaction scales between the (sliding) grains: i) atomic, ii) asperity or iii) grain scale. In Chapters 4 and 5 microphysical models were developed for steady state frictional sliding of respectively dry and wet phyllosilicates at low temperature. In the derived models friction was either controlled by atomic or by grain scale interactions between the sliding grains. The predicted (apparent) frictional coefficients and predicted trends in the dependence on (changes in) sliding velocity of the friction predicted by the different developed microphysical models are compared with observations on phyllosilicate friction reported in the literature. This is done in order to evaluate if one of the models can explain the observations on pure phyllosilicate friction.

6.1 Dry models versus observations in literature

Recall from Chapter 2 that a microphysical model for dry phyllosilicate friction ideally should explain the following main observations on phyllosilicate friction:

i) The low frictional strength of dry phyllosilicates compared to other rock forming minerals, i.e. μ≈0.1-0.6 compared to μ ≈0.85 (e.g. Byerlee, 1978; Ikari et al., 2009,2011)

ii) The velocity strengthening behaviour of phyllosilicates observed at low temperature range (RT<T<400^{0}C) (e.g. Ikari et al., 2009, 2011; van Digellen et al, 2010; den Hartog et al., 2013)

iii) The (linear) relation found by Moore and Lockner, 2004 between the interlayer bond strength of phyllosilicate minerals and their frictional strength.

6.1.1 Atomic scale barrier model versus previous experiments

The microphysical model developed for atomic scale friction predicts that the macroscopic coefficient of friction, μ, is equal to the atomic coefficient of friction $\tilde{\mu}$. Values of the atomic friction coefficient of phyllosilicates reported in the literature are roughly one order of magnitude lower than the macroscopic coefficient of friction observed, i.e. $\tilde{\mu}$ is ~0.03 for pyrophyllite (Bucholz et al., 2011) compared to a value for μ of 0.33-0.38 (Marone and Lockner, 2004; Benhsen and Faulkner, 2013) and $\tilde{\mu}$ ~0.045 for muscovite compared to a value μ of 0.42-0.59 (Morrow et al., 2000; Marone and Lockner, 2004; Benhsen and Faulkner, 2013). Furthermore, the observed velocity strengthening behaviour of phyllosilicates is not predicted by the atomic scale controlled friction model, instead the model predicts no dependence of the frictional strength on (changes in) the sliding velocity.

The atomic scale friction model can (therefore) explain none of the observations of phyllosilicate friction and it is thus concluded that friction of dry phyllosilicates is not controlled by atomic scale interactions between sliding grains.

6.1.2 Grain scale barrier models versus previous experiments

In the models derived for grain scale interaction it is assumed that friction is controlled by (overcoming) the contact between the edges of adjacent grains. Contact between adjacent grains is in all the models assumed to occur by bending of individual grains over pore areas between grains by either i) elastic, ii) ductile time independent and iii) ductile time dependent bending. Overcoming the edge contact is assumed to result from either failure by i) cleavage of the edge-contact and ii) Griffith-type failure.

6.1.2.1. *Cleavage failure models*

Cleavage failure models predict coefficients of friction that are between 2 to 13 orders of magnitude lower than observed, i.e. a minimal value, $\mu_{(C+e)\min}$ of 2.5 x 10^{-13} for a combination of elastic bending and a minimal cleavage failure scenario and a maximum value, $\mu_{(C+e)\max}$ of 1.87 x 10^{-2} for a combination of a theoretical maximum cleavage failure scenario and time (in)dependent scenario. These values are respectively 13 to 2 orders of magnitude lower than the friction coefficient observed in experiments. The models for the theoretical maximum cleavage failure are based on an extremely unlikely scenario, namely failure of every cleavage plane of the area of edge-contact. The amount of failed cleavage planes in this scenario is extremely high, e.g. ~150 cleavage planes fail per edge contact for the ductile time independent contact mechanism at 10 MPa. There is no evidence in the literature or in the experiments for such a scenario. Furthermore the velocity strengthening observed in the literature is not predicted by any of the cleavage failure models. Lastly, cleavage failure models do predict the relation between the surface energy and frictional strength of phyllosilicates by Moore and Lockner (2004), since the macroscopic shear strength in all cleavage failure models is linearly dependent on the surface energy.

Since cleavage failure models can only explain the relation between the surface energy and the frictional strength reported by Moore and Lockner (2004) and none of the other observations on phyllosilicate friction it is concluded that cleavage failure edges of adjacent grains is not the controlling mechanism of phyllosilicate friction.

6.1.2.2 *Griffith-type failure models*

The models combining ductile time depended and time independent bending with Griffith-type failure predict frictional coefficients which fall in the range of frictional coefficients predicted by experiments, i.e. the models predict a μ ranging from 0.074 to 2.9, depending on values of the parameters used compared to μ of 0.42-0.59 (Morrow et al., 2000; Marone and Lockner, 2004; Benhsen and Faulkner, 2013)

The wide range of μ-values for these models is caused by the uncertainty in the following input parameters: i) The constant C_1 and ii) the initial crack width d. The friction coefficient depends linearly on C_1. The value for C_1, which relates the remotes stress acting on the crack σ_r with the force/stress to overcome an edge contact, F_{edge}, has no proper physical basis. In this study two extreme values, 1 and 10, are used in calculating the frictional strength. If C_1 has a value of 1, it means that the remote force acting on the crack is equal to the force, F_{edge}, needed to overcome the edge-contact. Note that in the scenario that failure occurs by a mode 2 type crack, F_{edge} would then be equal to remote applied stress and C_1 is 1. The extreme value of 10 for C_1 is based on the assumption that due to the crack geometry, a kind of cantilever effect occurs when the crack opens which creates a stress enhancement at the crack tip. The remote stress needed for failure is then reduced, which is reflected by a higher value of C_1.

The initial crack widths used in this study are taken from the length of the crack/imperfections seen at the edges of the grains in SEM-micrographs of the experiments conducted. There are also (many) imperfections on a scale that cannot be resolved by the SEM. For the Griffith-failure analysis this is however not important, since the largest initial flaw will takes the least amount of stress for failure and therefore the largest flaws are assumed to fail. In the model calculations values between 0.25μm-1.5μm for d are used and an increase in d leads to a $\frac{1}{\sqrt{d}}$ decrease in the predicted friction coefficient.

The frictional strength predicted by the Griffith-type failure models depends on the square root of the surface energy of the phyllosilicate minerals. This is not the same as the linear relation

observed by Moore and Lockner, 2004, but can potentially fit the data of Behnsen and Faulkner, 2012. Velocity strengthening behaviour however is not predicted, since Griffith like failure is not a time dependent process.

A microphysical model that combines Griffith-type failure of the edge contact and a ductile bending process resulting in contact of the edges of adjacent grains can potentially explain the frictional strength of phyllosilicates. Furthermore Griffith failure models are potentially consistent with data of Behnsen and Faulkner (2012). However, in all the Griffith failure models considered no velocity strengthening behaviour is predicted and therefore it is concluded that Griffith-like failure of an edge contact cannot be the (only) process controlling phyllosilicate friction.

6.1.2.3 *Formation of edge barriers*

In both type of failure models there is a huge discrepancy in the predicted frictional coefficients between models assuming only elastic bending and models assuming ductile bending as contact mechanism. This is caused by the fact that the contact area resulting from elastic bending is considerably smaller than from time (in)dependent ductile bending at the same applied normal stress, e.g. at 10 MPa for elastic bending the contact area is 0.67 % of the total area while for ductile bending this is ~5 %. The contact areas between the neighbouring grains are not quantified in the experiments but are most likely in the order of 5-10%. The values used in the analysis of the different bending mechanisms are at best estimates, since little is known on single crystal deformation of phyllosilicates. Lastly, for experiments with high sliding velocities, i.e. 0.1 μm/s-1mm/s, it seems very unlikely that contact between adjacent grains is controlled by a time dependent process. In the proposed models the time allowed for the grain to bent in a pore area is in the order of 0.01-10s depending on the grain width and sliding velocity. Based on the experiments conducted by Mares and Kronenberg (2008) such time spans would result in negligible contact between grains.

6.1.3 Summary of grain scale barrier models

None of the dry microphysical models considered can explain all observations on dry phyllosillicate friction. Models combining Griffith-type failure of an edge contact in combination with a ductile time (in)dependent bending can potentially explain the frictional strength and the relation between the surface energy and the frictional strength as observed for phyllosilicates. However none of the models, including the models combining Griffith-type failure and ductile bending predict velocity-strengthening behaviour. The contact between adjacent grains of the model microstructure is assumed to result from a simple bending geometry and ignores the more geometrically complex contacts resulting from ductile deformation mainly seen in the loading experiments (e.g. contact where one or both of the grains were completely folded up.)

The failure mechanisms considered for edge failure are parallel processes, meaning that the process that results in the least shear resistance for failure of the edge will be the process that actually occurs. Since cleavage failure mechanisms offer systemically lower frictional strength for the same contact mechanisms considered, failure of the edge contact would (preferentially) occur by cleavage failure and not Griffith-type failure. If the analysis done in the cleavage failure model is correct, the models considered here predict that edge interaction can therefore be neglected in dry phyllosilicate friction.

6.2 Wet models versus observations in literature

Recall from Chapter 2 that from previous experimental studies a microphysical model for wet phyllosilicate friction needs to explain the following main observations:

i) A significant drop in frictional strength (μ_{wet} is~0.1-0.2 lower than μ_{dry}) of phyllosilicates in the presence of pore fluids compared to dry friction (e.g. Morrow et al, 2000; Moore and Lockner, 2004).

ii) Velocity strengthening behaviour of phyllosilicates at room temperature (e.g. Ikari et al. 2011, den Hartog et al. 2013)

iii) An observed decrease in velocity-strengthening with increasing temperature to (near) velocity-neutral or even slightly velocity-weakening behaviour at the temperature range considered. (RT<T<400 ^{0}C) (e.g. van Diggelen et al., 2010; den Hartog et al., 2013; He and Lu, 2014)

iv) The qualitative relation found by Moore and Lockner, 2004 and Behnsen and Faulkner, 2012 that phyllosilicate minerals with hydrophobic plate surfaces have a lower drop in frictional strength between μ_{wet} and μ_{dry} than phyllosilicates with hydrophilic plate surfaces.

Models for wet phyllosilicate friction were derived by considering if the presence of water/pore fluids would change the models derived for dry phyllosilicate friction.

6.2.1 Atomic scale barrier model in presence of water versus previous experiments

The model for atomic controlled friction in the presence of water predicts that the macroscopic coefficient of friction is controlled by the atomic coefficient of friction $\tilde{\mu}$. This result is equivalent to that of the dry atomic controlled friction. Values of the atomic friction coefficient of phyllosilicates reported in the literature are roughly one order of magnitude lower than the macroscopic coefficient of friction observed, i.e. $\tilde{\mu}$ is ~0.03 for pyrophyllite (Bucholz et al., 2011) compared to a value for μ of 0.33-0.38 (Marone and Lockner, 2004; Benhsen and Faulkner, 2013) and $\tilde{\mu}$ ~0.045 for muscovite compared to a value μ of 0.42-0.59 (Morrow et al., 2000; Marone and Lockner, 2004; Benhsen and Faulkner, 2013). Furthermore, the observed velocity strengthening behaviour of phyllosilicates is not predicted by the atomic scale controlled friction model, instead the model predicts no dependence of the frictional strength on (changes in) the sliding velocity. Lastly, the drop in frictional strength is not predicted by the wet atomic scale controlled friction model.

The atomic controlled friction model cannot explain any of the observations on wet phyllosilicate friction and it is therefore concluded that wet phyllosilicate friction is not controlled by atomic interactions between the phyllosilicate grains.

6.2.2 Thin adsorbed film model

The coefficient of friction predicted by the adsorbed film model depends on the sliding velocity of grains past each other. For typical macroscopic sliding velocities (10^{-5} µm/s-1µm/s) used in friction experiments the model predicts friction coefficients of 3 to 7 orders of magnitude lower than observed, i.e. 4.09 x 10^{-8} to 9.38 x 10^{-8} for a sliding velocity of 10^{-5} µm/s and 4.09 x 10^{-3} to 9.38 x 10^{-3} for a sliding velocity of 1µm/s. Only for sliding velocities in the order of 100µm/s -1µm/s frictional parameters are predicted similar to those observed in friction experiments. This model predicts velocity-strengthening behaviour, but a relatively much greater increase in the shear stress with an increase in the sliding velocity is predicted than is observed in experiments.

In the thin adsorbed film model it is assumed that thin films of water have properties similarly to bulk continuum water, i.e. that viscous slip on a thin film can be described by viscous slip of a Newtonian fluid (cf. equation 4.7). As described in section 5.3.2.3 this assumption is based on SFA-studies on the properties of (confined) water (e.g. Israelachvili, 1986; Israelachvili and Kott, 1998; Klein et al., 2001). In SFA studies on other liquids (Israelachvili et al., 1990; Israelachvili and

Kott, 1998) and in studies on the properties of confined water using IFM (e.g. Major et al., 2006; Goertz et al., 2007) the properties of thin confined films are however greatly dissimilar to that bulk properties**.** Since the experimental setup of the SFA studies are more akin to actual conditions of frictional sliding of phyllosilicate grains than the IFM setup the assumption that thin adsorbed films of water behave similarly to bulk liquids is reasonable, certainly for the conditions relevant for phyllosilicate friction.

The thin adsorbed film model predicts values for (apparent) friction coefficient that are orders of magnitude lower than observed in experiments for typical sliding velocities used in experiments. While the model predicts velocity strengthening behaviour as is observed in phyllosilicate friction, the degree in which strengthening is predicted is of a much higher order than observed. It is therefore concluded that the hypothesis of Moore and Lockner (2004) can be refuted and viscous slip on a thin adsorbed water film is not the process controlling friction in phyllosilicates.

6.2.3 Grain scale barrier models in presence of water versus previous experiments

6.2.3.1 *Cleavage failure models*

It is assumed that water has no effect on the mechanism of cleavage failure. Therefore cleavage failure models for wet phyllosilicate friction predict similar frictional parameters as for dry phyllosilicate friction if it is assumed that frictional sliding on the horizontal contact area occurs by atomic controlled friction and cannot explain any of the observations on wet phyllosilicate friction. If it is assumed that viscous slip on a thin film controls friction on the horizontal contact area the cleavage failure models predict velocity strengthening due to the viscous slip on the horizontal contact area, but cannot account for any of the other observation on wet friction.

The cleavage failure models cannot account for any of the main observations on wet phyllosilicate friction, so it is concluded that cleavage failure of the edge contact is not controlling wet phyllosilicate friction.

6.2.3.2 *Sub critical crack growth failure models*

No literature exists on sub critical crack growth mechanisms in phyllosilicate minerals and therefore no frictional parameters could be calculated. So only qualitative statements can be done on this model. A combination of ductile time dependent bending can potentially account for most of the observations in wet phyllosilicate friction. Qualitatively this would lead to i) velocity strengthening behaviour at room temperature and ii) with increasing temperature a decrease in velocity strengthening behaviour. At room temperature ductile time dependent processes, such as dislocation glide are less active than at higher temperatures. So with increasing temperature the contact area between grains is increasingly the result of ductile time dependent bending. Since this process leads to velocity weakening behaviour, it could be argued that a decrease velocity strengthening with temperature is predicted by this model combination. Lastly, iii) the frictional strength by sub critical crack growth failure is predicted to be lower than dry Griffith-type failure at the same experimental conditions, potentially explaining the drop in frictional strength observed from dry to wet phyllosilicate friction. However research is needed on sub-critical crack growth in phyllosilicates to be able to conclude if sub critical crack growth mechanisms occur in phyllosilicate minerals and could potentially control phyllosilicate friction.

7 Conclusions

In this study microphysical models were derived for the frictional behaviour of wet and dry phyllosilicate gouges at relatively low temperatures (room temperature to ~400 ^{0}C) in which friction was controlled either by atomic or by grain scale. The predicted frictional parameters of these models, e.g. coefficient of friction and the dependence of this coefficient on the sliding velocity, were compared with previous observations. Based on these models the following conclusions can be drawn:

1) The approach used in the loading and shear experiments in which samples were impregnated by epoxy resin while under load is successful in eliminating 'unloading' artefacts seen in conventional friction studies. For better results in the shear experiments a different experimental setup needs to be developed, where impregnation of the samples is possible while also having lateral containment.

2) From the loading and shear experiments it is concluded that during frictional sliding of phyllosilicates the edges of neighbouring grains are in contact. It is apparent from microstructural evidence that during frictional sliding these edges fail, both by brittle and ductile deformation.

3) By comparing the observations on phyllosilicate friction in the literature with models in which atomic scale interactions control friction it is concluded that both wet and dry friction of phyllosilicates are not controlled by atomic scale interactions, since these models predict an order of magnitude lower frictional strength and no dependence of the coefficient of friction on the sliding velocity.

4) The model derived in which phyllosilicate friction is controlled by viscous slip on a thin adsorbed water film predicts frictional parameters that are not in agreement with observations, i.e. coefficients of frictions that are orders of magnitudes too low and show a much higher dependence of the coefficient of friction on the sliding velocity. It is therefore concluded that the hypothesis of Moore and Lockner (2004) in which friction of phyllosilicates is accommodated by viscous slip on thin adsorbed water is not correct.

5) None of the microphysical models derived for grain scale controlled friction can explain the observations on dry phyllosilicate friction, such as the relative low coefficient of friction, velocity strengthening behaviour and an empirical relation between surface energy and the coefficient of friction . Griffith-type failure of edge-contact models are in agreement with most observations, except that no velocity strengthening is predicted.

6) Cleavage failure models predict extremely low frictional strength. This indicates that grain scale barriers are present during phyllosilicate friction, but these do not control phyllosilicate friction

7) A combination of ductile time dependent edge-contact and sub critical crack growth type failure of the edge contact can potentially explain most of the observed phenomena of wet phyllosilicate friction, e.g. lower wet frictional strength vs. dry frictional strength and velocity strengthening behaviour. Research is needed on sub critical growth mechanisms in order to evaluate this in a physical robust way.

Acknowledgements

First, I would like to thank Peter van Krieken, Gert Kastelein and especially Jon Samuelson for their help and support with my experiments. Next, Elisenda Bakker is thanked for providing the necessary wake-up call when everything seemed to fall apart and for having the patience to review and read trough my very rough first drafts. A special thank you goes to Sabine den Hartog who thoroughly reviewed this thesis, which she for reasons I probably will never fathom apparently enjoyed as well. Finally, Chris Spiers is sincerely thanked for giving me the support, both professional as personal, and time to finish this thesis in a satisfactory manner.

Appendix 1

Symbol	Definition	Symbol	Definition
a	Long axis of phyllosilicate grain	c_0	Initial (Griffith) crack width
b	Short axis of phyllosilicate grain	c_{mean}	Mean (Griffith) crack width
$\frac{b}{a}$	Ratio of short and long axis of phyllosilicate grain	c_f	(Griffith) crack width at failure
S	Average horizontal distance between grains	β	Experimental constant
c	Vertical contact length between adjacent grains	Q	Activation energy needed for dislocation creep mechanisms to start
ϕ	Porosity of the phyllosilicate aggregate	R	Gas constant
τ	Macroscopic shear stress (acting on unit cell)	T	Temperature
$\tilde{\tau}$	Microscopic shear stress (acting within unit cell)	t_f	Time of failure of edge contact
σ_n	Macroscopic normal stress (acting on unit cell)	v_{slide}	(Macroscopic) sliding velocity of phyllosilicate grains
$\tilde{\sigma}_n$	Microscopic normal stress (acting within unit cell)	$\dot{\gamma}$	Shear strain rate
μ	Macroscopic coefficient of friction	P_f	Pore fluid pressure
$\tilde{\mu}$	Microscopic coefficient of friction	σ_{neff}	Effective normal stress
γ_s	Surface energy of muscovite/phyllosilicate grain	δ	Thickness of adsorbed water film
E_a	Young's modulus of single crystal (muscovite/phyllosilicate grain	Π_d	Disjoining pressure of thin adsorbed film
E_c	Young's modulus of phyllosilicate/muscovite aggregate	v_{slide}	Macroscopic sliding velocity
F_{edge}	Force needed for sliding grain to overcome an edge contact. Subscript denotes the failure mechanisms, e.g. $F_{edge\,C_{\min}}$ denotes the minimum force related to cleavage failure	$\mu_{(C+e)\min}$	The predicted macroscopic friction coefficient of a microphysical model. Subscripts C and G denote cleavage and Griffith-type failure, e, d, dt and denote elastic, ductile time independent and ductile time dependent contact
τ_{edge}	Stress needed for sliding grain to overcome an edge contact. Subscript denotes the failure mechanisms, e.g. $\tau_{edge\,C_{\min}}$ denotes the minimum stress related to cleavage failure	η	Viscosity of thin adsorbed film
S'	Average horizontal width of cleavage planes	v_c	Crack growth velocity
d	Average distance between opened cleavage planes	v_0	Reference crack growth velocity
$d_{lattice}$	001 lattice spacing of phyllosilicate mineral/muscovite	H	Activation enthalpy related to subcritical crack growth
σ_{yield}	Yield strength needed before ductile deformation initiates	B	Experimental constant (in subcritical crack growth)
$\dot{h}$	Work hardening rate	τ_{scc}	Macroscopic shear stress related to subcritical crack growth failure
σ_r	Remote stress acting on crack	n	Stress corrosion index
C_1	Constant relating the remote stress acting on a crack to the force F_{edge} /stress τ_{edge} acting a the edge contact	K_1	Stress intensity factor for a mode 1 crack

Appendix 1 Explanation of the symbols used in this study

Appendix 2

Symbol	Meaning	Value	Based on:
a	(Average) width/length of long axis of phyllosilicate grain	~ $30x10^{-6}$m (30µm)	-Microstructural evidence of section 3, Den Hartog, 2013, van Diggelen et al., 2010
b	(Average) height of short axis of phyllosilicate grain	~ $30x10^{-6}$m (30µm)	-Microstructural evidence of section 3, Den Hartog, 2013, van Diggelen et al, 2010
$\frac{b}{a}$	Ratio of short and long axis of phyllosilicate grain	0.1	-Microstructural evidence of section 3, Den Hartog, 2013, van Diggelen et al, 2010
S	Average distance between adjacent phyllosilicate grains	~ $2x10^{-6}$m (2µm)	Microstructural evidence
$\tilde{\mu}$	Atomic coefficient of friction of muscovite	0.035, but taken as 0 (see text)	Liu et al, 1996
γ_s	Surface energy of muscovite	0.3 Jm^{-2}	Bailey, 1961
γ_{001}	Surface energy related to 001 interlayer bond strength	~ 1 Jm^{-2}	Giese, 1974; Moore and Lockner, 2004
E_c	Young's modulus of single crystal of muscovite	176,5 GPa	Mcneil and Grimditch (1993)
E_a	(Average value of) Young's modulus of muscovite aggregate	15 Gpa	C.J. Spiers, personal communication/ Choloach and Smiths, 2006
$d_{lattice}$	001 lattice spacing muscovite	$10,04x10^{-10}$ (10,04 $\dot{A}$)	Meunier and Velde, 2004
d	Average distance between opened cleavage planes	~ $2x10^{-7}$m (0.2µm)	Assumption/microstructural evidence
C_1	Constant relating the remote stress σ_r acting on a crack to force F_{edge} /stress τ_{edge} at the edge contact	1-10	C.J. Spiers, personal communication
σ_{yield}	Yield strength needed before ductile deformation initiates		
$\dot{h}$	Work hardening rate	20x 10^7 Pa	Assumption/ see text
d_f	Average (Griffith) crack width at failure	0.25-1.5µm	Microstructural evidence

Appendix 2 Values used in calculation of (apparent) friction coefficients of the different proposed microphysical models

Appendix 3 Subcritical crack growth failure

The first method to obtain an expression relating the failure strength of the grain contact by subcritical crack growth failure and the macroscopic sliding velocity of the grains is as follows. It is assumed that the velocity of the sliding grains is determined by the time it takes for a subcritically growing crack with initial length c_0 to grow to a failure length c_f at which the crack fails dynamically. It is assumed that the time it takes for the grain to slide the width of the unit cell $(a+S)$, the distance between successive contacts, is negligible compared to the time it takes for failure of the contact. The relation between the sliding velocity and the time to failure is then:

$$v_{slide} = \frac{d_{unitcell}}{t_f} \tag{A3.1}$$

where $d_{unitcell}$ is the distance a grain needs to slide between contacts and thus failure events, which is the width $(a+S)$ of the unit cell.

The time of failure is obtained by realizing that the crack propagation velocity is the change in crack length versus time.

$$\frac{dc}{dt} = v_o \exp(\frac{-H + bK_1}{RT}) \tag{A3.2}$$

Rearranging the terms and integrating from initial length c_0 to grow to a failure length c_f and t_0 to t_f leads to:

$$\int_{c_0}^{c_f} \exp(A + B\sqrt{c})dc = v_0 \int_{t_0}^{t_f} dt \tag{A3.3}$$

Where $A = \frac{H}{RT}$ and $B = \frac{-b\sigma_r\sqrt{\pi}}{RT}$

$$\left[_{c_0}^{c_f} \frac{(2B\sqrt{c} - 1)\exp(A - B\sqrt{c})}{B^2} = v_0 \right[_{t_0}^{t_f} t$$

$$\frac{(2B\sqrt{c_f} - 1)\exp(A - B\sqrt{c_f})}{B^2} - \frac{(2B\sqrt{c_0} - 1)\exp(A - B\sqrt{c_0})}{B^2} = v_0 t_f \tag{A3.4}$$

Filing in A and B and rearranging the terms leads to the following expression of t_f

$$\frac{(2\frac{-b\sigma_r\sqrt{\pi}}{RT}\sqrt{c_f} - 1)\exp(\frac{H}{RT} - \frac{-b\sigma_r\sqrt{\pi}}{RT}\sqrt{c_f})}{v_0(\frac{-b\sigma_r\sqrt{\pi}}{RT})^2} - \frac{(2\frac{-b\sigma_r\sqrt{\pi}}{RT}\sqrt{c_0} - 1)\exp(\frac{H}{RT} - \frac{-b\sigma_r\sqrt{\pi}}{RT}\sqrt{c_0})}{v_0(\frac{-b\sigma_r\sqrt{\pi}}{RT})^2} = t_f \tag{A3.5}$$

Finally, combining equations A3.1 and A3.5 gives an expression relating the sliding velocity to the applied remote stress:

$$v_{slide} = \frac{d_{unitcell}}{\frac{(2\frac{-b\sigma_r\sqrt{\pi}}{RT}\sqrt{c_f}-1)\exp(\frac{H}{RT}-\frac{-b\sigma_r\sqrt{\pi}}{RT}\sqrt{c_f})}{v_0(\frac{-b\sigma_r\sqrt{\pi}}{RT})^2} - \frac{(2\frac{-b\sigma_r\sqrt{\pi}}{RT}\sqrt{c_0}-1)\exp(\frac{H}{RT}-\frac{-b\sigma_r\sqrt{\pi}}{RT}\sqrt{c_0})}{v_0(\frac{-b\sigma_r\sqrt{\pi}}{RT})^2}}$$

References

Alcantar, N., Israelachvili, J., & Boles, J. (2003). Forces and ionic transport between mica surfaces: Implications for pressure solution. *Geochimica et Cosmochimica Acta*, *67*(7), 1289–1304.

Atkinson, B.K. (1982), Subcritical crack growth in geological materials, *Journal of Geophysical Research, 89,* 4077-4114

Bailey, A. I. (1961). Friction and Adhesion of Clean and Contaminated Mica Surfaces. *Journal of Applied Physics*, *32*(8), 1407.

Beaglehole, D., & Christenson, H. K. (1992). Vapor Adsorption on Mica and Silicon : Entropy Effects , Layering , and Surface Forces, (14), 3395–3403.

Beeler, N.M., Tullis, T.E., Blanpied, M.L. and Weeks, J.D., 1996. Frictional behavior of large displacement experimental faults. J. Geophys. Res. 101 (B4), 8697-8715.

Behnsen, J., & Faulkner, D. R. (2012). The effect of mineralogy and effective normal stress on frictional strength of sheet silicates. *Journal of Structural Geology*, *42*, 49–61.

Behnsen, J., & Faulkner, D. R. (2013). Permeability and frictional strength of cation-exchanged montmorillonite. *Journal of Geophysical Research: Solid Earth*, *118*(6), 2788–2798.

Berthoud, P., & Baumberger, T. (1999). Physical analysis of the state- and rate-dependent friction law :, *59*(22), 313–327.

Bird, P. (1984). Hydration-phase diagrams and friction of montmorillonite under laboratory and geologic conditions, with implications for shale compaction, slope stability, and strength of fault gouge. *Tectonophysics, 107*, 235-260

Bos, B., Peach, J., Spiers, C. (2000). Frictional-viscous flow of simulated fault gouge caused by the combined effects of phyllosilicates and pressure solution. *Tectonophysics, 327*, 173-194.

Bos, B. and Spiers, C. (2002). Frictional-viscous flow of phyllosilicate-bearing fault rock: microphysical model and implications for crustal strength profiles. *Journal of Geophysical Research, 107*, 20-28.

Brantut, N., Schubnel, A., Rouzaud, J., Brunet, F., Shimamoto, T. (2008). High-velocity frictional properties of a clay-bearing fault gouge and implications for earthquake mechanics. *Journal of Geophysical Research, 113*, Bhushan, B., Israelachvili, J.N. & Landman, U. (1995). Nanotribology: friction and lubrication at the atomic scale, *Nature, 374*, 607-616

Bucholz, E. W., Zhao, X., Sinnott, S. B., & Perry, S. S. (2012). Friction and Wear of Pyrophyllite on the Atomic Scale. *Tribology Letters*, *46*(2), 159–165.

Butt, H., Graf, K., & Kappl, M. (2003). *Physics and Chemistry of Interfaces* WILEY-VCH GmbH & Co .

Byerlee, J., 1978. Friction of rocks. Pure Appl. Geophys. 116 (4), 615-626.

Carpenter, B., Marone, C., Saffer, D. (2011). Weakness of the San Andreas fault revealed by samples from the active fault zone. *Nature Geoscience*,

Cholach, P. Y., & Schmitt, D. R. (2006). Intrinsic elasticity of a textured transversely isotropic muscovite aggregate: Comparisons to the seismic anisotropy of schists and shales. *Journal of Geophysical Research*, *111*(B9),

Collettini, C. (2011). The mechanical paradox of low-angle normal faults: Current understanding and open questions. *Tectonophysics*, *510*(3-4), 253–268.

Collettini, C., Niemeijer, A., Viti, C., & Marone, C. (2009). Fault zone fabric and fault weakness. *Nature*, *462*(7275), 907–910

Crawford, B., Faulkner, D., Rutter, E., 2008. Strength, porosity, and permeability development during hydrostatic and shear loading of synthetic quartz-clay fault gouge. *Journal of Geophysical Research, 113*,

Den Hartog, S.A.M., Niemeijer, A. R., & Spiers, C. J. (2012). New constraints on megathrust slip stability under subduction zone P-T conditions. *Earth and Planetary Science Letters*, *353-354*, 240–252.

Den Hartog, S.A.M., Frictional behaviour of megathrust fault gouges under in -situ subduction zone conditions, Doctoral dissertation, University Utrecht

Den Hartog, S.A.M., Niemeijer, a. R., & Spiers, C. J. (2013). Friction on subduction megathrust faults: Beyond the illite-muscovite transition. *Earth and Planetary Science Letters*, *373*, 8–19.

Den Hartog, S.A.M. & Spiers, C. J. (2013b). Influence of subduction zone conditions and gouge composition on frictional slip stability of megathrust faults. *Tectonophysics*, *600*, 75–90.

Den Hartog, S.A.M., and C. J. Spiers (2014), A microphysical model for fault gouge friction applied to subduction megathrusts, J. Geophys. Res. Solid Earth, 119, 1510–1529

Dewhurst, D. N., Brown, K. M., Clennell, M. B., & Westbrook, G. K. (1996). A comparison of the fabric and permeability anisotropy of consolidated and sheared silty clay. *Engineering Geology*, *42*(4), 253–267.

Dieterich, J.H., (1979), Modeling of rock friction: 1. Experimental results and constitutive equations. J. Geophys. Res., 84(B5), 2161-2168

Faulkner, D.R., Mitchell, T.M., Behnsen, J., Hirose, T. and Shimamoto, T., 2011. Stuck in the mud? Earthquake nucleation and propagation through accretionary forearcs. Geophys. Res. Le. 38 (18), L18303, DOI:10.1029/2011GL048552.

Giese, R. F. (1978). The Electrostatic Interlayer Forces of Layer Structure Minerals. *Clays and Clay Minerals*, *26*(1), 51–57.

Goertz, M.P., Houston, J.E. and Zhu, X. Y., 2007, Hydrophilicity and the viscosity of interfacial water, 23, 5491-5497

Griffith, A. A., (1920) The phenomena of rupture and flow in solids, *Philosophical transactions of the Royal Society of London, series A,* Vol. 221, 163-198

Griffith A.A., (1924) The theory of rupture. In: Biezeno CG, Burgers JM (eds) Proc. 1st Int. Congr. Appl. Mech.: Delft, Tech. Boekhandel en Drukkerij J. Waltman Jr., pp 54–63

Haines, S. H., Kaproth, B., Marone, C., Saffer, D., & van der Pluijm, B. (2013). Shear zones in clay-rich fault gouge: A laboratory study of fabric development and evolution. *Journal of Structural Geology*, *51*, 206–225.

Heidug, W.K., 1995. Intergranular solid-fluid phase transforma- tions under stress: the effect of surface forces. J. Geophys. Res., 100(B4): 5931-5940

Horn, H., Deere, D. (1962). Frictional characteristics of minerals. Geotechnique 12

Holdsworth, R. E., van Diggelen, E. W. E., Spiers, C. J., de Bresser, J. H. P., Walker, R. J., & Bowen, L. (2011). Fault rocks from the SAFOD core samples: Implications for weakening at shallow depths along the San Andreas Fault, California. *Journal of Structural Geology*, *33*(2), 132–144.

Hyndman, R.D., Yamano, M. and Oleskevich, D.A., 1997. The seismogenic zone of subduction thrust faults. Isl. Arc 6 (3), 244-260.

Ikari, M.J., Saffer, D.M., and Marone, C., 2007, Effect of hydration state on the frictional prop- erties of montmorillonite-based fault gouge: Journal of Geophysical Research, v. 112

Ikari, M., Saffer, D., Marone, C., 2009. Frictional and hydrologic properties of clay- rich fault gouge. *Journal of Geophysical Research, 114*

Ikari, M. J., & Kopf, A. J. (2011). Cohesive strength of clay-rich sediment. *Geophysical Research Letters*, *38*(16)

Ikari, M. J., Marone, C., & Saffer, D. M. (2011a). On the relation between fault strength and frictional stability. *Geology*, *39*(1)

Ikari, M. J., Niemeijer, A. R., & Marone, C. (2011b). The role of fault zone fabric and lithification state on frictional strength, constitutive behavior, and deformation microstructure. *Journal of Geophysical Research*, *116*(B8)

Ikari, M. J., & Saffer, D. M. (2011). Comparison of frictional strength and velocity dependence between fault zones in the Nankai accretionary complex. *Geochemistry Geophysics Geosystems*, *12*(4)

Israelachvili, J.N. and Adams G.E., (1978) Measurement of Forces between Two Mica Surfaces in Aqueous Electrolyte Solutions in the Range 0-100 nm, J. Chem. Soc., Faraday Trans. 1, 74, 975-1001

Israelachvili, J. N. (1982). Forces between surfaces in liquids. *Advances in Colloid and Interface Science*, *16*(1), 31–47. Israelachvili, J. N. (1986). Measurement of the viscosity of liquids in very thin films. *Journal of Colloid and Interface Science*, *110*(1), 263–271.

Israelachvili, J. N. (1986). Measurements of the viscosity of thin fluid films between two surfaces with and without adsorbed polymers. *Colloid & Polymer Science*, *264*(12), 1060–1065.

Israelachvili and Kott, 1988, Shear Properties and Structure of Simple Liquids in Molecularly Thin Films- The Transition from Bulk (Continuum) to Molecular Behavior with Decreasing Film Thickness, Journal of Colloid and Interface Science, Vol. 129, 461-467

Israelachvili, J.N., McGuiggan, P. Gee, M., Homola, A., Robbins, M. and Thompson P. (1990), Liquid dynamics in molecularly thin films, Journal of Phys. Condens. Matter. **2** 89-98

Israelachvili, J.N., Chen, Y-L. & Yoshizawa, H. (1995), Relationschip between adhesion and friction forces, *Fundamentals of Adhesion and Interfaces,* 261-279

Israelachvili, J., Mcguiggan, P., Gee, M., Homola, A., Robbinsq, M., & Thompson, P. (1998). Liquid dynamics in molecularly thin films.

Israelachvili, J.N., 2011, Intermolecular and surface forces, Elsevier Academic Press, 415–467

Kopta, S., & Salmeron, M. (2000). The atomic scale origin of wear on mica and its contribution to friction. *The Journal of Chemical Physics*, *113*(18)

Krim, J. (2012). Friction and energy dissipation mechanisms in adsorbed molecules and molecularly thin films. *Advances in Physics*, *61*(3), 155–323. doi:10.1080/00018732.2012.706401

Logan, J., Friedman, M., Higgs, N., Dengo, C., Shimamoto, T., 1979. Experimental studies of simulated gouge and their application of studies of natural fault zones. In: Proc. Conf. Vlll Analysis of Actual Fault Zones in Bedrock. USGS, pp. 305e343. Open-file rep. 79-1239

Logan, J.M., Dengo, C.A., Higgs, N.G. and Wang, Z.Z., 1992. Fabrics of experimental fault zones: their development and relationship to mechanical behavior, in: Evans, B., Wong, T.-F. and Brace, W.F. (Eds.), Fault Mechanics and Transport Properties of Rocks. Academic Press, London, pp. 33-67.

Liu, E., Blanpain, B., Celis, J.P., Roos, J.R.: Comparative study between macrotribology and nanotribology. J. Appl. Phys. 84, 4859–4865 (1998)

Lu, Zhen, He, Changrong, Frictional behaviour of simu- lated biotite fault gouge under hydrothermal conditions, *Tectonophysics* (2014)

Major, R.C., Houston, J.E., McGrath, M.J., Siepmann, J.I., and Zhu, X.Y., (2006), Viscous water meniscus under nanoconfinement, Physical Review Letters, 177803 1-4.

Mares, V. ., & Kronenberg, a. . (1993). Experimental deformation of muscovite. *Journal of Structural Geology*, *15*(9-10), 1061–1075.

Mariani, E., Brodie, K. H., & Rutter, E. H. (2006). Experimental deformation of muscovite shear zones at high temperatures under hydrothermal conditions and the strength of phyllosilicate-bearing faults in nature. *Journal of Structural Geology*, *28*(9), 1569–1587.

Marone, C. (1998). Laboratory-Derived Friction Laws and Their Application To Seismic Faulting. *Annual Review of Earth and Planetary Sciences*, *26*(1), 643–696.

Marone, C. and Scholz, C.H., 1988. The depth of seismic faulting and the upper transition from stable to unstable slip regimes. Geophys. Res. Le. 15 (6), 621-624.

Misra, S., & Burg, J.-P. (2012). Mechanics of kink-bands during torsion deformation of muscovite aggregate. *Tectonophysics*, *548-549*, 22–33.

Moore, D. E. (2004). Crystallographic controls on the frictional behavior of dry and water-saturated sheet structure minerals. *Journal of Geophysical Research*, *109*(B3).

Moore, D. E., & Lockner, D. a. (2008). Talc friction in the temperature range 25°-400 °C: Relevance for Fault-Zone Weakening. *Tectonophysics*, *449*(1-4), 120–132.

Moore, D. E., & Lockner, D. a. (2011). Frictional strengths of talc-serpentine and talc-quartz mixtures. *Journal of Geophysical Research*, *116*(B1), 1

Moore, D. E., Summers, R., & Byerlee, J. D. (1988). Sliding behavior and deformation textures of heated illite gouge Tins paper describes the results of a petrographic study of the deformation textures developed during triaxial friction experiments on heated fault gouge . Preliminary textural studies on a , *I*(3).

Morrow, C., Radney, B., Byerlee, J., 1992. Frictional strength and the effective pressure law of montmorillonite and illite clays. *Fault Mechanics and Transport Properties of Rocks; a Festschrift in Honor of W. F. Brace.* Academic Press, San Diego, CA, pp. 69-88 (Chapter 3).

Morrow, C. a., Moore, D. E., & Lockner, D. a. (2000). The effect of mineral bond strength and adsorbed water on fault gouge frictional strength. *Geophysical Research Letters*, *27*(6), 815–818.

Niemeijer, a. R., & Spiers, C. J. (2005). Influence of phyllosilicates on fault strength in the brittle-ductile transition: insights from rock analogue experiments. *Geological Society, London, Special Publications*, *245*(1), 303–327.

Niemeijer, a. R., & Spiers, C. J. (2007). A microphysical model for strong velocity weakening in phyllosilicate-bearing fault gouges. *Journal of Geophysical Research*, *112*(B10),

Obreimoff, J. W. (1930). The Splitting Strength of Mica. *Proceedings of the Royal Society A: Mathematical, Physical and Engineering Sciences*, *127*(805), 290–297. doi:10.1098/rspa.1930.0058

Ohnishi, S. (2009). Friction and Capillary Forces at the Nanometer Scale. *E-Journal of Surface Science and Nanotechnology*, *7*(February), 137–140.

Pashley, R. M., & Israelachvili, J. N. (1984). Molecular layering of water in thin films between mica surfaces and its relation to hydration forces. *Journal of Colloid and Interface Science*, *101*(2), 511–523.

Paterson, M. S. (1995). A theory for granular flow accommodated by material transfer via an intergranular fluid. *Tectonophysics*, *245*(3-4), 135–151.

Paterson, M.S. and Wong, T.-F., 2005. Experimental Rock Deformation - the Brittle Field, 2nd ed. Springer, Berlin.

Peacock, S.M. and Hyndman, R.D., 1999. Hydrous minerals in the mantle wedge and the maximum depth of subduction thrust earthquakes. Geophys. Res. Le. 26 (16), 2517-2520.

Putnis, A. 1992. Introduction to mineral sciences. Cambridge University Press. 194-195.

Renard, F., and P. Ortoleva (1997), Water films at grain-grain contacts: Debye-Hu¨ckel, osmotic model of stress, salinity, and mineralogy depen- dence, Geochim. Cosmochim. Acta, 61, 1963–1970.

Rice, J. R., Lapusta, N., & Ranjith, K. (2001). Rate and state dependent friction and the stability of sliding between elastically deformable solids. *Journal of the Mechanics and Physics of Solids*, *49*(9), 1865–1898.

Ruina, A., 1983. Slip instability and state variable friction laws. J. Geophys. Res. 88 (B12), 10359-10370.

Rutter, E. H. (1983), Pressure solution in nature, theory, and experiment, J. Geol. Soc. London, 140, 725–740.

Saffer, D., Frye, K., Marone, C., Mair, K. (2001). Laboratory results indicating complex and potentially unstable frictional behavior of smectite clay. *Geophysical Research Letters*, *28*, 2297-2300.

Saffer, D., Marone, C., 2003. Comparison of smectite- and illite-rich gouge fric- tional properties: application to the undip limit of the seismogenic zone along subduction megathrusts. *Earth and Planetary Science Letters, 215*, 219-235.

Sakuma, H. (2013). Adhesion energy between mica surfaces: Implications for the frictional coefficient under dry and wet conditions. *Journal of Geophysical Research: Solid Earth*, *118*(12), 6066–6075. doi:10.1002/2013JB010550

Schleicher, a. M., van der Pluijm, B. a., & Warr, L. N. (2010). Nanocoatings of clay and creep of the San Andreas fault at Parkfield, California. *Geology*, *38*(7), 667–670.

Scholz, C. H. (1998). Earthquakes and friction laws. *Nature, 391,* 37–42.

Scholz, C.H., 2002. The mechanics of earthquakes and faulting, second ed. Cambridge University Press, Cambridge.

Scruggs, V., Tullis, T. (1998). Correlation between velocity dependence of friction and strain localization in large displacement experiments on feldspar, muscovite and biotite gouge. *Tectonophysics, 295*, 15-40.

Shimamoto, T., Logan, J. (1981). Effects of simulated clay gouges on the sliding behavior of Tennessee sandstone. Tectonophysics 75

Simons, M. et al., 2011. The 2011 magnitude 9.0 Tohoku-Oki earthquake: mosaicking the megathrust from seconds to centuries. Science 332, 1421-1425.

Takahashi, M., Mizoguchi, K., Kitamura, K., Masuda, K., 2007. Effects of clay content on the frictional strength and fluid transport property of faults. *Journal of Geophysical Research, 112*

Tembe, S., Lockner, D., Wong, T., 2010. Effect of clay content and mineralogy on frictional sliding behavior of simulated gouges: binary and ternary mixtures of quartz, illite, and montmorillonite. *Scientific Results Volume, 115*.

Tesei, T., Collettini, C., Carpenter, B. M., Viti, C., & Marone, C. (2012). Frictional strength and healing behavior of phyllosilicate-rich faults. *Journal of Geophysical Research*, *117*(B9),

Van Diggelen, E. W. E., De Bresser, J. H. P., Peach, C. J., & Spiers, C. J. (2010). High shear strain behaviour of synthetic muscovite fault gouges under hydrothermal conditions. *Journal of Structural Geology*, *32*(11), 1685–1700.

Vrolijk, P., 1990. On the mechanical role of smectite in subduction zones. Geology 18 (8), 703-707.

Wiederhorn, S.M. & Bolz, L.H. (1970). Stress corrosion and static fatique of glass, *Journal of the American Ceramic Society, 53-10,* 543-548